ALMA MATER STUDIORUM - UNIVERSITÀ DI BOLOGNA
PhD COURSE IN BIOENGINEERING
XXIV CYCLE - SCIENTIFIC DISCIPLINARY SECTORS 09/G2 - ING-INF/06

Automated Segmentation and Non-Rigid Registration for the Quantitative Evaluation of Myocardial Perfusion from Magnetic Resonance Images

Giacomo Tarroni

SUPERVISOR
Prof. Claudio Lamberti

CO-SUPERVISOR
Dott. Cristiana Corsi

COORDINATOR
Prof. Angelo Cappello

DEIS - DEPARTMENT OF ELECTRONICS, COMPUTER SCIENCES AND SYSTEMS
JANUARY 2009 - DECEMBER 2011

Giacomo Tarroni: *Automated Segmentation and Non-Rigid Registration for the Quantitative Evaluation of Myocardial Perfusion from Magnetic Resonance Images.* Dissertation for the degree of Doctor of Philosophy in Bioengineering, March 2012.

Contents

Preface

The present Thesis describes the principal research projects pursued during my Ph.D. course. Part I is dedicated to the main research project, which consisted in the design, the implementation and the validation of an automated technique for myocardial identification as a basis for perfusion quantification in magnetic resonance images. Some of the methods developed for the main project were successfully applied also to other areas of research. More in particular, the implemented segmentation methods were adopted for myocardial identification in cine cardiac magnetic resonance images as a basis for both ventricular modelling and necrotic scars detection. These two projects, to which I have only partially contributed, are described in Part II. Finally, Part III describes a project unrelated to the field of cardiac image processing, and consists in the design and implementation of an automated segmentation technique for prosthetic components in fluoroscopy. Of note, the side projects presented in Parts II and III are described by reporting the relative papers.

The indicated research projects were pursued at the Department of Electronics, Computer Sciences and Systems of the University of Bologna and at the Cardiac Imaging Research of the University of Chicago.

Part I

Main Project

Short Abstract

MYOCARDIAL perfusion quantification by means of Contrast-Enhanced Cardiac Magnetic Resonance images relies on time consuming frame-by-frame manual tracing of regions of interest. In this Thesis, a novel automated technique for myocardial segmentation and non-rigid registration as a basis for perfusion quantification is presented. The proposed technique is based on three steps: reference frame selection, myocardial segmentation and non-rigid registration. In the first step, the reference frame in which both endo- and epicardial segmentation will be performed is chosen. Endocardial segmentation is achieved by means of a statistical region-based level-set technique followed by a curvature-based regularization motion. Epicardial segmentation is achieved by means of an edge-based level-set technique followed again by a regularization motion. To take into account the changes in position, size and shape of myocardium throughout the sequence due to *out of plane* respiratory motion, a non-rigid registration algorithm is required. The proposed non-rigid registration scheme consists in a novel multiscale extension of the normalized cross-correlation algorithm in combination with level-set methods. The myocardium is then divided into standard segments. Contrast enhancement curves are computed measuring the mean pixel intensity of each segment over time, and perfusion indices are extracted from each curve. The overall approach has been tested on synthetic and real datasets. For validation purposes, the sequences have been manually traced by an experienced interpreter, and contrast enhancement curves as well as perfusion indices have been computed. Comparisons between automatically extracted and manually obtained contours and enhancement curves showed high inter-technique agreement. Comparisons of perfusion indices computed using both approaches against quantitative coronary angiography and visual interpretation demonstrated that the two technique have similar diagnostic accuracy. In conclusion, the proposed technique allows fast, automated and accurate measurement of intra-myocardial contrast dynamics, and may thus address the strong clinical need for quantitative evaluation of myocardial perfusion.

Extented Abstract

Purpose. Cardiac magnetic resonance (CMR) is currently the standard technique for myocardial functional assessment. Myocardial perfusion analysis by means of Contrast-Enhanced CMR is performed clinically only by qualitative visual assessment. Although quantitative methods have demonstrated superior diagnostic accuracy, they rely on frame-by-frame manual tracing of myocardial regions of interest (ROIs). The resulting methodology is tedious, time-consuming and potentially inaccurate, being strongly operator-dependent. Accordingly, many automated and semi-automated technique for myocardial identification in perfusion images have been proposed in literature. However, only few of them try to compensate for respiratory *out of plane* motion, which causes apparent myocardial deformations in the imaging plane. Among these, to the best of our knowledge, none has successfully undergone an extensive validation procedure in the clinical environment. The main goal of the present project was to develop, implement and validate an automated technique for myocardial identification as a basis for perfusion quantification suitable for clinical application.

Methods. The proposed technique is based on three major steps: reference frame selection, myocardial segmentation and non-rigid registration. In the first step, after the manual input of a seed point inside the left ventricular cavity, the reference frame in which myocardial segmentation will be performed is automatically chosen. Endocardial segmentation is achieved by means of a statistical region-based level-set technique followed by a curvature-based regularization motion. Differently, epicardial segmentation is achieved by means of an edge-based level-set technique followed again by a regularization motion. After the myocardial boundaries have been defined in the reference frame, they have to be shifted and deformed to match the changes in position, size and shape of heart throughout the sequence. This task is achieved implementing a non-rigid registration method, consisting in a novel multiscale extension of the normalized cross-correlation algorithm combined with level-set methods. After the myocardium has been identified into all sequence frames, it is divided into 16 segments. Contrast enhancement curves are computed mea-

suring the mean pixel intensity of each segment over time. Perfusion indices are then extracted from each curve. The presented approach has been applied to synthetic and real perfusion sequences. As for real acquisitions, 42 patients have been analyzed both at rest and during vasodilator stress. To ensure the robustness of the implemented method, the real sequences have been acquired in two different institutions, using different equipment and different protocols. To validate the proposed automated technique, the real sequences were manually traced by an experienced interpreter. The automatically defined contours were compared to the manually traced ones by means of several error metrics including Hausdorff Distance and Mean Absolute Distance. Contrast enhancement curves extracted both automatically and manually were compared using Pearson's correlation coefficient, linear regression and Bland-Altman analyses. Perfusion indices were also compared in the same way. Finally, to evaluate the clinical usefulness of the proposed approach, the diagnostic accuracy of the perfusion indices were compared between automated and manual analyses using quantitative coronary angiography (QCA) and qualitative visual interpretation as reference standards.

Results. Time required for the automated analysis of a perfusion sequence is less than one minute. The spatial comparison of the automatically and manually defined contours resulted in errors comparable to those reported in literature. Segmental contrast enhancement curves obtained using the automated approach were in good agreement with those extracted manually. The same happened for most of the perfusion indices studied. Finally, the diagnostic accuracy of these indices were similar between automated and manual analysis both against QCA and visual inspection.

Conclusions. Despite the extreme dynamic nature of contrast-enhanced image sequences and respiratory motion, fast automated detection of myocardial segments and accurate quantification of tissue contrast is feasible at rest and during vasodilator stress. The proposed technique allows the detection of stress-induced perfusion abnormalities and yields a diagnostic accuracy comparable to that of conventional manual analysis. Consequently, it represents a viable candidate for the adoption in the clinical environment.

Chapter 1

Introduction

The leading cause of death in the world, according to the latest estimates provided by the World Health Organization [1][2], is represented by cardiovascular diseases. In 2008, the mortality due to this group of diseases exceeded the 30% of the total, and up to the 12.8% was due to ischaemic heart diseases alone (see Fig. 1.1). This last percentage is strongly related to the geographic region being analyzed: while in low-income countries it decreases to 6.1%, in middle- and high-income countries it rises up to 13.7% and 15.6%, respectively [3]. As a consequence, it becomes evident the importance of scientific research applied to this field, aiming to an improvement of both the diagnostic process and the clinical treatment of ischaemic heart diseases.

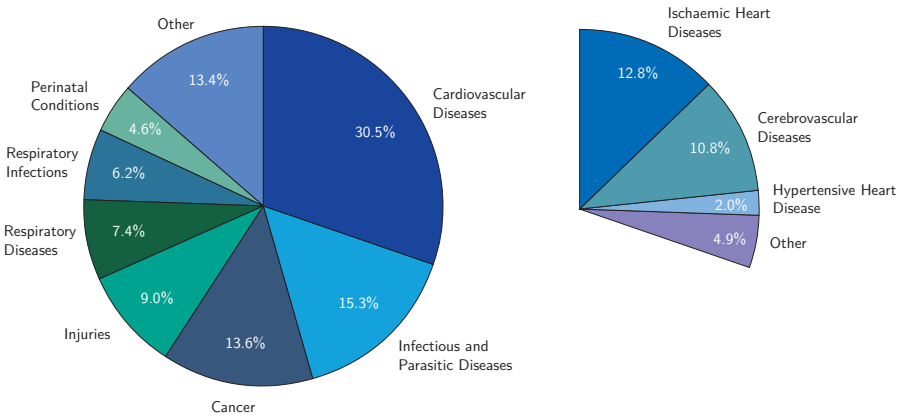

Figure 1.1: Worldwide mortality estimates for the year 2008, with particular focus on cardiovascular diseases. Data gathered from the WHO technical report and summary tables [1][2].

The assessment of patients presenting symptoms related to myocardial ischemia is one of the most common and yet challenging clinical tasks. Each

year, a large amount of patients (approximately 6 millions only in the United States [4]) presents to emergency departments with chest pain and other symptoms related to myocardial ischaemia. However, according to statistics, only approximately 20% of them are suffering from acute coronary syndrome (ACS). The initial ECG, which is routinely used as first patient assessment tool, is diagnostic in fewer than a half of the patients with ACS [5]. In addition, cardiac enzymes do not become positive for several hours after coronary occlusion. As a result, the vast majority of these patients is either admitted to the hospital or to a chest pain unit, leading to a large wasted expenditure per year (approximately $12 billion only in the United States [6]). On the other hand, up to 4% of patients with ACS are being inappropriately discharged from the emergency department [7]. Overall, almost a half of cardiac mortality due to myocardial infarction takes place before reaching the catheterization laboratory [8]. These findings indicate that, despite the many improvements in the clinical identification of myocardial ischemia, the need for fast, reliable and affordable techniques for risk stratification in averting cardiac events is still of prime importance.

Cardiac perfusion imaging is currently playing the leading role in the field of non-invasive assessment of myocardial perfusion for the detection of the presence and severity of myocardial ischaemia and of the underlying coronary artery disease (CAD). The basic principle consists in acquiring images of the heart during the inflow of an appropriate intravenous contrast medium (see Fig. 1.2).

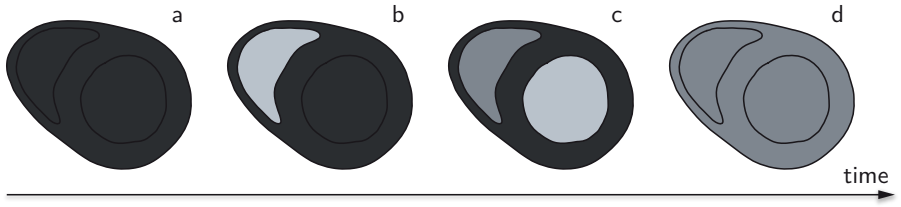

Figure 1.2: Basic cardiac perfusion image sequence (short-axis view). Initially the whole heart appears uniformly dark (a); after the contrast medium is intravenously injected into the patient's circulation, the right ventricular cavity, the left ventricular cavity and the myocardium are sequentially enhanced (b, c, d, respectively).

The visualization of the contrast medium dynamics allows the evaluation of the local myocardial perfusion in the left ventricle (LV), and thus the detection of potentially ischaemic areas. Aside from CAD detection, perfusion imaging is able to locate myocardial necrotic tissue (in case of previous myocardial infarction) and to assess viability, showing myocardial regions which could benefit

from angioplasty and revascularization. Generally speaking, all the main imaging techniques (i.e. Nuclear Imaging, Computed Tomography, Echocardiography and Magnetic Resonance Imaging) can be applied to estimate myocardial perfusion, usually at the additional cost of intravenous injection of an endogenous contrast medium. However, many of them are not routinely applied due to many reasons.

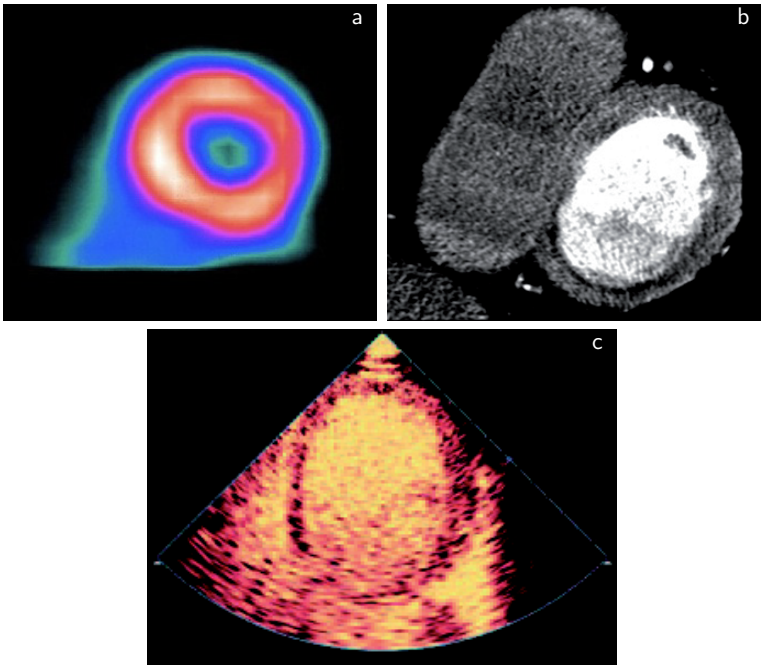

Figure 1.3: Myocardial perfusion short-axis images obtained with different modalities: SPECT (a), CT (b), MCE (c). Images respectively from Hendel *et al.* [9], Techasith *et al.* [10] and Hayat *et al.* [11].

Nuclear Imaging is one of the first imaging techniques applied to the evaluation of myocardial perfusion (see Fig. 1.3, a) [12]. It can be performed both using Single-Photon Emission Computed Tomography (SPECT) or Positron Emission Tomography (PET): the former is definitely more widespread than the latter, requiring less expensive technological facilities, albeit PET generally provides higher imaging accuracy. Due to the specific pharmacokinetics of the commonly adopted radioactive tracers, which are directly absorbed by myocardial cells, Nuclear Imaging can estimate perfusion performing a single, non dynamic acquisition of the heart few minutes after the tracer injection. Although being a well-established technique for myocardial perfusion assessment, used as gold standard for several decades [12], Nuclear Imaging for cardiac perfusion assessment suffers from many limitations. First of all, it is characterized by a relatively low spatial resolution [13], hindering the application of quantita-

tive methods which could improve diagnostic accuracy. Nuclear Imaging is also limited by different types of artifacts such as attenuation artifacts and motion artifacts (enhanced by the relatively high acquisition time, which can go up to 20 minutes per single scan). Finally, all the nuclear imaging techniques obviously require the production and the administration of a radioactive isotope to the patient, which will be exposed to ionizing radiations. Albeit some of these issues have being tackled by modern scanners [13], most of them still hold, limiting the clinical use of Nuclear Imaging for the assessment of myocardial perfusion.

Historically, Computed Tomography (CT) has not been deployed for the estimation of myocardial perfusion due to its relatively low temporal resolution, unsuitable for contrast medium dynamics imaging. Only recently, thanks to the advantages in CT technology, cardiac perfusion imaging has become feasible on this platform (see Fig. 1.3, b) [14]. However, this methodology is still at an early stage of development, and at the moment still suffers from a few image artifacts, namely beam-hardening and motion artifacts [10]. Both these types of artifacts determine the appearance hypo-enhanced regions, which could be mistaken for perfusion defects. In addition, every CT scan obviously involves the administration of a certain amount of ionizing radiation to the patient. These factors, at the present time, limit the viability of this modality and hamper its clinical adoption.

Echography is one of the most widespread imaging modalities applied to the analysis of both cardiac morphology and functionality. Myocardial Contrast Echocardiography (MCE) consists in imaging the myocardium after the intravenous injection of gas bubbles encapsulated in a solid shell and called microbubbles (see Fig. 1.3, c). MCE has proven to be very sensitive in detecting coronary stenosis, especially at mild and moderate states [15]. Moreover, MCE is a very cost-effective and safe technique. Despite all these advantages, MCE is not routinely used in clinical practice. This is mainly due to the reluctance in the approval of microbubble-based contrast agents in many Countries, including the United States [5]. On a more technical note, Echography may also be limited by the specific anatomy of the patient, being strictly dependent upon the acoustic window available and the size of the heart. Finally, MCE images are difficult to be evaluated, due to their relatively low signal-to-noise ratio. These facts considerably steepen the learning curve for this technique and limit its acceptance in the clinical environment.

Cardiac Magnetic Resonance Imaging (CMR) is currently the reference standard technique in assessing cardiac structure and function. The evaluation of cardiac perfusion with CMR is made possible through the administration of a Gadolinium-based contrast medium (GBCM), revealing myocardial blood inflow (see Fig. 1.4). To correctly estimate the dynamics of the GBCM bo-

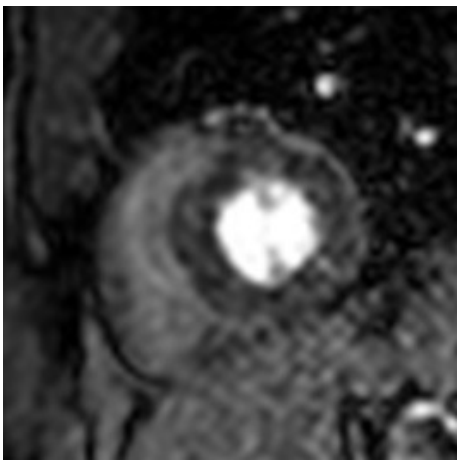

Figure 1.4: Myocardial perfusion short-axis image obtained with CMR.

lus through cardiac tissue, imaging must start right after its injection and be performed at a sufficiently high frame rate. Based on these considerations, this type of imaging protocol takes the name of First-Pass Perfusion CMR (FP-CMR). Compared to other available imaging modalities used to assess myocardial perfusion, FP-CMR is characterized by high spatial and temporal resolution, high sensitivity, relatively good image quality (with substantial absence of artifacts due to attenuation phenomena or induced by unfavorable body conditions) and an excellent safety profile [16]. These technical features are the reason of the growing fortune of FP-CMR, which can nowadays be considered the gold standard for the evaluation of myocardial perfusion and the detection of potential ischaemia. In the clinical environment, this detection is performed relying on the simple visual assessment of the acquired image sequences. Clearly, this analysis is strongly operator-dependent, and unable to identify a variety of diseases such as three-vessel CAD (consisting in a uniform stenosis of all the three coronary arteries) which induce a balanced ischemia with no visible defects [17]. A quantitative analysis, consisting in the extraction of intensity time curves from different regions of the myocardium (i.e. contrast enhancement curves), would be able to address these issues. Nonetheless, quantitative perfusion evaluation methods are not used in the clinical routine. The main reason is that the construction of contrast enhancement curves requires manual drawing of myocardial regions of interest (ROIs) in each frame of the image sequence [18][19][20]. This operation is greatly hampered by cardiac *out of plane* motion due to diaphragmatic respiration of the patient [1]. While patients are asked to hold their breath as long as they can during contrast

[1]The normal contraction/relaxation of the heart is not visible in perfusion image sequences thanks to ECG-gating imaging protocols, which allow to scan the heart at the same phase in each cardiac cycle.

administration and imaging, most of them is unable to maintain apnea for the whole scan time (usually from 30 to 60 seconds). *Out of plane* motion causes changes in position, size and shape of the myocardium throughout the sequence, which causes the need for constant repositioning and redrawing of the ROIs [21][22][23]. The resulting procedure is tedious, highly time-consuming and potentially inaccurate, thus unapplied in the clinical practice.

To overcome this issue, several image processing techniques have been proposed and presented in literature, aiming at the automated identification of the myocardium in all the frames of a FP-CMR image sequence [21][24][25]. This task is particularly difficult to achieve due to the relatively high noise levels in the images as well as the extreme changes in brightness from frame to frame of the different image components (i.e. ventricular cavities and myocardium). As a consequence, none of the presented approaches has reached widespread consensus, and the research for an automated method for myocardium identification in FP-CMR image sequences remains still open.

In Part I of this Thesis, a new approach for segmentation and registration of myocardial regions of interest as a basis for perfusion quantification is presented. This technique is based on level-set methods for image segmentation and modified normalized cross-correlation algorithms for non-rigid image registration. The approach has been tested both on synthetic image datasets and on real FP-CMR datasets acquired in patients presenting normal perfusion and CAD. For validation purposes, the implemented technique has been compared to conventional manual tracing of myocardial ROIs, both in terms of contour accuracy and of contrast enhancement curves consistency. Perfusion indices have been extracted using both automated and manual techniques, and their diagnostic accuracy has been assessed using quantitative coronary angiography and image visual interpretation as references. The results indicate that myocardial identification in FP-CMR images using this approach is feasible, fast and accurate compared to manual tracing. This technique could therefore be transferred in the clinical environment, helping the diffusion and the adoption of quantitative perfusion assessment methods based on FP-CMR.

Part I is organized as follows: Chapter 2 describes in detail the FP-CMR imaging modality; Chapter 3 presents a review of the literature regarding myocardial identification techniques on FP-CMR images; Chapter 4 introduces the level-set approach and the basic segmentation techniques based on it; Chapter 5 describes the methods for myocardial segmentation and registration implemented in the proposed technique; Chapter 6 presents the details involved in image generation and analysis, for both synthetic and real FP-CMR images; Chapter 7 reports and discusses the comparison between automatically and

manually defined myocardial boundaries; finally, Chapter 8 presents the comparison between automatically and manually extracted contrast-enhancement curves and reports the diagnostic accuracy of several perfusion indices computed with these two methods.

Chapter 2

Magnetic Resonance Imaging of Cardiac Perfusion

MAGNETIC Resonance Imaging (MRI) can nowadays be considered the modality of choice for the evaluation of cardiac morphology and functionality. Its widespread in the clinical environment has been due to the significant improvements in MRI technology occurred in the last decade, such as the design of MRI cardiac coils and the advent of parallel imaging [26]. These advancements have greatly empowered the capabilities of Cardiac MRI (also known as CMR), improving both spatial and temporal resolutions and overall image quality. Today, MRI can provide a deep insight in the heart, being able to reveal morphological details and to assess ventricular ejection fraction, wall motion, strain and, of course, tissue perfusion. In particular, tissue perfusion analysis requires the administration of a Gadolinium-based contrast medium, which is why this methodology takes the name of Contrast-Enhanced Cardiac Magnetic Resonance (CE-CMR). Depending on the specific imaging protocol used, it is possible to investigate different aspects of myocardial perfusion. More specifically, First-Pass Perfusion CMR (FP-CMR) consists in performing imaging right after the injection of the contrast medium, and in visualizing the first inflow of the bolus in the myocardial walls; Late Gadolinium Enhancement (LGE), on the other hand, consists in imaging the heart minutes after contrast injection. The former technique allows the detection of CAD, while the latter reveals necrotic areas affected by previous myocardial infarction.

This Chapter is dedicated to Contrast-Enhanced Cardiac Magnetic Resonance with particular focus on FP-CMR.

2.1 Principles of Contrast-Enhanced CMR

Contrast-Enhanced CMR is an imaging method for myocardial perfusion evaluation based on the intravenous administration of a Gadolinium-based contrast

medium (GBCM). The effects of a GBCM are to shorten the T_1 relaxation time of the protons located in its vicinities and to strongly enhance their brightness in the acquired images [16]. Gadolinium (Gd) is a highly toxic element: as a consequence, a chelation process is needed to avoid any contact between the Gadolinium ion and the tissue components and thus to allow its administration [27]. Of note, the first chelating agent for Gadolinium was DTPA (diethylene-triamine-pentaacetic acid), which is even today the most adopted one [28]. Differently from the contrast media used in Nuclear Imaging, Gadolinium compounds currently approved for the use on patients are extracellular, i.e. there is almost no GBCM uptake from normal myocardial fibers. Therefore, the only way to gather information about myocardial blood flow is to perform imaging at a frame rate high enough to visualize the initial inflow of the contrast medium in the myocardial tissue. This method is accordingly called First-Pass Perfusion CMR (FP-CMR), and permits to locate areas of the myocardium potentially supplied by a reduced blood flow, which is usually caused by underlying CAD. An example of an FP-CMR image sequence is presented in Fig. 2.1).

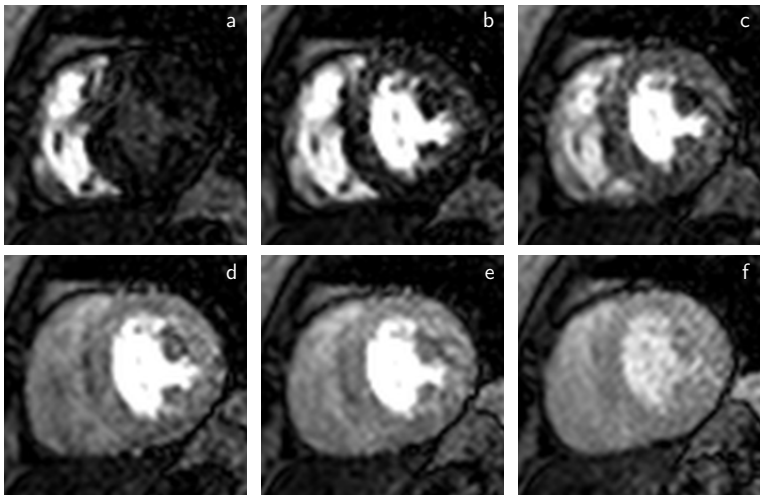

Figure 2.1: First-Pass Perfusion Cardiac Magnetic Resonance image sequence (from a to f): short-axis view of a normal subject during cardiac stress.

The detection of CAD with FP-CMR is performed in two different phases, one during cardiac stress and one at rest. Cardiac stress is usually pharmacologically induced through the administration of a vasodilator such as adenosine, dipyridamole or regadenoson [16], although some studies have reported that physical exercise performed right before image acquisition might be a better method in terms of both induced cardiac conditions and safety of the patient [10]. Stress imaging works via coronary steal phenomenon: normal coronary

arteries dilate more than their diseased counterpart, leading to a difference in flow in the downstream myocardium and highlighting the perfusion defect in the territory supplied by the diseased artery (see Fig. 2.2). Through the comparison of perfusion defects between stress and rest acquisitions, it is possible to identify and separate stress-induced ischaemic regions from fixed non-perfused areas. This insight into myocardial blood supply is of prime importance in order to take decisions about potential angioplasty or other treatments for CAD. To further determine whether a particular fixed defect corresponds to hibernated tissue (due to chronic hypo-perfusion) or to necrotic tissue, it's possible to exploit GBCMs particular pharmacokinetic properties. Because of the severe structural alterations which occur after myocardial infarction, contrast wash-out time for necrotic tissue is substantially higher than for intact (and thus viable) tissue [28]. This difference in concentration reaches its maximum after 10-15 minutes after contrast medium injection. The Late Gadolinium Enhancement (LGE) technique consists in imaging the heart after this time delay, allowing to assess myocardial viability and to estimate the benefits achievable through revascularization. Importantly, FP-CMR (at stress and rest) and LGE can be performed during the same imaging session, providing deep and comprehensive insight in myocardial perfusion and vascularization, which are the basis for cardiac functionality.

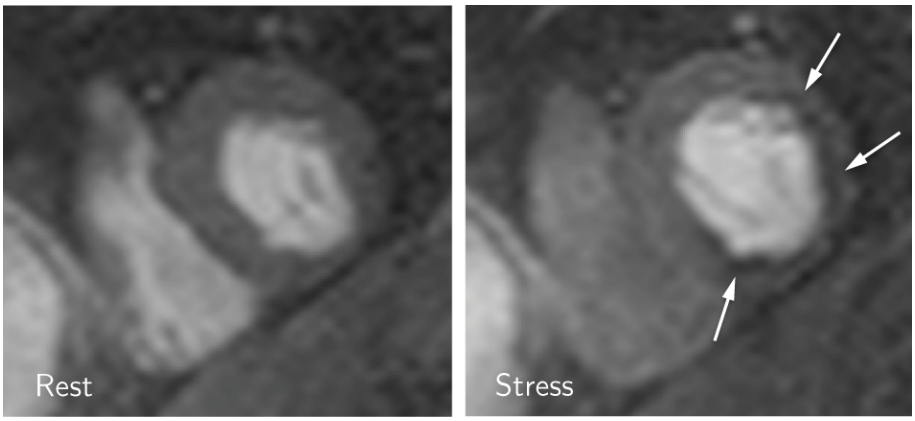

Figure 2.2: First-Pass Perfusion Cardiac Magnetic Resonance images in short-axis view at rest (left) and at stress (right) in a patient with CAD. While perfusion appears to be normal at rest, stress-induced defects are visible in the antero-lateral, lateral, inferior and infero-septal segments.

2.2 Diagnostic and Prognostic Performances

Several studies have analyzed the diagnostic performance of these imaging techniques and have demonstrated that contrast-enhanced CMR consists in

a powerful tool in evaluating the spectrum of CAD [16]. Diagnostic accuracy of FP-CMR against invasive Quantitative Coronary Angiography (QCA) has been reported by many initial single-center studies. Ishida *et al.* [29] have analyzed 84 patients and found sensitivity (SE) 90% and specificity (SP) of 85% for coronary stenosis luminal narrowing equal to 50% or more. Other studies have reported similar results [18][30]. These studies were followed by multi-center studies, providing better insight in the diagnostic capabilities of FP-CMR. Wolff *et al.* [31] performed a Gadolinium dose-ranging multi-center study on 99 patients and reported an overall SE of 93% and SP of 75%. Giang *et al.* [32] found identical diagnostic accuracy in a multi-center study of 94 patients. More recently, the much larger *Comparison of Perfusion-cardiac Magnetic Resonance with Single-Photon Emission Computed Tomography for the Detection of Coronary Artery Disease (MR-IMPACT)* trial was performed by Schwitter *et al.* [33]. In this study, 234 patients in 18 different centers were evaluated, and FP-CMR showed SE of 85% and SP of 67%. Finally, a meta-analysis of more than 1180 patients from 37 studies analyzed by Nandalur *et al.* [34] showed SE of 91% and SP of 81%. Similar findings were reported in another meta-analysis performed by Hamon *et al.* [35]. All these results underline the high diagnostic power of FP-CMR, and explain the reason why it is gaining more and more attention in the clinical practice.

The prognostic capabilities of FP-CMR have been assessed by several studies. Ingkanisorn *et al.* [36] evaluated 135 patients presenting to the ED with chest pain but no elevation of troponin I. They reported SE of 100% and SP of 93% for stress CMR perfusion in detecting adverse cardiac outcomes at 1-year follow-up. The cost-effectiveness of stress CMR for the assessment of patients presenting acute chest pain was analyzed in a prospective, randomized, controlled trial comparing CMR to standard inpatient evaluation [37]. The study included 110 patients at intermediated or high probability for ACS, but without ECG or biomarker evidence of infarction. The patients assessed with CMR presented a significantly lower median hospitalization cost, and 79% were managed without hospital admission. In either randomized groups, no adverse clinical outcomes were found at 1-month follow-up, suggesting that CMR evaluation was cost-effective in this clinical setting.

2.3 Comparison with Nuclear Imaging

As already mentioned, when compared to other imaging modalities for myocardial perfusion assessment, FP-CMR features high spatial and temporal resolution, high sensitivity, relatively good image quality (lacking artifacts due to attenuation phenomena or induced by unfavorable body conditions) and an excellent safety profile [16]. When compared to SPECT, which is the main

clinically adopted alternative, FP-CMR presents 3- to 4-fold higher spatial resolution, allowing superior myocardial tissue visualization and outstanding endocardial border definition (which is the area usually suffering earlier in case of infarction). This feature allows the deployment of a variety of quantitative methods for perfusion measurement, which is more difficult to be achieved in SPECT. These methods permit the diagnosis of a variety of diseases (such as three-vessel disease) which produce a uniform reduction in blood flow in the whole myocardium and thus no visible defects. The higher temporal resolution of FP-CMR makes contrast dynamics imaging possible, while SPECT produces one fixed image, thus providing less information about myocardial perfusion. Contrary to SPECT, FP-CMR is not daunted by attenuation artifacts, and can handle motion artifacts in a better fashion (thanks to higher sampling frequency). Time required for one complete SPECT perfusion exam is usually higher than for FP-CMR [16]. Finally, SPECT imaging involves patient exposure to potentially harmful ionizing radiations, which are absent in FP-CMR. Overall, FP-CMR has demonstrated higher diagnostic accuracy over SPECT, as reported by many studies. Among them, Schwitter *et al.* [33] showed that FP-CMR presents superior diagnostic performance compared to SPECT using QCA as reference standard, and reported an area under the ROC curve of 86% vs 75% for FP-CMR and SPECT, respectively. PET has higher spatial and temporal resolution, providing better diagnostic performance than SPECT. FP-CMR and PET have shown high correlation [38]. However, PET imaging is a very expensive technique, which is not cost-effective in many clinical scenarios, and still requires the administration of radioactive tracers to the patient. FP-CMR also suffers from some limitations. The usual list of biomedical metallic devices for which magnetic resonance imaging is contraindicated still applies, although an MR-compatible pacemaker model is now FDA approved and commercially available [39]. The use of GBCMs has been associated with a serious complication called as nephrogenic systemic fibrosis (NSF) [40]. However, recent studies have highlighted the fact that NSF is a rare complication which occurs primarily in patients with strongly compromised renal function and in those with concurrent acute illnesses [41]. The chances of NSF occurrence seem to be substantially lower with newer cyclic-structured Gadolinium compounds, and pre-scan analysis are now usually performed in high-risk patients in order to estimate glomerular filtration rate. As a result, new cases of NSF from GBCM injection have been extremely rare in recent years [16].

2.4 Qualitative vs Quantitative Analysis

First-pass perfusion may be estimated either qualitatively or quantitatively. The former approach completely relies on visual assessment; the latter is based

on the definition of myocardial regions of interest (ROIs) in each frame of the sequence and on the measurement of intensity changes of the ROIs. More specifically, the changes of the mean intensity of the pixels comprised in each ROI over time during the contrast bolus in-flow in the tissue are computed (see Fig. 2.3). The resulting curve is often called contrast enhancement curve.

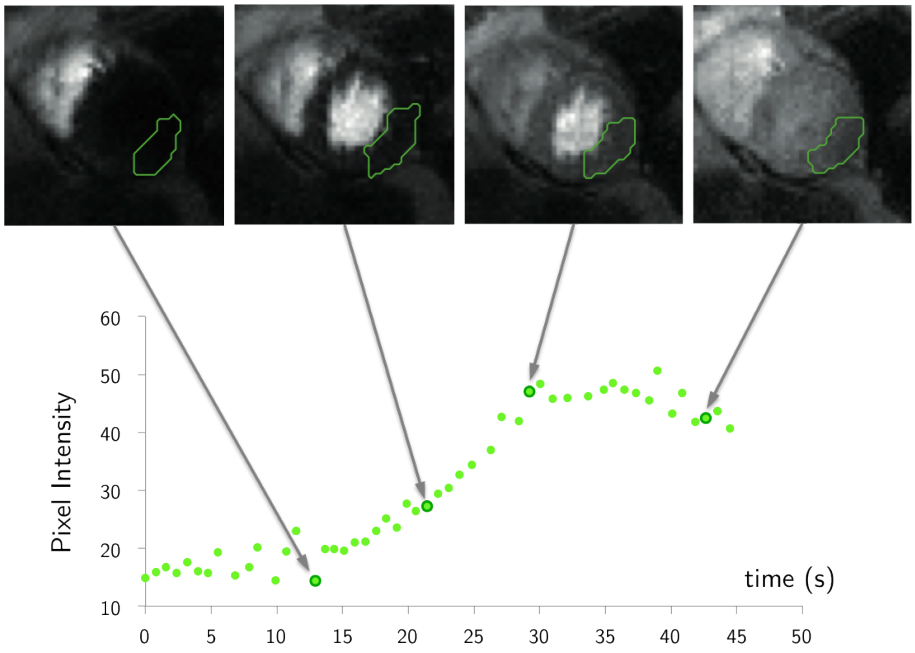

Figure 2.3: Extraction of a contrast enhancement curve from a myocardial ROI.

From these curves it is possible to compute several indices reflecting myocardial perfusion. Most common indices are peak-to-peak amplitude (i.e. intensity difference between baseline level and maximum peak), rate of contrast enhancement (upslope of the curve during the enhancement phase) and area under the curve (computed from baseline to maximum peak) [18][42][43]. The obtained values allow the comparison of perfusion findings not only from different ROIs of the same patient, but between different patients. To this aim, indices normalization by the respective left ventricular cavity value is performed. Moreover, ratios between values obtained at stress and at rest are usually computed, in order to assess myocardial perfusion reserve (formally defined as the ratio of myocardial blood flow between stress and rest). More complex methods have also been deployed to measure myocardial blood flow and perfusion reserve, such as deconvolution models based on data interpolation with a Fermi function [43]. All these techniques permit a more objective perfusion estimate, and the detection of a variety of CAD which induce a balanced ischemia with no

visible defects (such as three-vessel disease).

In the clinical practice, FP-CMR image sequences are usually qualitatively evaluated by visual assessment alone, due to the extremely heavy time burden required to manually trace ROIs onto all the frames of acquired image sequences. However, qualitative analysis is strongly operator-dependent and error-prone. Accordingly, several studies indicate that the diagnostic performance of quantitative methods is higher compared to qualitative visual assessment. Patel *et al.* [17] have recently directly investigated this issue in 30 patients, and found that quantitative analysis and visual assessment had respectively an accuracy of 83% vs 80% to detect stenoses greater than 50%, and 77% vs 67% for stenoses greater than 70% (although the differences were not always statistically significant). Importantly, the quantitative analysis was able to correctly detect three-vessel CAD, differently from visual assessment. Moreover, agreement between observers for quantitative analysis was higher than for qualitative assessment. All these outcomes suggest the importance of performing quantitative measurements on FP-CMR images rather than relying solely on the operator's eyes.

Chapter 3

State of the Art of Perfusion Assessment in CMR

The estimation of local myocardial perfusion is nowadays routinely performed by means of First Pass Perfusion CMR (FP-CMR) in many clinical facilities. The detection of myocardial hypo-enhanced areas is done by cardiologists and radiologists, which usually rely solely on the visual inspection of the image sequences to perform their analysis. Quantitative analysis, which would provide more reliable and efficient results [17] requires the definition of myocardial ROIs in each frame of the image sequences. Unfortunately, despite the presence of commercially available software designed for this purpose, ROIs definition requires their manual tracing in many different frames of the sequence to account for respiratory motion. The resulting procedure is cumbersome and strongly time-consuming, and as a consequence is usually not applied in the clinical environment. Accordingly, in the last decades many image processing methods have been presented to semi-automatically or automatically identify myocardial ROIs on FP-CMR image sequences. The most common approach is based on the combination of two independent steps: myocardial segmentation and myocardial registration. Myocardial segmentation consists in the definition of the boundaries of the left ventricular myocardium in a specific frame. Within the limits of myocardial perfusion image sequences, myocardial registration consists in the modification (either by simple translation or translation and deformation) of the sequence frames in order to offset the visible cardiac motion. Different proposed methods involve a different order in the application of these two steps, while, on the other hand, some methods apply hybrid approaches in which the definition of myocardial ROIs is performed at the same time for all the frames of the analyzed sequence.

In this Chapter, the state of the art in myocardial perfusion assessment by means of FP-CMR will be presented. First, the methods used in the clinical environment will be described, then the main automated techniques for my-

ocardial segmentation and registration already reported in literature will be presented.

3.1 Perfusion Evaluation in the Clinical Environment

Clinical routine for perfusion evaluation from FP-CMR image sequences is based on visual assessment. Because of the relatively high noise level of the images, which can induce the appearance of false hypo-enhanced areas, usually a persistence of at least three consecutive frames is required to identify a perfusion defect [29]. Although most of the time the analysis is limited to the detection of the defects, it is also possible to grade them with a score reflecting either their severity or their extension [29][31]. Visual assessment is a fast and effective way of evaluating perfusion sequences, but strongly relies on the experience of the interpreters. Moreover, this approach is very limited in comparing results obtained from different patients and does not allow the detection of perfusion defects uniformly distributed onto the whole myocardium, such as three-vessel disease and microvascular dysfunction (for instance caused by diabetes mellitus). At the present time there are several commercially available software designed to help the physician in the visualization and analysis of MRI images. The main examples are Cardiac Specialist CX®(sponsored by Philips, Best, Netherlands [44]) and Argus Dynamic Signal®(sponsored by Siemens Healthcare, Erlangen, Germany [45]). Both these software products feature automated or manual segmentation and registration functions, which, when unable to achieve optimal results, still offer a valuable help to the operator in identifying the myocardial ROIs throughout the frames of the examined sequence.

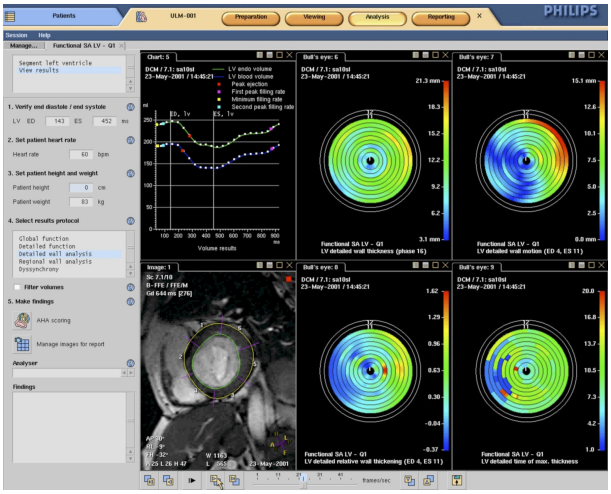

Figure 3.1: Screenshot of Cardiac Specialist CX [44].

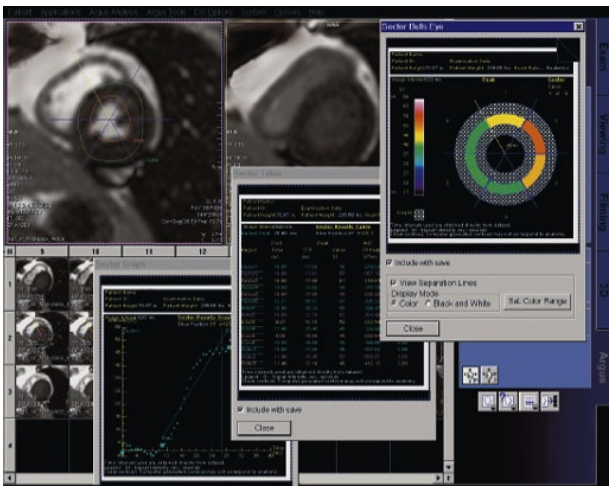

Figure 3.2: Screenshot of Argus Dynamic Signal [45].

3.2 Research in Myocardial Segmentation

The automated segmentation of the myocardium (i.e. the identification of the endocardial and epicardial boundaries of the left ventricle) in perfusion images is a non trivial task due to the nature of FP-CMR, which is characterized by relatively low spatial resolution, high noise levels and lack of well-contrasted boundaries at the left ventricular (LV) cavity - myocardium and myocardium - right ventricular (RV) cavity interfaces. Moreover, the different image components change drastically in brightness throughout the sequence due to the contrast medium dynamics, thus automated segmentation methods are likely to successfully identify the myocardium only in a limited amount of frames. As a consequence, the most common approach involves the selection (either in a manual or automated fashion) of a reference frame suitable for the specific myocardial segmentation technique. Finally, the presence of papillary muscles inside the LV cavity, which exhibit the same intensity values of the myocardium throughout the sequence but have to be included in the endocardial boundary, further hinders reliable myocardial segmentation.

Many different segmentation techniques have been proposed in literature. The first attempts have been done by means of simple image arithmetics, morphologic operators, thresholding and region growing. A combination of these approaches has been presented also very recently by Weng *et al.* [46]: their method consists in the manual selection of four specific sequence frames (depicting respectively the pre-contrast phase, the LV cavity enhancement peak, the RV cavity enhancement peak and the myocardium enhancement) after image registration. The segmentation procedure allows the detection of both LV

and RV cavities and the myocardium, but is dependent on many empirically chosen parameters and some strong constraints (i.e. elliptic fitting and myocardial thickness), which might prevent the deployment of this method in the clinical daily routine.

Santarelli *et al.* [47] presented an active contour approach featuring nonlinear anisotropic diffusion filtering and a Gradient-Vector-Flow-based snake model, which relies on the edges of the image to detect boundaries. The required manual input is a rough selection of the desired endocardial boundary. This approach suffers from all the limitations of snake models, namely sensitivity to the initialization curve and difficulty in progressing into boundary concavities, which are extremely common in LV cavities showing papillary muscles.

Shape prior-based techniques have often been adopted for myocardial segmentation: for instance, Gupta *et al.* [25] implemented an Active Appearance Models (AAMs) segmentation algorithm. Formally, AAMs establish a compact parameterisation of the variability of a desired object as learned from a representative training set. For myocardial segmentation, this involves the manual tracing of endo- and epicardial boundaries in a training image dataset. The modelled object properties are shape and pixel intensity. When applied to an unseen image, the algorithm synthesizes object instances with all possible combinations of acquired shape and pixel intensity. All the instances are fitted into the image allowing changes in position, orientation and scale. Finally, the best fitting instance is selected applying a least squares-based criterion based on the minimization of the root mean square error (MSE) between the image and the instance itself. AAMs require an initialization step which consists in initial guesses of position, rotation and scale: in the work by Gupta *et al.* this information is produced by a previously applied registration algorithm. The main disadvantage in the application of methods based on shape priors, such as AAMs, is the requirement of the manual tracing of a training set. Importantly, the shape and inner proportions of the myocardium can greatly vary in case of diseases such as hypertrophic or dilated cardiomyopathies, which would difficultly be addressed by prior-based segmentation approaches.

To date, the most advanced approach for myocardial segmentation in perfusion images consists in active contour techniques based on level-set methods. Li *et al.* [48][23] developed a comprehensive approach which combines five different terms into one energy functional for minimization. The five terms are a region based term, which incorporates a statistical model of the gray level distribution (approximately Gaussian) of the different regions; an edge-based term attracting the contour to the boundaries between different regions; a shape-prior term forcing the contour to resemble an elliptical shape (allowing inclusion of papillary muscles inside the endocardial boundary); a smoothness

term controlling the smoothness of the contour; and a thickness constraint term penalizing uneven myocardium thickness. The weighting factors, controlling the contribution of each term, are adjusted exploiting an annealing algorithm. This approach is affected by the common risk in level-set method of stopping at local minimum; furthermore, the exploitation of a shape prior and thickness constraint energy functionals might fail in detecting the boundaries of a diseased myocardium.

3.3 Research in Rigid Myocardial Registration

The automated registration of the myocardium (i.e. the modification of the sequence frames in order to offset cardiac *out of plane* motion due to patient respiration) in perfusion images is a challenging task which has been faced by the scientific community for more than a decade. The main reasons hampering its accomplishment are the high degree of motion and apparent deformation the imaged heart can undergo due to respiratory motion as well as the extreme changes in brightness of the different image components throughout the image sequence. These reasons, combined to the aforementioned relatively poor image quality and resolution, have so far impeded the development and implementation of a standardized technique for myocardial registration.

Registration methods presented in literature can be divided between rigid and non-rigid registration approaches. One of the first rigid registration algorithms was proposed by Bidaut and Vallée [49]. Their algorithm consisted basically in defining a ROI around the myocardium in a manually selected reference frame and then applying translations and rotations to the other frames minimizing the mean square error (MSE). A similar method was applied by Dornier et al [50], which restricted the ROI to the myocardium alone, cutting off the LV cavity. The biggest limitation of these works is that due to the huge changes in brightness of the image elements during contrast inflow, it is unlikely that all the sequence frames will be correctly registered to one single reference.

To overcome this issue, Gupta et al [51] chose to rigidly register each frame to the preceding one using cross-correlation as a similarity measure.

Years later, Adluru *et al.* [21] proposed a model-based approach to perform at once the registration of the whole sequence. The idea behind model-based methods is to exploit the fact that for perfectly registered perfusion images the intensity curves for each pixel are relatively smooth in time. As a consequence, a smooth model of the curve can provide a measure of motion by identifying outliers. The model chosen for pixel intensity variation in time consists in a two-compartment exponential one, using the enhancement in the RV cavity as input function. Applying this model to the acquired images allows the creation

of a "model sequence", in which each pixel undergoes an intensity change in time following its own computed model curve. Finally, rigid registration is performed between each pair of images (acquired one and modelled one) using MSE as similarity measure. Basically the same technique has been adopted by Weng *et al.* [46]. There are many problems with this approach. First of all, curves are naturally noisy due to poor image quality, and correct model fitting is always a complex and delicate operation. The major pitfall, though, is that pixel located at the boundary between the background and an enhancing structure will display a very erratic intensity curve, making extremely hard to tell to what image component the pixel itself belongs. As a result, the modeled image sequence will have blurred boundaries, which will worsen the upcoming registration step.

Milles *et al.* [24] presented a novel registration approach based on the application of Independent Component Analysis (ICA). ICA is a blind source separation method able to decompose measured mixed signals into a set of statistically independent sources and their corresponding weights. Applying this technique to a perfusion sequence allows the generation of feature images, each one corresponding to an extracted independent component (ICs, which are, as for the work of Milles *et al.*, RV cavity, LV cavity and background), and the computation of their intensity curve in time. With these data it is possible to create a modeled sequence to which the acquired sequence is registered by means of normalized cross-correlation. The whole process is repeated twice using a multiresolution approach to improve accuracy and computation time. The same ICA-based registration strategy has been adopted also by Gupta *et al.* [25]. Although formally very elegant, this technique is haunted by the same limitations seen for model-based approaches: computed ICs are likely to feature blurred boundaries, hampering proper alignment.

3.4 Research in Non-rigid Myocardial Registration

The adoption of rigid registration methods has been usually justified stating that respiratory motion is likely to cause *out of plane* cardiac movements of low entity, not requiring a non-rigid registration procedure. However, many recent studies have proved that in the clinical environment, especially for elder patients undergoing stress imaging, respiratory-induced myocardial deformation can often become of relevant intensity (see Fig. 3.3) [22][23]. While it can be agreed that "*the inherent concept behind perfusion imaging is to image the same location in the heart muscle and to follow the perfusion of a tracer in it. If the shape of the myocardium varies for a given frame, such a frame violates this underlying principle of perfusion imaging and as such might be ignored*" [24], it is also true that none of the rigid registration methods examined

features a "deformation scoring" step, allowing the automatic exclusion of the frames with excessive deformation. As a consequence, the extracted perfusion values, in those frames, would be corrupted.

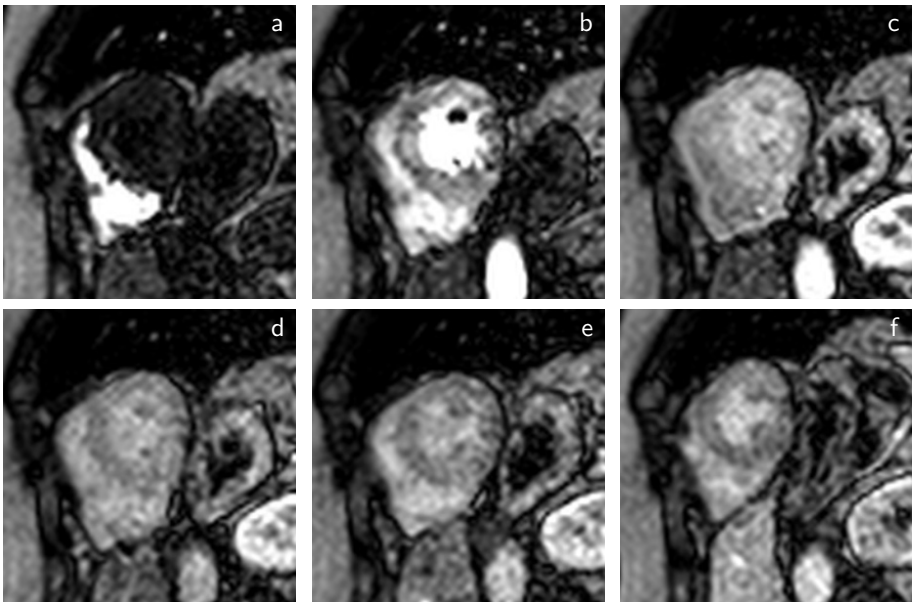

Figure 3.3: FP-CMR image sequence frames (from a to f) showing a high level of respiratory-induced myocardial deformation.

In the last years a couple of non-rigid registration algorithms have been proposed in literature. Olafsdottir *et al.* [52] presented a technique based on Normalized Mutual Information (NMI). NMI is a well-known algorithm often used for non-rigid registration between intermodality images. Importantly, however, it relies on a consistent material-intensity mapping over the whole image domain and does not account for the local intensity change, which is of crucial importance in FP-CMR. In addition, the evaluation of MI is very expensive in computational terms.

Wollny *et al.* [22] proposed a scheme that exploits the quasiperiodicity of free breathing to decouple movement from intensity changes and thus to substitute a single registration step with two easier ones. An automated algorithm detects the breathing cycle from the acquired images. It is then possible to firstly register frames corresponding to the same breathing phase (which will display evident changes in intensity but negligible motion), to linearly combine these registered frames to create synthetic references, and finally to register to them the remaining frames (thus dealing with considerable motion but similar intensity distribution). The similarity measure used in the first registration step is the sum of squared differences, and the one used in the second one is Normalized Gradient Fields. The reason behind this choice is that the former

deals well with intensity changes but lacks in accounting for shape variations, while for the latter is viceversa.

One of the most complex and evolved works about myocardial registration has recently been published by Li *et al.* [23]. The proposed approach consists in generating a *pseudo-ground truth* sequence, which is a copy of the original one with motion and noise reduced as much as possible and will be used as reference for the registration process, thus facilitating the task. The rationale is that a motion- and noiseless sequence satisfies spatiotemporal smoothness constraints: in the spatial domain, in absence of motion, homogeneous regions remain such in all the other frames; similarly, in the temporal domain, pixel intensities evolve smoothly in time. The implementation is based on an expectation-minimization approach, in which the functional to be minimized depends from the observed sequence, the pseudo-ground truth and a non-rigid deformation function. This functional consists of three terms: a data fidelity term, measuring the sum-squared intensity difference between the pseudo ground-truth and the non-rigidly deformed sequence; a spatial smoothness constraint penalizing the intensity difference between neighboring pixels of the same tissue type; and a temporal smoothness constraint penalizing the first order derivative (for background and pre-contrast periods) and second order derivative (for pixels undergoing contrast-enhancement, in order to have approximately piece-wise linear enhancement curves). The registration process is the edge-emphasized demons algorithm, which is an optical flow-type method. The major pitfall of this elaborated approach is that, in order to be effective, it relies on a first, coarse rigid registration step which, as stated by the authors themselves, is unable to deal with significant elastic deformation. Furthermore, there is the need of the manual selection of a reference frame and a reliable myocardial segmentation in order to identify the different image components.

3.5 Hybrid Approaches

Although the vast majority of the techniques reported in literature consist in registering the image sequence and in segmenting one single frame, there are a couple of approaches aiming at directly segmenting the myocardium into all image frames, implicitly accounting for respiratory motion. Stegmann *et al.* [53] applied the aforementioned Active Appearance Models (AMMs) to the whole sequence. Their approach features the definition of a myocardial shape including also the RV cavity, a multislice implementation (applying constraints on the choice of an AAM instance for a single slice based on the instances of the other slices) and a realistic pixel intensity search space (applying constraints based on the known dynamics of the contrast medium in ventricular cavities and in the myocardium). Of course, the already stated limitations for shape

prior-based methods still hold.

Finally, Mahapatra and Sun [54] proposed a Markov Random Field (MRF)-based method to integrate segmentation information for the registration. MRFs have been previously used in order to formulate the elastic registration of natural and medical images as a discrete labeling problem. Each label defines the joint occurrence of displacement vectors (used for registration) and segmentation class (semantically separating the different myocardial components). The cost function is formulated as a combination of the mutual dependence of registration and segmentation information at every label. The data penalty includes image intensity and gradient information similarity measures. This discrete formulation allows the deployment of a multiresolution graph-cut technique to reduce the computation time.

Chapter 4

Level-set Techniques

The level-set approach has been a groundbreaking leap forward in the world of image segmentation and, in general, of image processing. Firstly introduced by Stanley Osher and James A. Sethian in 1988 [55], it has been developed in the following years, initially by the authors themselves who provided a more detailed mathematical framework [56], and later by a vast number of researchers. Specifically, level-set techniques are mathematical and computational techniques describing the evolution of a contour. When compared to other approaches, they have the advantages of accurately accounting for complex evolution fields, handling implicitly topological merge and splitting events and working in an arbitrary number of dimensions. The applications of the level-set approach are innumerable: object detection, computational geometry, fluid mechanics, computer vision, materials science and so on. Clearly, level-set techniques have also been exploited and implemented to address a large variety of issues in the field of biomedical image processing, most of all in the identification of biological structures and objects.

In this Chapter, the basic concepts behind level-set techniques will be described [56]. Initially, the general definition and mathematical framework will be presented, including a specific paragraph on the main fields able to drive the contour evolution. Then, the main categories of level-set methods will be introduced, with specific focus on the ones adopted in the proposed myocardial segmentation and registration techniques.

Importantly, an extensive description of the level-set approach, including the most important issues related to its implementation, go beyond the aim of the present Thesis. To deeper delve into these topics, please refer to the dedicated book of James A. Sethian entitled *Level Set Methods* [57] and the PhD Thesis of Xavier Bresson entitled *Image Segmentation with Variational Active Contours* [58].

4.1 General Approach

Let Γ be a closed curve defined on a two-dimensional space $\Omega \subseteq \mathbb{R}^2$ and let Ω_i and Ω_o the regions inside and outside of the curve itself, respectively. This curve can be represented as a zero level-set of an implicit function $\phi : \Omega \to \mathbb{R}$ called *level-set function* and defined by

$$\begin{cases} \phi < 0, & \forall (x, y) \in \Omega_i \\ \phi = 0, & \forall (x, y) \in \Gamma \\ \phi > 0, & \forall (x, y) \in \Omega_o \end{cases} \tag{4.1}$$

or, more concisely, by $\Gamma = \phi^{-1}(0)$ (see Fig. 4.1). The main idea behind the level-set approach is to represent the evolution in time of the curve Γ as the evolution of the associated level-set function ϕ, formally $\Gamma(t) = \phi(t)^{-1}(0)$.

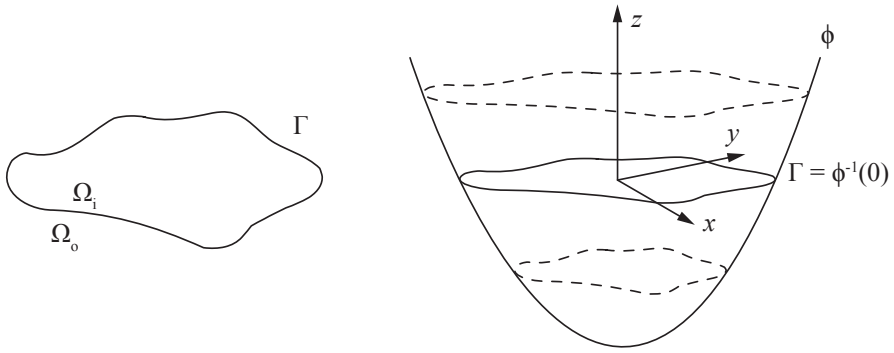

Figure 4.1: Definition of a curve Γ as zero level-set of a function ϕ.

As a consequence, it is possible to control the propagation of curve acting exclusively on the associated surface and driving its evolution. To this aim, it is useful to define few local geometrical quantities, specifically the unit normal vector and the mean curvature of the level-set curves of the surface ϕ. The unit normal vector to the level-set curves is given by

$$\mathbf{n} = \frac{\nabla \phi}{|\nabla \phi|} \tag{4.2}$$

since the gradient operator

$$\nabla \phi = \left(\frac{\partial \phi}{\partial x}, \frac{\partial \phi}{\partial y} \right) \tag{4.3}$$

is always perpendicular to level set curves and points towards higher values of ϕ. Accordingly, $\mathbf{n}$ is the outer-pointing unit normal vector.

The mean curvature is defined as

$$\kappa = \nabla \cdot \mathbf{n} = \nabla \cdot \left(\frac{\nabla \phi}{|\nabla \phi|} \right) \tag{4.4}$$

and from a geometrical point of view it represents the inverse of the curvature radius. Positive values for κ represent convex regions, while negative values represent concave ones; high values for $|\kappa|$ represent regions with a small curvature radius, while low values represent regions with a high curvature radius. As an example, Fig. 4.2 shows these two geometrical quantities for two different points belonging to the zero level-set curve Γ.

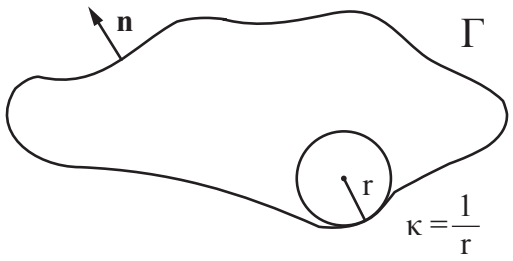

Figure 4.2: Unit normal vector $\mathbf{n}$ and curvature κ for two points of the curve Γ.

The general geometric evolution equation for the level-set function $\phi = \phi(x, y, t) : \Omega \times [0, \infty) \rightarrow \mathbb{R}$ is

$$\phi_t + \mathbf{V} \cdot \nabla\phi = 0 \tag{4.5}$$

where $\mathbf{V}$ is the velocity vector field, which is defined in Ω and can be decomposed as $\mathbf{V} = V_n\mathbf{n} + V_t\mathbf{t}$, being $\mathbf{t}$ the unit tangent vector to the level-set curves of ϕ. Of note, the components are both functions with domain in Ω: $V_n = V_n(x, y)$ and $V_t = V_t(x, y)$. By replacing in equation (4.5) $\mathbf{V}$ with its definition, the evolution equation becomes

$$\phi_t + (V_n\mathbf{n} + V_t\mathbf{t}) \cdot \nabla\phi = 0 \tag{4.6}$$

Finally, the scalar product can be resolved replacing $\mathbf{n}$ with the definition given in equation (4.2), and noticing that by definition $\mathbf{t} \perp \nabla\phi$. As a result, the final expression of the so called *level-set evolution equation*, along with the initial condition for ϕ, is

$$\begin{cases} \phi_t + V_n|\nabla\phi| = 0, & \text{in } \Omega \times (0, t) \\ \phi(x, y, 0) = \phi_0, & \text{in } \Omega \end{cases} \tag{4.7}$$

where it is evident that, in order to drive the evolution of the surface and thus of its zero level-set, it is necessary to act on V_n.

4.2 Basic Evolution Fields

According to equation (4.7), the normal component V_n of the velocity vector plays the role of a pushing/pulling force applied to the surface ϕ, acting on

planes parallel to Ω and for all the values $(x, y) \in \Omega$. Depending on the choice of the adopted V_n, different types of evolution can be implemented.

Evolution at constant speed. In this simple case, V_n is replaced by a constant value F:

$$V_n = F \tag{4.8}$$

As a consequence, all the points of the surface ϕ move along the local unit normal vector at a constant speed (see Fig. 4.3). The direction of motion depends on the sign of F.

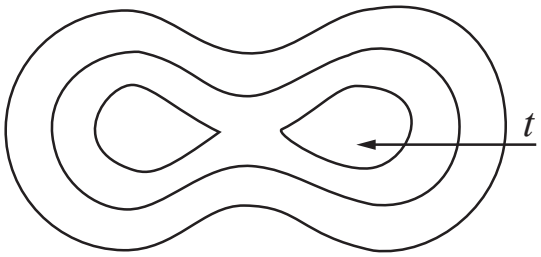

Figure 4.3: Evolution at constant speed.

Evolution per curvature. In this case, V_n is equal to the opposite of mean curvature:

$$V_n = -\kappa \tag{4.9}$$

Curvature is a local geometrical quantity: as a consequence, regions of the surface with small curvature radius move faster than regions with a higher radius (see Fig. 4.4). The direction of evolution is locally defined by the curvature's sign. Importantly, curvature changes during the motion itself, thus modifying the evolution field in time. Based on this intuition, it is possible to enunciate the Grayson's theorem, which states that "*a smooth closed curve evolving at a speed equal to its curvature will become convex in a finite amount of time*" [59].

Evolution per advection. In this case, V_n is equal to the scalar product between $\mathbf{n}$ and an external vector field:

$$V_n = \mathbf{n} \cdot \mathbf{U} \tag{4.10}$$

The vector field $\mathbf{U}$ can be defined in order to achieve the desired surface motion (see Fig. 4.5).

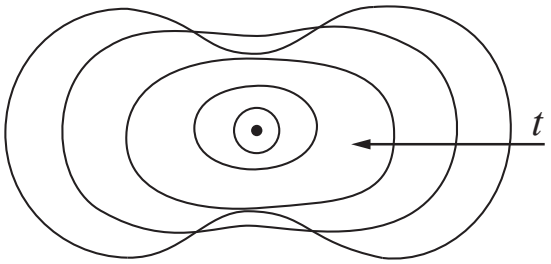

Figure 4.4: Evolution per curvature.

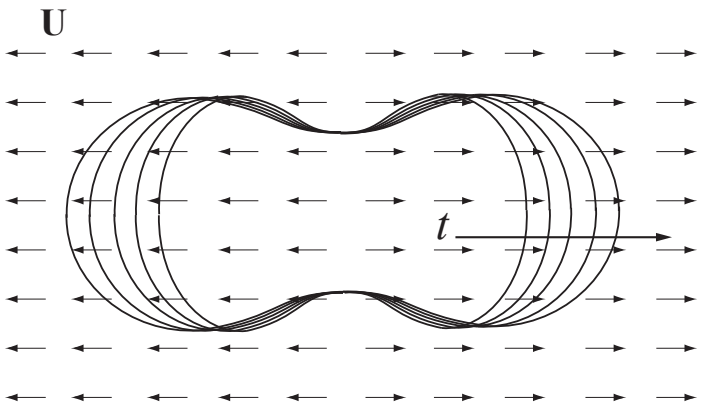

Figure 4.5: Evolution per advection.

4.3 Edge-Based Level-Set Methods

The presented level-set framework can be applied to the problem of image segmentation. Through the years, a large number of different techniques have been proposed to address this issue. These techniques can be divided into two different categories: edge-based methods and region-based methods. Edge-based methods are segmentation techniques which rely on the edges present in the analyzed image in order to perform the segmentation; on the contrary, region-based methods rely on the pixel intensity distribution of the regions respectively inside and outside the evolving contour. In this paragraph, the edge-based approach will be discussed, focusing specifically on the Malladi-Sethian example, while the region-based techniques will be presented in the following ones.

Edge-based level-set segmentation methods consist in letting ϕ evolve in a specific manner and to locally stop the propagation once the zero level-set arrives to an interface. As a consequence, these methods strongly rely on the

ability to define the desired boundaries of the image, task usually achieved manipulating the gradient of the image itself. The level-set approach, on the other hand, guarantees boundary consistency and smoothness during the evolution process evolution.

Malladi-Sethian model. One of the most comprehensive formulations of an edge-based technique is the Malladi-Sethian level-set method, firstly introduced by Malladi and Sethian [56] and treated also by Caselles *et al.* [60]. It comprises one instance per each of three basic evolution fields presented in the previous paragraph. One possible formulation of its level-set evolution equation for a function $\phi(x, y, t)$, comprising of adequate initial and boundary conditions, is the following:

$$\begin{cases} \phi_t = g(\epsilon\kappa - \rho)|\nabla\phi| + \nu\nabla g \cdot \nabla\phi, & \text{in } \Omega \times (0, \infty) \\ \phi(x, y, 0) = \phi_0, & \text{in } \Omega \\ \phi(x, y, t) = min(\phi_0), & \text{in } \partial\Omega \times (0, \infty) \end{cases} \tag{4.11}$$

where ϵ, ρ and ν are parameters dosing the curvature-based, constant speed-based and advection-based motion fields, respectively, while g is the *edge-indicator function*. The edge-indicator function $g : \Omega \rightarrow \mathbb{R}$ can be defined as a function which reaches a constant, high value in homogeneous regions of the image, while it decreases in correspondence of strong variations in image contrast. The edge-indicator function adopted in the Malladi-Sethian model has been inherited from the pioneering work of Perona and Malik [61], and its analytical expression is

$$g = \frac{1}{1 + |\nabla(G_\sigma * I)|} \tag{4.12}$$

where $I : \Omega \rightarrow \mathbb{R}$ is the input image and G_σ is a Gaussian kernel: the convolution between G_σ and I produces a smoothed version of the image, while the final gradient operator achieves the true edge detection operation. Overall, the function g is equal to 1 in homogeneous areas and decreases in presence of contrast variations. Another expression for g, similar to (4.12) is

$$g = \frac{1}{1 + |\nabla I|/\beta} \tag{4.13}$$

in which β is a parameter controlling edge enhancement. Placing the definition of g given in (4.12) in the model equation in (4.11) allows to explain how the Malladi-Sethian segmentation method works. The first term on the right hand side determines an expansion motion, due to the presence of the positive constant-speed term ρ, also called *balloon term* [62]; the coupled curvature-based motion, controlled by ϵ, keeps a certain amount of boundary smoothness. Thanks to the presence of g as a factor, this first term is allowed to act on the local evolution of the contour only in absence of edges. The second term on the

right hand side consists in an advection term, dosed by the parameter ν, which attracts the contour to the image edges when near them, while it cancels out in homogeneous regions. An example of the application of the Malladi-Sethian segmentation technique is shown in Fig. 4.6.

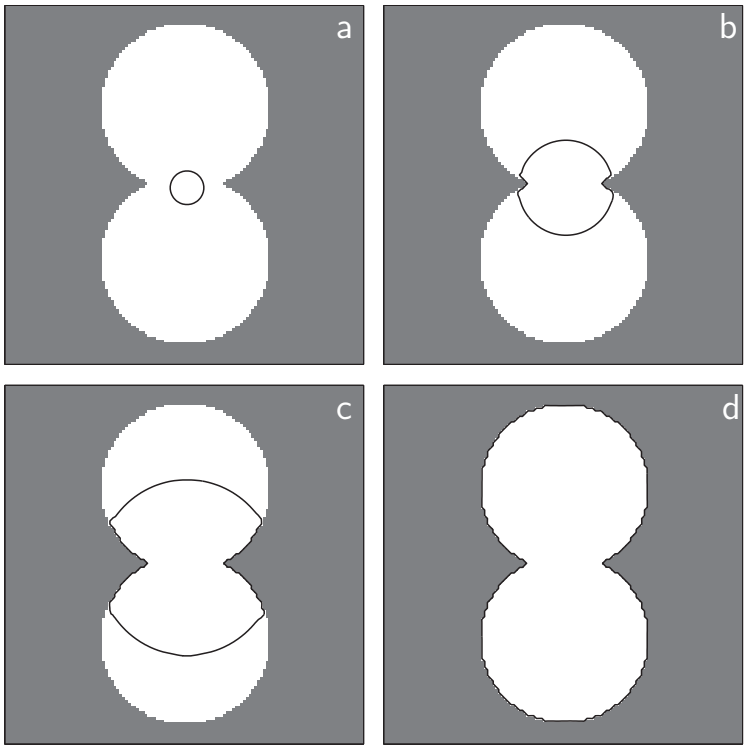

Figure 4.6: Example of the Malladi-Sethian segmentation technique.

4.4 Region-Based Level-Set Methods

Region-based level-set segmentation methods consist in letting ϕ evolve in order to separate the image into maximally homogeneous regions with respect to a certain criterion. This approach to image segmentation has been firstly proposed by Zhu *et al.* [63], while its consolidation in the level-set framework is due to the work by Chan and Vese [64].

Region-based methods are inherently variational methods: the evolution of the level-set function is aimed at the minimization of an energy functional E, designed following a specific criterion[1]. Formally, the aim is to find the level-set

[1]Of note, it is also formally possible to define an energy functional for most of the edge-based methods [60]. However, it is impractical to define a specific functional for the presented Malladi-Sethian model, also due to the presence of the parameters controlling the evolution terms.

function $\widetilde{\phi}$ which minimizes $E = E(\phi)$:

$$\widetilde{\phi} = \underset{\phi}{\operatorname{argmin}}\ E(\phi) \tag{4.14}$$

The Euler-Lagrange equation related to equation (4.14) is

$$\frac{\partial E}{\partial \phi} = 0 \tag{4.15}$$

in which $\partial E/\partial \phi$ represents the *first variation* of the energy functional with respect to ϕ. The first variation can be defined as

$$\frac{\partial E}{\partial \phi} = \lim_{l \to 0} \frac{E(\phi + l\psi) - E(\phi)}{l} \tag{4.16}$$

being ψ a test function of the same space of ϕ. In order to achieve the necessary energy functional minimization through the evolution of ϕ, it can be adopted a gradient descent approach:

$$\phi_t = -\frac{\partial E}{\partial \phi} \tag{4.17}$$

Equation (4.17) is another version of the level-set evolution equation (4.7), in which

$$V_n = \frac{1}{|\nabla \phi|} \frac{\partial E}{\partial \phi} \tag{4.18}$$

The most general formulation for the energy functional is the following one:

$$\begin{aligned} E(\phi) = \lambda_i \int_{\Omega_i} F_i(\phi, x, y) dxdy + \lambda_o \int_{\Omega_o} F_o(\phi, x, y) dxdy + \\ + \lambda_c \int_{\Gamma} F_c(\phi, x, y) dxdy \end{aligned} \tag{4.19}$$

in which the first two terms on the right hand side, called region terms, account for the values assumed by the energy functional respectively inside and outside the evolving contour, the last term, called contour term, carries an energy contribution relative to the contour itself and λ_i, λ_o and λ_c are weighting factors. Relatively to the ϕ, it is now useful to introduce two functions: the Heaviside function H and the Dirac delta function δ:

$$H(x, y) = \begin{cases} 1, & \text{in } \Omega_i \cup \Gamma \\ 0, & \text{in } \Omega_o \end{cases} \tag{4.20}$$

$$\delta(x, y) = |\nabla H(x, y)| \begin{cases} \neq 0, & \text{in } \Gamma \\ = 0, & \text{in } \Omega_i \cup \Omega_o \end{cases} \tag{4.21}$$

Of note, the Dirac delta function is formally a distribution whose integral over the domain Ω is equal to 1 only on the curve Γ. Embedding (4.20) and (4.21) into (4.19), the energy functional becomes

$$\begin{aligned} E(\phi) = \lambda_i \int_\Omega F_i(\phi, x, y) H(x, y) dxdy + \\ + \lambda_o \int_\Omega F_o(\phi, x, y) \big[1 - H(x, y)\big] dxdy + \\ + \lambda_c \int_\Omega F_c(\phi, x, y) \delta(x, y) dxdy \end{aligned} \tag{4.22}$$

this is the most commonly used formulation of the energy functional adopted in region-based level-set methods. The choice of a specific energy functional determines different segmentation results.

Chan-Vese model. One of the most important region-based technique is the Chan-Vese level-set method [64]. The proposed energy functional is

$$\begin{aligned} E(\phi) = \lambda_i \int_\Omega |I - c_i|^2 H dxdy + \\ + \lambda_o \int_\Omega |I - c_o|^2 (1 - H) dxdy + \\ + \mu \int_\Omega \delta dxdy + \nu \int_\Omega H dxdy \end{aligned} \tag{4.23}$$

where I is the input image and c_i and c_o are the mean intensities measured in Ω_i and Ω_o, respectively, during the evolution. The last two terms are regularization terms depending on the length of the curve and on the area of the region inside the curve itself. This regularization process on shape and size of the contour is needed to obtain a well-posed and well-conditioned problem. The associated level-set evolution equation (4.17), together with appropriate initial and boundary conditions, is the following:

$$\begin{cases} \phi_t = \dfrac{\delta}{|\nabla \phi|} \big[\mu \kappa - \nu - \lambda_i (I - c_i)^2 + \lambda_o (I - c_o)^2\big], & \text{in } \Omega \times (0, \infty) \\ \phi(x, y, 0) = \phi_0, & \text{in } \Omega \\ \dfrac{\delta}{|\nabla \phi|^2} \dfrac{\partial \phi}{\partial \mathbf{n}} = 0, & \text{in } \partial\Omega \times (0, \infty) \end{cases} \tag{4.24}$$

An example of the application of the Chan-Vese segmentation technique is shown in Fig. 4.7.

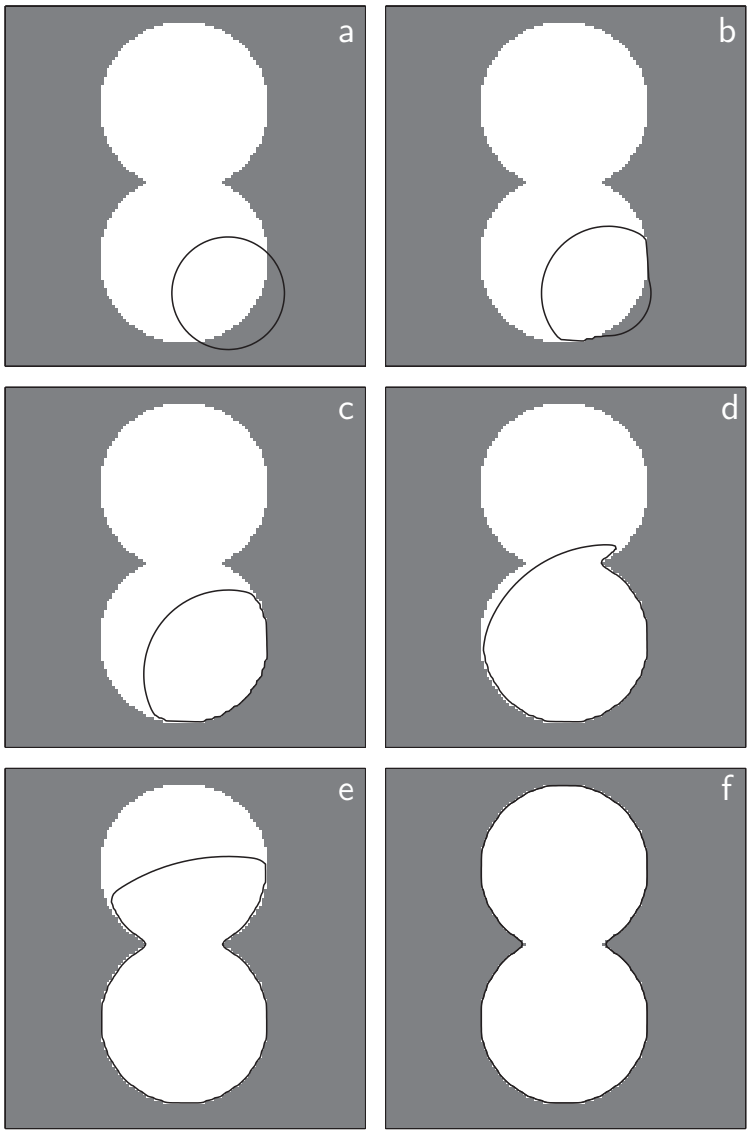

Figure 4.7: Example of the Chan-Vese segmentation technique.

4.5 Statistical Level-Set Methods

The extremely general formulation of the energy functional E given in (4.22) allows the embedding of *a priori* knowledge about the analyzed image and the target object. In this regard, one of the most important source of information is image statistics: the distribution of the gray levels in an image is usually related to the intrinsic noise introduced by the specific acquisition technique. This is particularly useful in biomedical image processing, since noise characteristics are well known for most of the clinically adopted acquisition systems.

Statistical level-set methods are essentially region-based methods which incorporate information about the statistical distribution of pixel intensity. Of note, differently from the other presented approaches, statistical methods are specifically formulated for digital images, since they are based on pixel intensity distribution.

Maximum Likelihood model. The Maximum Likelihood region-based statistical technique has been proposed by Sarti *et al.* [65]. The main idea behind this technique is to maximize the posterior probability relative to the gray levels distribution given the position of the evolving contour:

$$P(I|\phi) = P_i(I|\phi) \cdot P_o(I|\phi) \tag{4.25}$$

where P_i and P_o are relative respectively to the regions Ω_i and Ω_o, assumed to be statistically independent and uncorrelated. Assuming that pixels located within each region are also independent and uncorrelated, it follows that

$$P_i(I|\phi) = \prod_{(x,y)\in\Omega_i} p_i(I) \qquad P_o(I|\phi) = \prod_{(x,y)\in\Omega_o} p_o(I) \tag{4.26}$$

in which p_i and p_o are the probability density function associated to the pixel intensity I inside and outside the evolving contour, respectively. If the contour is not dividing the image into homogeneous regions, at least one between p_i and p_o will be characterized by a low profile, necessary to embrace a large variety of possible gray levels. On the other hand, the more homogeneous the two regions, the higher the measured $P(I|\phi)$. In order to avoid the complexity related to product operations, the functional to be maximized is the logarithm of $P(I|\phi)$ instead of $P(I|\phi)$ directly: since the logarithm function is monotonically increasing, the two functionals have the same optimal ϕ. As a consequence, the products in (4.26) become sums:

$$log\ P = log\ P_i + log\ P_o = \sum_{(x,y)\in\Omega_i} p_i(I)\ + \sum_{(x,y)\in\Omega_o} p_o(I) \tag{4.27}$$

Finally, moving from the discrete to the continuous domain, it is possible

to formulate the final version of the energy functional to be minimized:

$$\begin{aligned} E(\phi) = \lambda \int_{\Omega} \delta dxdy + \\ - \int_{\Omega} \big[log\ p(I)\big] H dxdy + \\ - \int_{\Omega} \big[log\ p(I)\big](1-H)dxdy \end{aligned} \tag{4.28}$$

where the first term is a regularization term. To move forward it is necessary to embed the known statistical distribution of image pixel. In the work by Sarti *et al.*, the focus was on echographic images, which are known to follow a Rayleigh distribution [65]:

$$p(I)_{rayleigh} = \frac{I}{\sigma^2} exp\bigg(- \frac{I^2}{2\sigma^2} \bigg) \tag{4.29}$$

After substituting (4.29) into (4.28), it is possible to compute the level-set evolution equation (4.17) for the Maximum Likelihood segmentation technique:

$$\begin{cases} \phi_t = \dfrac{\delta}{|\nabla\phi|}\bigg[\lambda\kappa + log\bigg(\dfrac{C_i A_o}{A_i C_o}\bigg) + f_i - f_o\bigg], & \text{in } \Omega \times (0,\infty) \\ \phi(x,y,0) = \phi_0, & \text{in } \Omega \\ \dfrac{\delta}{|\nabla\phi|^2}\dfrac{\partial\phi}{\partial\mathbf{n}} = 0, & \text{in } \partial\Omega \times (0,\infty) \end{cases} \tag{4.30}$$

in which the several appearing terms are defined as follows:

$$A_i = \int_{\Omega} H dxdy \qquad A_o = \int_{\Omega} (1-H) dxdy \tag{4.31}$$

$$C_i = \int_{\Omega} I^2 H dxdy \qquad C_o = \int_{\Omega} I^2 (1-H) dxdy \tag{4.32}$$

$$f_i = \frac{A_i I^2 - C_i}{C_i} \qquad f_o = \frac{A_o I^2 - C_o}{C_o} \tag{4.33}$$

An example of the application of the Maximum Likelihood segmentation technique is shown in Fig. 4.8.

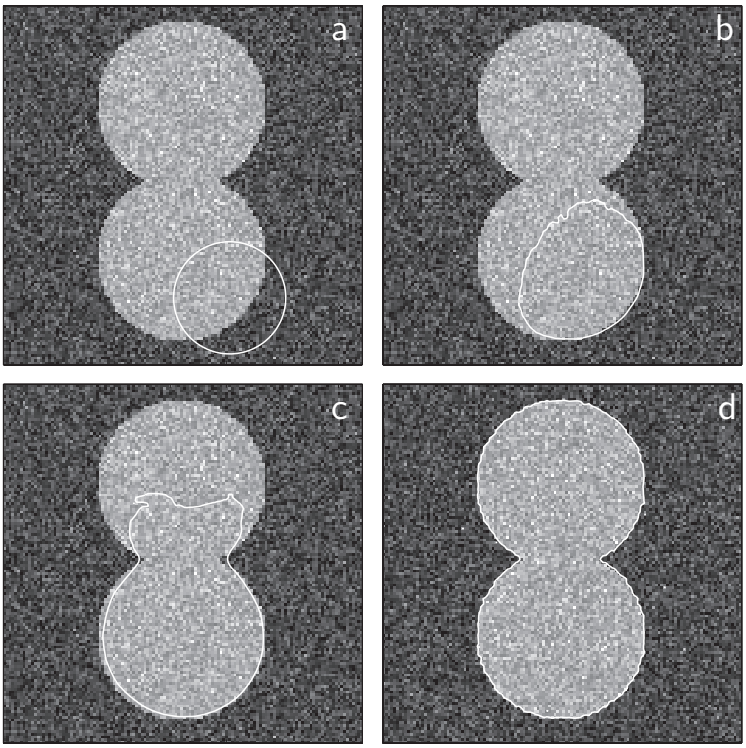

Figure 4.8: Example of the Maximum Likelihood segmentation technique with Rayleigh distribution.

Chapter 5

Myocardial Segmentation and Registration

As stated in the previous Chapters, the automated quantification of myocardial perfusion in FP-CMR images remains an open issue, since only a very limited number of techniques has been presented and none of them has yet gained the widespread consensus required for its adoption in the clinical arena. As a consequence, the need for fast and reliable techniques for perfusion evaluation remains strong.

In this Chapter, a novel approach for automated myocardial segmentation and non-rigid registration will be presented. Myocardial segmentation is performed using both edge-based and statistical region-based methods, which have been presented in Chapter 4. Non-rigid registration is achieved using an original modification of the well-known normalized cross-correlation algorithm. Steps of boundary regularization and refinement have also been implemented in the proposed approach in order to achieve smooth and consistent results.

5.1 Rationale

The design criteria adopted in the formulation of the present technique are the following ones:

I. Automaticity: maximum reduction of user interaction;

II. Effectiveness: applicability to a clinically realistic patient cohort;

III. Velocity: minimal computational cost;

IV. Robustness: independency from specific imaging protocols and systems.

Most of the methods proposed in literature first perform an overall image registration process, and then segment the myocardium. The problem with

this approach is that it usually requires the manual definition of the region in which the myocardium will be located throughout the sequence. Moreover, segmentation information can be helpful in achieving a reliable registration step. Accordingly, we decided to perform the segmentation as first step. Recently, statistical region-based methods have been deployed for the automated segmentation of the endocardium in CMR images (with no contrast enhancement). Corsi *et al.* [66] used the Maximum Likelihood method presented in § 4.5 with a Gaussian distribution, which is typical of magnetic resonance images. We hypothesized that the same method would be useful as well for endocardial detection in FP-CMR.

In the proposed approach, the frame used for myocardial segmentation is selected semi-automatically thanks to a specific algorithm. To provide the highest achievable accuracy in myocardial boundaries identification, we implemented different level-set techniques for endocardial and epicardial detection. Of note, the endocardial segmentation is performed first, and the resulting contour is used as initial condition for epicardial segmentation. After myocardial segmentation has been achieved for one frame of the sequence, a non-rigid registration algorithm alters position, size and shape of the computed boundaries in all the remaining frames in order to account for *out of plane* motion. This process is performed by means of an original multi-scale extension of the normalized cross-correlation algorithm coupled with level-set methods. The final result consists in myocardial boundaries registered in each frame of the sequence. In summary, the proposed technique is based on three major steps, which are listed in Fig. 5.1. Each one of these steps will be described in the following paragraphs.

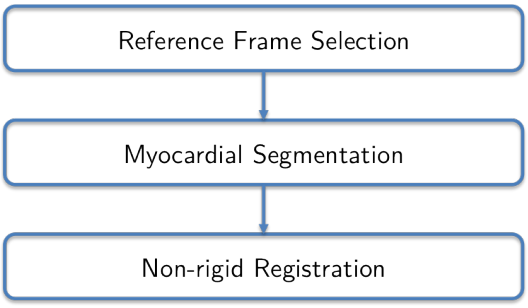

Figure 5.1: Main steps of the proposed technique.

5.2 Selection of the Reference Frame

To better describe the steps of the technique, it is useful to model a perfusion image sequence as a mapping $I : \Omega \times [1 \dots n] \rightarrow \Lambda$, where $\Omega \subset \mathbb{N}^2$ is the discrete image domain, n is the number of acquired frames and $\Lambda \subset \mathbb{N}$ is the gray level range. The selection of the frame into which both endo- and epicardial boundaries will take place is performed in a semi-automated way, since the only manual input required is the placement of a seed point inside the LV cavity in a random frame. Then, a time-intensity curve of a small, circular (radius 2 pixels) fixed region around the seed point is computed, reflecting cavity enhancement. Although myocardial motion will change the position of this region with respect to the endocardial boundary, it is likely that the small fixed region will not fall out of the cavity, hence offering a rather reliable cavity enhancement curve. The reference frame $I_r = I(\cdot, r)$ is defined as the one in which this cavity enhancement curve reaches the 95% of its maximum value (see Fig. 5.2).

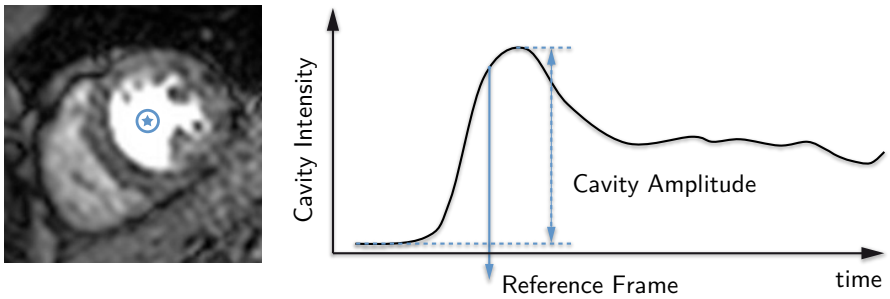

Figure 5.2: Selection of the reference frame.

This frame usually features optimal left and right ventricular cavities opacification as well as a certain level of myocardial enhancement, which are all helpful factors for myocardial segmentation (see Fig. 5.3).

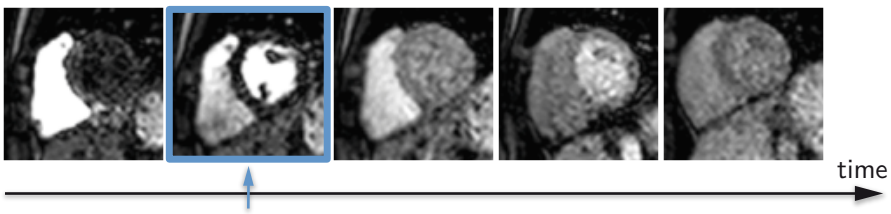

Figure 5.3: Selection of the reference frame in a sequence presented as example.

5.3 Myocardial Segmentation

Myocardial segmentation is performed in the defined reference frame I_r, and consists in two separate phases: endocardial and epicardial boundary detection. Level-set set techniques are adopted and specifically tailored for each of them. Fig. 5.4 shows the main steps in myocardial segmentation.

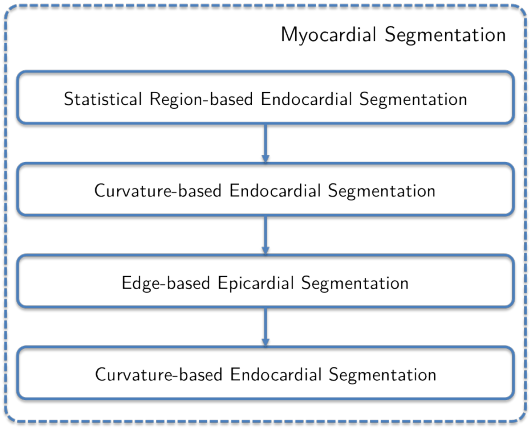

Figure 5.4: Main steps for myocardial segmentation.

Endocardial segmentation. Endocardial boundary detection is performed using the Maximum Likelihood algorithm presented in § 4.5, which is a statistical, region-based level-set method. Corsi *et al.* [66] adopted this algorithm for endocardial boundary detection in CMR images (i.e. with no contrast enhancement). This algorithm takes into account the noise distribution of MRI images (which, albeit being theoretically Rician, can be considered Gaussian for a reasonably high SNR [66]), and allows the segmentation of the image into maximally homogeneous regions. Firstly, following the formalism presented in Chapter 4, a level-set function $\phi_d : \Omega \times [0, \infty) \rightarrow \mathbb{R}$ is defined, and its zero level set $\Gamma_d = \phi_d^{-1}(0)$ represents the evolving contour. The Maximum Likelihood algorithm is based on the minimization of the functional (4.28):

$$\begin{aligned} E(I_r, \phi_d) = \lambda \int_\Omega \delta dxdy + \\ - \int_\Omega \big[log\ p(I_r)\big] H dxdy + \\ - \int_\Omega \big[log\ p(I_r)\big](1 - H) \end{aligned} \tag{5.1}$$

where H and δ are the Heaviside function and the Dirac delta function defined in (4.20) and (4.21) respectively and define the partition of Ω into the regions inside and outside Γ_d. The function $p(I_r)$ is the probability density

distribution associated to the pixel intensity in the reference image, and is said to be Gaussian:

$$p(I)_{gaussian} = \frac{1}{\sqrt{2\pi}\sigma} exp\left[-\frac{1}{2}\left(\frac{I-\mu}{\sigma}\right)^2 \right] \tag{5.2}$$

where μ and σ are the mean and variance of I_r, respectively. To obtain the evolution equation for this specific functional, it is necessary to embed (5.1) and (5.2) into (4.7). The result, comprising of adequate initial and boundary conditions, is the following one:

$$\begin{cases} \dfrac{\partial \phi_d}{\partial t} = \dfrac{\delta}{|\nabla \phi_d|}\left[\lambda\kappa + log\left(\dfrac{e_i}{e_o}\right) + f_i - f_o\right], & \text{in } \Omega \times (0,\infty) \\ \phi_d(x,y,0) = \phi_{d0}, & \text{in } \Omega \\ \dfrac{\delta}{|\nabla \phi_d|^2}\dfrac{\partial \phi_d}{\partial \mathbf{n}} = 0, & \text{in } \partial\Omega \times (0,\infty) \end{cases} \tag{5.3}$$

having defined

$$A_i = \int_\Omega H dxdy \qquad A_o = \int_\Omega (1-H) dxdy \tag{5.4}$$

$$B_i = \int_\Omega I_r H dxdy \qquad B_o = \int_\Omega I_r (1-H) dxdy \tag{5.5}$$

$$C_i = \int_\Omega I_r^2 H dxdy \qquad C_o = \int_\Omega I_r^2 (1-H) dxdy \tag{5.6}$$

$$f_{i,o} = \frac{A^2 I_r^2 - 2 I_r AB + 2B^2 - AC}{AC - B^2} \tag{5.7}$$

$$e_{i,o} = \frac{AC - B^2}{A^2} \tag{5.8}$$

The initial level-set function ϕ_{d0} (with Γ_{d0} being its zero level-set) is defined as the distance function from the seed point used for the selection of the reference frame. The exit condition of motion is reached once there is no noticeable change in the value of the functional E. Let $\widehat{\phi_d}$ be the final level-set function.

After this step, the endocardial contour undergoes a regularization motion, which is necessary to include the papillary muscles inside the contour itself. This regularization process is achieved using a modified curvature motion (see § 4.2) specifically designed not to allow curvature above a certain level:

$$\begin{cases} \dfrac{\partial \phi_d}{\partial t} = \xi\big[(\kappa < 0) + g(\kappa < \kappa_{avg})\big], & \text{in } \Omega \times (0,\infty) \\ \phi_d(x,y,0) = \widehat{\phi_d}, & \text{in } \Omega \\ \phi_d(x,y,t) = min\ \widehat{\phi_d}, & \text{in } \partial\Omega \times (0,\infty) \end{cases} \tag{5.9}$$

in which κ is the local curvature of ϕ_d, κ_{avg} is the average curvature of Γ_d obtained with the previous statistical level-set algorithm, ξ is a fixed negative

parameter (working as a balloon coefficient) and g is the Perona-Malik edge-indicator (4.13) applied to I_r. This equation allows to locally expand the only portions of Γ_d characterized by a curvature value either negative or lower than the average one (when not close to an edge). The exit condition is reached when the area of the region inside Γ_d becomes greater than $l \cdot Area_{Hull}$, where $Area_{Hull}$ is the area of the convex hull computed using the initial $\widehat{\Gamma_d}$ contour and l a fixed parameter. Let $\widetilde{\phi_d}$ be the final level-set function. Fig. 5.5 shows the main steps in endocardial segmentation.

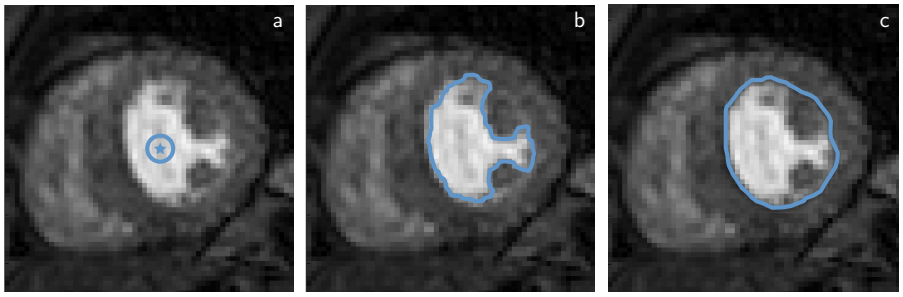

Figure 5.5: Example of endocardial segmentation: a) seed point and initial contour, b) result of the Maximum Likelihood algorithm, c) result of the regularization motion.

Epicardial segmentation. Epicardial boundary detection is performed using the Malladi-Sethian algorithm, presented in § 4.3, which is an edge-based level-set method. This algorithm is adopted to search the image from the endocardium outwards in order to identify the epicardial boundary. To this end, a new level-set function ϕ_p is defined, together with its zero level-set $\Gamma_p = \phi_p^{-1}(0)$. The level-set surface is then moved by means of the evolution equation (4.11):

$$\begin{cases} \dfrac{\partial \phi_p}{\partial t} = g(\epsilon\kappa - \rho)|\nabla\phi_p| + \nu\nabla g \cdot \nabla\phi_p, & \text{in } \Omega \times (0,\infty) \\ \phi_p(x,y,0) = \widetilde{\phi_{p0}} = \widetilde{\phi_d} - dist, & \text{in } \Omega \\ \phi_p(x,y,t) = min\ \phi_p, & \text{in } \partial\Omega \times (0,\infty) \end{cases} \tag{5.10}$$

The initial epicardial contour is defined as an expanded version of the computed endocardial contour by means of the parameter $dist$. The edge-indicator function g is defined as in (4.13). The exit condition is reached when the area of the region inside Γ_p does not change significantly. Let $\widehat{\phi_p}$ be the final level-set function.

The final step of epicardial border detection is again boundary regulariza-

tion, which is achieved using again the evolution equation (5.9):

$$\begin{cases} \dfrac{\partial \phi_p}{\partial t} = \xi\big[(\kappa < 0) + g(\kappa < \kappa_{avg})\big], & \text{in } \Omega \times (0, \infty) \\ \phi_p(x, y, 0) = \widehat{\phi_p}, & \text{in } \Omega \\ \phi_p(x, y, t) = min\ \widehat{\phi_p}, & \text{in } \partial\Omega \times (0, \infty) \end{cases} \tag{5.11}$$

Let $\widetilde{\phi_p}$ be the final level-set function.

At the end of myocardial segmentation, both endocardial and epicardial boundaries ($\widetilde{\Gamma_d}$ and $\widetilde{\Gamma_p}$, respectively) are available in the reference frame I_r. Fig. 5.6 shows the main steps in epicardial segmentation together with the final result of myocardial segmentation.

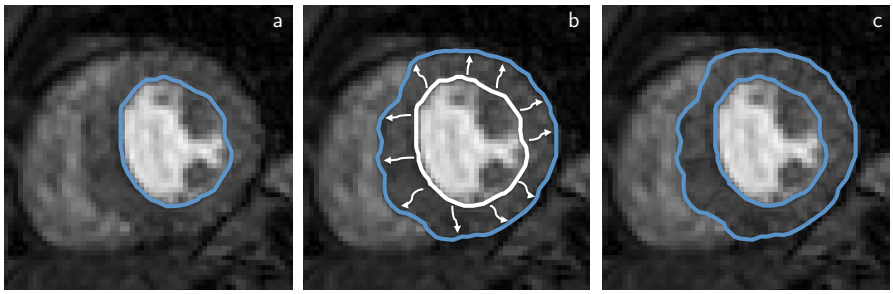

Figure 5.6: Example of epicardial segmentation: a) initial contour, b) result of the Malladi-Sethian algorithm and regularization motion, c) final result of myocardial segmentation.

5.4 Non-rigid Registration

To take into account the changes in position, size and shape of the myocardium throughout the sequence, which might have occurred in the frames both preceding and following I_r, a non-rigid registration technique is required. We implemented a multi-scale extension of the normalized cross-correlation algorithm followed by a contour adaptation step achieved using again the Malladi-Sethian level-set algorithm. Fig. 5.7 shows the main steps for non-rigid registration.

The first step consists in the definition of an Original Template T as a crop of the reference frame I_r around the computed outer myocardial boundary Γ_p. Then, a series of $h - 1$ other Templates are defined by resizing the Original Template by one pixel difference at a time uniformly (see Fig. 5.8).

The next step involves the computation of the normalized cross-correlation between the consecutive frame $I(\cdot, r + 1)$ and each Template (both Original and Resized ones). This operation results in h normalized cross-correlation

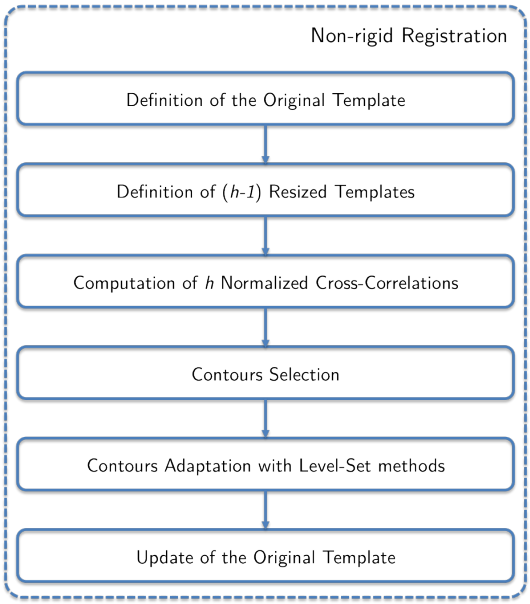

Figure 5.7: Main steps for non-rigid registration.

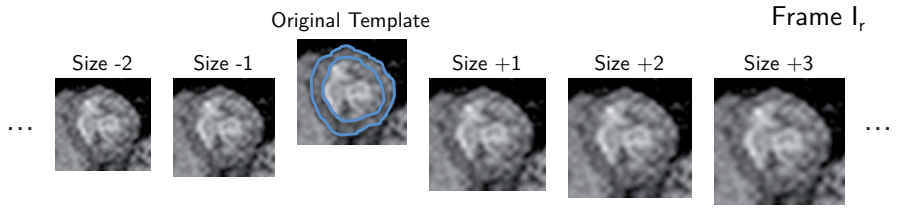

Figure 5.8: Definition of the Original Template and of the Resized Templates in the reference frame I_r.

matrixes M. The elements $m_k(u,v)$ of each matrix M_k are defined as follows[1]:

$$m_k(u,v) = \frac{\sum_{i,j}\left[I(i,j,r+1) - \widehat{I_{u,v}}\right]\left[T_k(i-u,j-v) - \widehat{T_k}\right]}{\sqrt{\sum_{i,j}\left[I(i,j,r+1) - \widehat{I_{u,v}}\right]^2 \sum_{i,j}\left[T_k(i-u,j-v) - \widehat{T_k}\right]^2}} \quad (5.12)$$

where $\widehat{T_k}$ is the mean pixel intensity of T_k and $\widehat{I_{u,v}}$ is the mean pixel intensity of the region of $I(\cdot, r+1)$. Then, per each matrix M_k, the highest value is selected and denoted as CC_k. The new position and scale of the myocardial contours are finally determined by selecting the highest cross-correlation peak CC_k between the h possible combinations. As final step, both endocardial and

[1]In this paragraph we will consider a discretized version of the domain Ω with indices i, j for both image frames and level-set surfaces. However, for ease of notation, we will not introduce any obvious formal definition.

epicardial curves undergo a Malladi-Sethian evolution, as described by (4.11), which allows a fine non-rigid tuning of the displaced contours (see Fig. 5.9). Figs. 5.10 and 5.11 show some results of the proposed non-rigid registration algorithm.

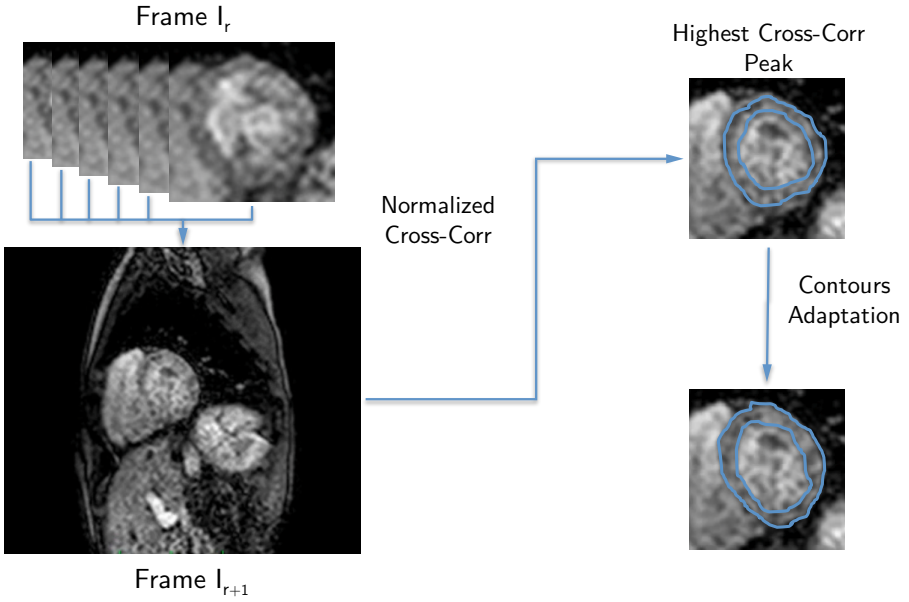

Figure 5.9: Computation of h normalized cross-correlation matrixes, contours selection and adaptation.

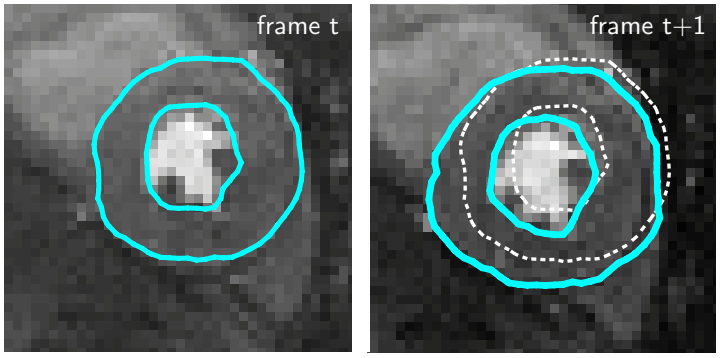

Figure 5.10: Non-rigid registration: on the left, myocardial boundaries in a sequence frame; on the right, the subsequent frame with the boundaries before (white, dotted) and after (cyan, solid) non-rigid registration.

The conclusion of the registration process is reached with the update of the Original Template, which is necessary to account for the changes in brightness of myocardial components due to contrast medium inflow. This is achieved

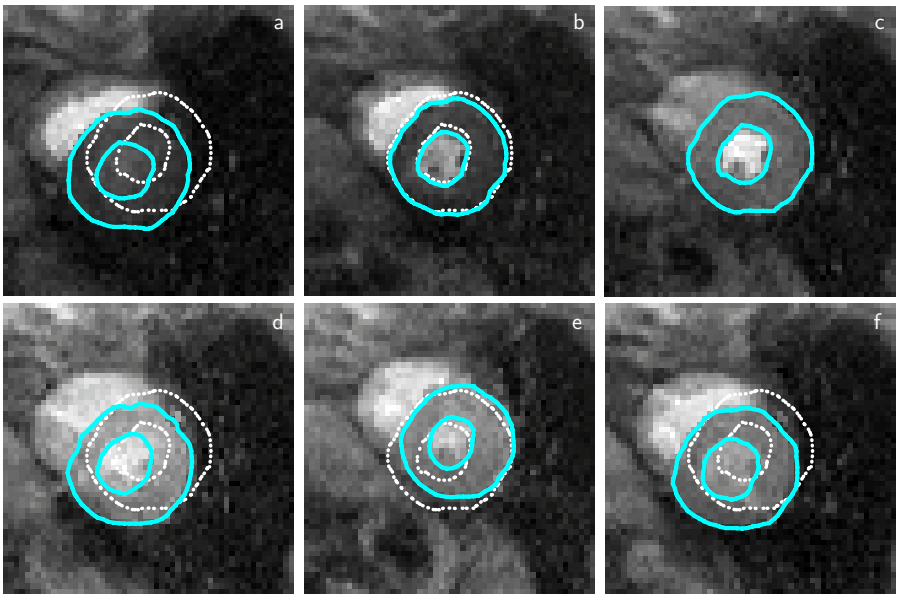

Figure 5.11: Example of the application of the registration algorithm in different frames (from a to f – c is the reference frame) of a perfusion sequence: in each panel, myocardial contours are displayed both before (white, dotted) and after (cyan, solid) non-rigid registration.

by averaging pixel-by-pixel the Original Template with the counterpart image crop in the new frame. To limit potential error propagation, the update process takes place only for sufficiently high values of the highest CC_k. Of note, in order not to lose the achieved accuracy in myocardial segmentation, the reference computed contours are not changed through the registration process. The overall algorithm for the registration of two consecutive frames is hereby listed:

Registration of frame $I(\cdot, r+1)$ from $I(\cdot, r)$:

1. Definition of the Original Template
   $T_0 = I(i \dots i+p, j \dots j+q; r)$
   and associated level-set contours
   $\widetilde{\phi_d}(i \dots i+p, j \dots j+q)$, $\widetilde{\phi_p}(i \dots i+p, j \dots j+q)$
2. Definition of $h-1$ Resized Templates
   $T_k = resize(T_0; p+k, q+k)$
   with $k = -l \cdots -1, 1, \dots m \in \mathbb{Z}$, $h = l+m+1$
   and associated resized contours $\widetilde{\phi_{d\_k}}$, $\widetilde{\phi_{p\_k}}$
3. Computation of h Normalized Cross-Correlation Matrixes
   $M_k = normxcorr\big(I(\cdot, r+1), T_k\big)$
   $CC_k = \max_{(u,v)} M_k$

4. Selection of the contours $\widetilde{\phi_{d\_\bar{k}}}$, $\widetilde{\phi_{p\_\bar{k}}}$
   with $\bar{k} = \underset{k}{\text{argmax}}\ CC_k$
5. Contours adaptation with Malladi-Sethian model
6. Original Template Update (if $CC_{\bar{k}} \geq thresh$)
   $T_{CC} = I(\bar{i} \dots \bar{i} + p + \bar{k}, \bar{j} \dots \bar{j} + q + \bar{k}; r + 1)$
   $T_0 = mean\big(T_0, resize(T_{CC}; p, q)\big)$

in which $\bar{i}$ and $\bar{j}$ indicate the position of $T_{\bar{k}}$ placed in correspondence of the cross-correlation peak. The method is applied to all the images, registering each frame with the preceding one, applying the above listed algorithm from step 2 to 6. Importantly, frames preceding the reference frame are registered in the opposite direction, from the reference frame towards the first one.

5.5 Comparison with State of the Art

The presented technique is based on the combination of a reference frame selection algorithm, an automated segmentation method and a non-rigid registration scheme: in this paragraph these steps will be discussed and compared to the state of the art presented in $ 3.2, $ 3.3 and $ 3.4.

The selection of the reference frame is performed using an extremely simple algorithm. Albeit the overall technique is been considered automated in this work, it requires the placement of a seed point somewhere in the LV cavity in a random frame. However, the user interaction required for this operation is truly negligible.

The adopted segmentation methodology takes full advantage of the level-set framework to identify the myocardium. The algorithms have been specifically tailored for the specific aim of this technique. The statistical level-set approach is a powerful tool for LV cavity identification, since it is not haunted by the high noise levels typical of FP-CMR images (actually, it takes advantage of it) and it is able to deal with extremely complex shapes, which are often seen in CMR due to the presence of papillary muscles and of potential cardiomyopathies. The subsequent regularization approach, which is based only on the curvature, allows to include the papillary muscles without moving the other portion of the contour. While very powerful in segmenting objects of given gray level intensity distribution, regardless of their shape, statistical level set methods tend to fail in detecting epicardial boundaries: this is mainly due to the fact that the intensity distribution of the myocardium can be very similar to the one of the surrounding tissue. As a consequence, we implemented an edge-based level set methods to perform epicardial detection. Edge-based methods can be tuned to keep a more regular shape (starting from the computed endocardial one) and be sensitive to the presence of weak edges. As a whole, the proposed

segmentation technique does not rely on error-prone intensity-based methods such as thresholding and morphologic operators (cfr. Weng *et al.* [46]), it can manage strong convexities and concavities (cfr. Santarelli *et al.* [47]) and does not require the definition of shape priors (cfr. Gupta *et al.* [25]), which could fail in detecting abnormally shaped myocardial regions. To the best of our knowledge, at the beginning of the Ph.D. program there was no published evidence, either on journal papers or on conference proceedings, that a statistical level-set method could have been adopted for endocardial segmentation in FP-CMR images. During the writing of the present Thesis, we discovered that the same approach had been independently implemented by Li *et al.* [48] [23]. This reinforces our belief about the choice of this method. Despite being based on the same statistical level-set approach for endocardial segmentation, however, the two techniques differ in epicardial segmentation and boundary regularization methods.

The non-rigid registration scheme combines a multiscale version of the normalized cross-correlation algorithm with contours boundaries adaptation by means of level-set methods. This choice was based on the major advantages of cross-correlation, that make it particularly well-suited to deal with the presented issues: mainly, it is capable of dealing with changes in brightness (if happening homogeneously in the object to be identified) and it can be executed at a high computational speed. However, it was necessary to embed two additional features: multiscale non-rigid registration capabilities, and insensitivity to non-homogeneous changes in brightness. These extra capabilities were achieved embedding level-set methods, using an array of resized templates and updating them through time by means of an averaging-based scheme. When compared to other non-rigid methods, the proposed registration algorithm is computationally fast (cfr. Olafsdottir *et al.* [52]), does not rely on any hypothesis about the possible trajectory of the myocardium in time (cfr. Wollny *et al.* [22]) and it is capable of dealing directly with considerable deformations during its one and only application (cfr. Li *et al.* [23]). It is of prime importance to point out here that most of the works presented in literature featuring non-rigid schemes perform registration by deforming and interpolating the acquired frames in order to force the myocardial boundaries in the same position throughout the whole sequence. This approach is very risky given the nature of the present problem since the final goal is to detect perfusion defects (i.e. small dark regions), which could be altered and potentially underestimated if processed through strong, non uniform image interpolation. Accordingly, the proposed algorithm acts on the contours computed by segmentation, and leaves the original frames untouched.

Chapter 6

Image Generation & Analysis

In order evaluate the robustness of the implemented technique and test its suitability for a potential clinical adoption, an extensive validation procedure was designed. Three different image datasets were generated and analyzed. The first one is a synthetic dataset, miming an FP-CMR image sequence, while the other two are both real datasets, acquired in proper hospitals. To ensure independency from the specific protocol details used for image acquisition, the two real datasets were acquired in different facilities and using different scanners.

In this Chapter, the protocols for the image datasets generation, synthetic and real ones, will be described. Moreover, a final paragraph will provide details about the choice of the main parameters comprised in the adopted technique.

6.1 Synthetic Dataset

The synthetic dataset was generated in MATLAB®(MathWorks, Natick, Massachussetts, US) using code specifically designed for this purpose. Two circles are created, featuring same center but different radii, representing the endocardium and the epicardium. Each of the two circles has a uniform pixel intensity value. Starting from the initial one, 99 other synthetic frames are created by moving, resizing and changing the pixel intensity value of the two circles, independently. Motion is performed by rigid translation driven by a uniformly distributed random, integer variable. Resizing acts using a bilinear interpolation method and, similarly to motion, is driven by a random integer variable; more specifically, the circles undergo a resize process of (r_1, r_2) pixels in the (x, y) direction, where r_1 and r_2 are independent random variables taking integer values between -1 and 3. These values have been heuristically chosen looking at the average myocardial deformation seen in real images. The pixel intensity value of the circles also changes following uniformly distributed random real variables, one per each circle, in order to mime enhancement changes

in the myocardium and in the cavity. Of note, this condition (random distribution) creates a sequence harder to be registered when compared to a real one, characterized by a coherent contrast inflow. Assumed values are in the range 0.2 - 0.8. Finally, for each frame, random Gaussian noise is added (mean 0.1, standard deviation 0.1) in order to simulate CMR image noise. The resulting synthetic images are reported in Fig. 6.1.

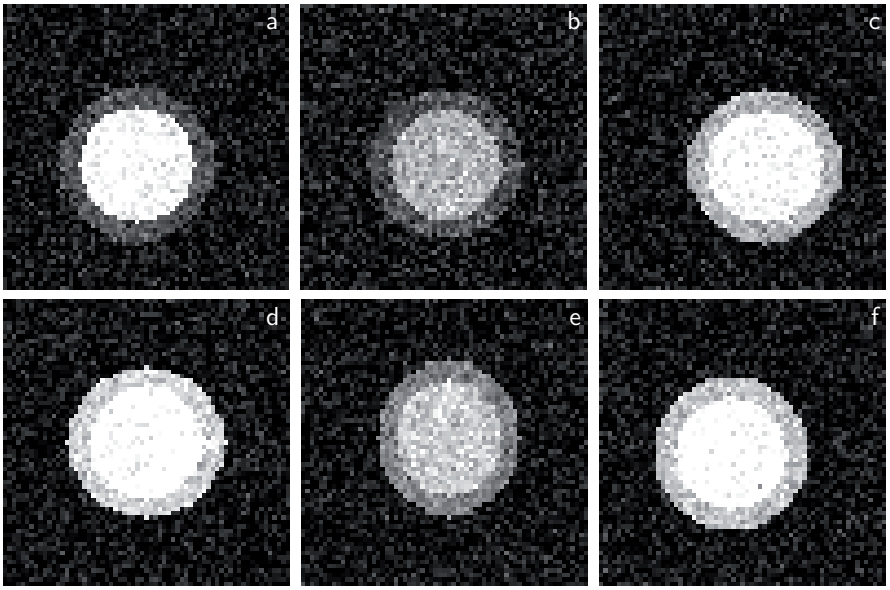

Figure 6.1: Synthetic sequence frames, showing the generated changes in position, size, shape, pixel intensity and noise levels of the different image components.

6.2 Real Datasets

Two real dataset were acquired. They will be denoted as Dataset A and Dataset B. Overall, the study included 42 patients who underwent contrast-enhanced CMR imaging. Exclusion criteria were: standard contraindications to CMR imaging with Gadolinium-based contrast mediums (specifically Gadolinium-DTPA), and contraindications to vasodilator agents. Patients were asked to avoid beta-blockers, nitrates and caffeine before their stress CMR study. The Institutional Review Board approved the study protocol, and all patients provided informed consent.

Population. Dataset A was acquired at the University of Chicago and included 15 adult subjects (age 56 ± 15 yrs, 9 males) in whom CAD was ruled out by the absence of visually apparent perfusion abnormalities or late Gadolin-

ium enhancement. Dataset B was acquired at the University of Virginia and included 27 patients (age 64 ± 13 yrs, 20 males). These patients were referred for coronary angiography on the basis of abnormal SPECT. In these patients, coronary angiography was performed within 30 days following CMR. Patients were excluded if they had a recent myocardial infarction, or were older than 85. Of the 27 patients, 9 patients had history of myocardial infarction, 7 had undergone previous revascularization, 22 had hypertension, 24 had dyslipidemia, and 7 patients had diabetes mellitus.

Protocols. For Dataset A, stress perfusion imaging was performed starting 1 minute after intravenous injection of a 0.4 mg bolus of A2A-specific vasodilator stress agent regadenoson (Lexiscan®, Astellas Pharma, Deerfield, Illinois, US). Then, perfusion imaging was repeated 15 minutes after injection of aminophylline under resting conditions. For Dataset B, adenosine (Adenoscan®, Astellas Pharma) was intravenously infused at a rate of 140 μg/kg/min, and stress imaging was performed starting 2 to 3 min after the initiation of infusion. Resting images were obtained 10 minutes after stopping adenosine infusion.

FP-CMR imaging. In each patient, short-axis images were acquired one image per cardiac cycle at three levels of the left ventricle (base, mid, apex; see Fig. 6.2). Patients were instructed to hold their breath as long as possible, starting just prior to the administration of contrast.

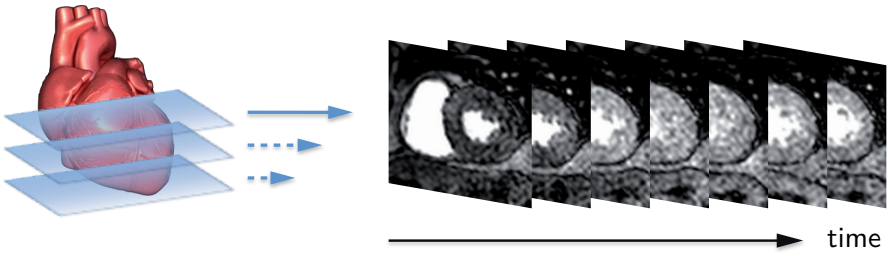

Figure 6.2: Scheme showing the three acquisition planes at basal, mid and apical level. From each of them one sequence is acquired.

For Dataset A, we used a 1.5T scanner (Philips, Best, Netherlands) with a phased-array cardiac coil. Images were acquired during 80-90 cardiac cycles using a hybrid gradient-echo and echo-planar imaging sequence (GRE-EPI), nonselective 90° saturation pulse followed by a 80 ms delay, voxel size ~2.5 x 2.5 mm, acquisition time 83 ms per slice, slice thickness 10 mm, flip angle 20°, repetition time 5.9 ms, echo time 2.7 ms, EPI factor 5, and SENSE factor 2. Imaging was performed during first pass of a Gd-DTPA bolus (0.075 - 0.10 mmol/kg at 4 - 5 ml/sec), followed by 20 ml saline (4 ml/s).

For Dataset B, studies were performed on a 1.5T scanner (Siemens Healthcare, Erlangen, Germany) with a 4-channel phased-array radiofrequency coil. Imaging was performed during 40-50 cardiac cycles using the GRE-EPI sequence [17]: nonselective 90° saturation pulse followed by an 80 ms delay, field of view 340 to 400×212 to 360 mm, matrix = 128×80, slice thickness 8 mm, flip angle 25°, repetition time 5.6-6.2 ms, echo time 1.3 ms, echo train length 4, effective spatial resolution ∼2.8×2.8 mm with (n = 23) or without (n = 18) rate 2 parallel imaging (TSENSE) [67]. Imaging was performed twice during first pass of two Gd-DTPA boluses: first using a low dose of contrast (0.0075 mmol/kg at 4 ml/sec) to measure contrast enhancement in the LV cavity, and then a standard dose (0.075 at 4 ml/sec) to measure intramyocardial contrast. Each bolus was followed by 20 ml normal saline (4 ml/s). The double bolus injection was due to the application of the dual bolus technique, necessary for the correct estimation of the contrast inflow in the LV cavity [17].

6.3 Automated Analysis Details

The proposed technique was implemented in MATLAB®(MathWorks, Natick, Massachussetts, US) using custom designed code.

Both real datasets were analyzed by the implemented technique. Important parameters for the segmentation (see § 5.3) are the following ones: $dt_{endo} = 0.1$ (discrete time step for the implementation of the statistical endocardial segmentation algorithm); $\lambda = -0.5$ (regularization parameter for statistical endocardial segmentation, see equation (5.1)); $dt_{epi} = 0.04$ (discrete time step for the implementation of the statistical endocardial segmentation algorithm); $\epsilon = 5$, $\rho = 1$, $\nu = 6$, $dist = 2$ (parameters for the edge-based epicardial segmentation algorithm); $\xi = -2$, $l = 1.05$ (parameters for both the endo- and epicardial regularization motions). Registration is completely automated, but relies on some fixed parameters (see § 5.4): $h = 6$ (the total number of Templates, with resize pixel steps ranging from -2 to +3); $thresh_{forward} = 0.95$ (threshold for the update of the Original Template during the registration of frames subsequent to the reference one); $thresh_{backward} = 0.65$ (threshold for the update of the Original Template during the registration of frames precedent to the reference one); $window = \pm 8$ px (maximum pixel displacement allowed to the contours with respect to their position in the reference frame). Albeit many, not all these parameters are critical for the correct functioning of the technique. This is demonstrated by the fact that, between the two different datasets A and B, only the parameter dt_{endo} had to be adjusted (from 0.1 to 0.02) due to the difference in the resolution of the acquired images. However, it is important to point out that for patients with particularly thick myocardial walls, it was seldom necessary to act on the parameter $dist$.

The synthetic dataset was used to assess the accuracy of the registration algorithm alone. As a consequence, the reference frame selection and myocardial segmentation steps were not performed: the contours used for the registration process are the true ones taken from the first frame. The parameters reported for the registration of the real sequences still hold for the synthetic dataset.

Chapter 7

Geometrical Validation

When validating a procedure for object identification, it is common practice to compare the obtained contours with reference ones. In literature, several error metrics have been proposed to perform this comparison. These indices usually give an insight about the mutual distance and the difference in image coverage of the two sets of contours, and thus are of help in the evaluation of the accuracy achievable with a specific technique.

In this Chapter, the comparison between automatically extracted contours and reference ones will be illustrated. More in detail, contours computed with the proposed technique will be compared to true ones in the synthetic dataset, and to manually traced ones in Dataset A. At first the adopted error metrics will be described, then the results of the comparisons will be displayed and discussed.

7.1 Performance Metrics

Among the many error metrics which can be adopted to compare contours, the ones used in the present study are the Hausdorff Distance [68], the Mean Absolute Distance [69], the Root Mean Square Distance [70], and the Dice Coefficient [71]. The first three indices are distance-based, while the last one is an area-based metric. Let us define two sets of points $\Gamma_e = \{e_1, e_2, \dots e_p\}$ and $\Gamma_r = \{r_1, r_2, \dots r_p\}$. The metrics are defined as following:

I. Hausdorff Distance (HD):

$$HD(\Gamma_e, \Gamma_r) = \max\left\{ \max_i d(e_i, \Gamma_r), \max_j d(r_j, \Gamma_e) \right\} \tag{7.1}$$

where $d(e_i, \Gamma_r) = \min_{r_j \in \Gamma_r} |r_j - e_i|$, i.e. the minimum Euclidean distance from a given point to the other set. The Hausdorff Distance measures the maximum distance between the two sets of points;

II. Mean Absolute Distance (MAD):

$$MAD(\Gamma_e, \Gamma_r) = \frac{1}{2}\left[\frac{1}{p}\sum_{i=1}^{p} d(e_i, \Gamma_r) + \frac{1}{q}\sum_{j=1}^{q} d(r_j, \Gamma_e)\right] \tag{7.2}$$

Differently from the Hausdorff Distance, the Mean Absolute Distance (MAD) measures the mean distance between the two sets of points;

III. Root Mean Square Distance (RMSD):

$$RMS(\Gamma_e, \Gamma_r) = \frac{1}{2}\left\{\sqrt{\frac{1}{p}\sum_{i=1}^{p}\left[d(e_i, \Gamma_r)\right]^2} + \sqrt{\frac{1}{q}\sum_{j=1}^{q}\left[d(r_j, \Gamma_e)\right]^2}\right\} \tag{7.3}$$

The Root Mean Square Distance returns information similarly to MAD;

IV. Dice Coefficient (DC):

$$DC(\Omega_e, \Omega_r) = \frac{2Area(\Omega_e \cap \Omega_r)}{Area(\Omega_e) + Area(\Omega_r)} \tag{7.4}$$

having defined as Ω_e and Ω_r the convex regions inside Γ_e and Γ_r, respectively. The Dice Coefficient (DC) measures the overlapping between the regions included in the sets of points.

Of note, the unit of all the distance-based metrics (HD, MAD and RMSD) is pixels, while the area-based one (DC) is dimensionless. The combined use of these metrics allows to evaluate the local and global differences between the compared contours.

7.2 Contours Accuracy in the Synthetic Dataset

The synthetic dataset[1] was used to assess the accuracy of the automated non-rigid registration algorithm, given the correct contours in the first frame. Some results are displayed in Fig. 7.1.

The error metrics defined in the last paragraph were applied to all the 100 images. Tab. 7.1 shows the obtained results.

Notably, the HD shows that, on average, the maximum distance between registered and reference contours is only slightly bigger than 1 px. The mean MAD is always lower than 0.5 px, instead.

[1] For details about the image generation process please refer to § 6.1.

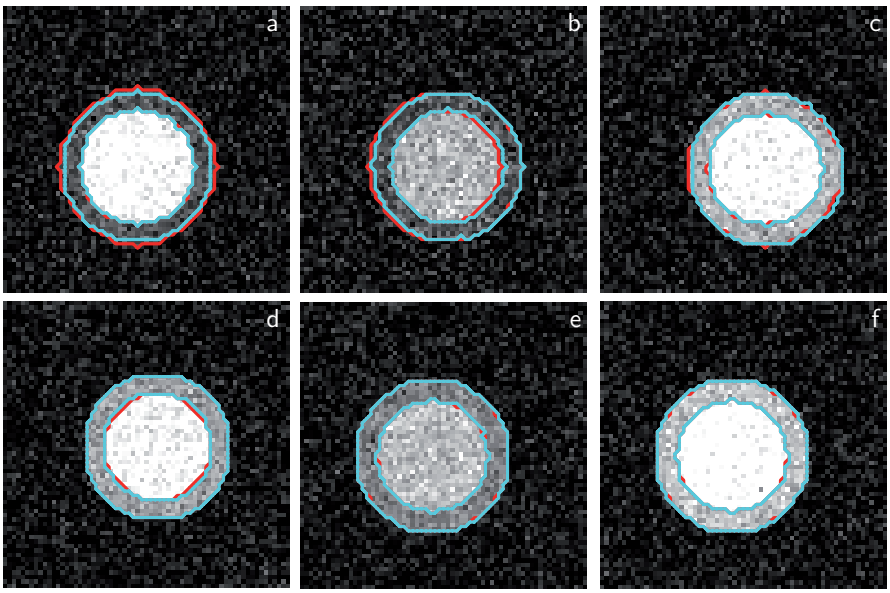

Figure 7.1: Synthetic sequence frames showing the comparison between automatically registered contours (light blue) and true ones (red).

	HD	MAD	RMSD	DC
Endo	0.95 ± 0.35	0.24 ± 0.17	0.39 ± 0.19	0.98 ± 0.01
Epi	1.40 ± 0.59	0.38 ± 0.20	0.55 ± 0.23	0.98 ± 0.01
Overall	1.18 ± 0.53	0.31 ± 0.20	0.47 ± 0.22	0.98 ± 0.01

Table 7.1: Error metrics (mean $\pm$ standard deviation) for the comparison between automatically registered contours and true ones in the synthetic dataset.

7.3 Contours Accuracy in Dataset A

The complete automated technique was tested on real perfusion sequences belonging to Dataset A. More specifically, 11 FP-CMR sequences (each one belonging to a different patient) acquired[2] at the mid-ventricular level during rest were analyzed. None of the parameters of the method were changed between different patients. After automated analysis, manual tracing was performed onto all image frames by an experienced reader, and the contours were compared between automated and manual analysis by means of the error metrics presented in § 7.1. Although the automated technique tries to register all the sequence frames, some initial frames were not traced by the operator due to absence of contrast enhancement: these frames were obviously excluded in the comparison. Overall, the frames used were 556.

[2]For details about the acquisition protocol and the population please refer to § 6.2.

Time required for automated analysis of a complete perfusion sequence was less than 1 minute on a personal computer, while manual tracing of the same sequence required at least 10 minutes. Of note, no code optimization or parallel computing were adopted in the present implementation, although they could further shorten analysis time. Some results of the comparison between the two approaches are presented in Fig. 7.2.

The error metrics were used to quantify the difference between contours. Tab. 7.2 shows the obtained results.

	HD	MAD	RMSD	DC
Endo	2.93 ± 1.39	1.13 ± 0.69	1.37 ± 0.77	0.83 ± 0.12
Epi	2.62 ± 1.49	0.96 ± 0.69	1.17 ± 0.80	0.90 ± 0.08
Overall	2.78 ± 1.45	1.04 ± 0.69	1.27 ± 0.79	0.87 ± 0.10

Table 7.2: Error metrics (mean ± standard deviation) for the comparison between automatically registered contours and manually traced ones in the analyzed sequences of Dataset A.

As reported, the overall mean HD is a less then 3 px, while the mean MAD is around 1 px.

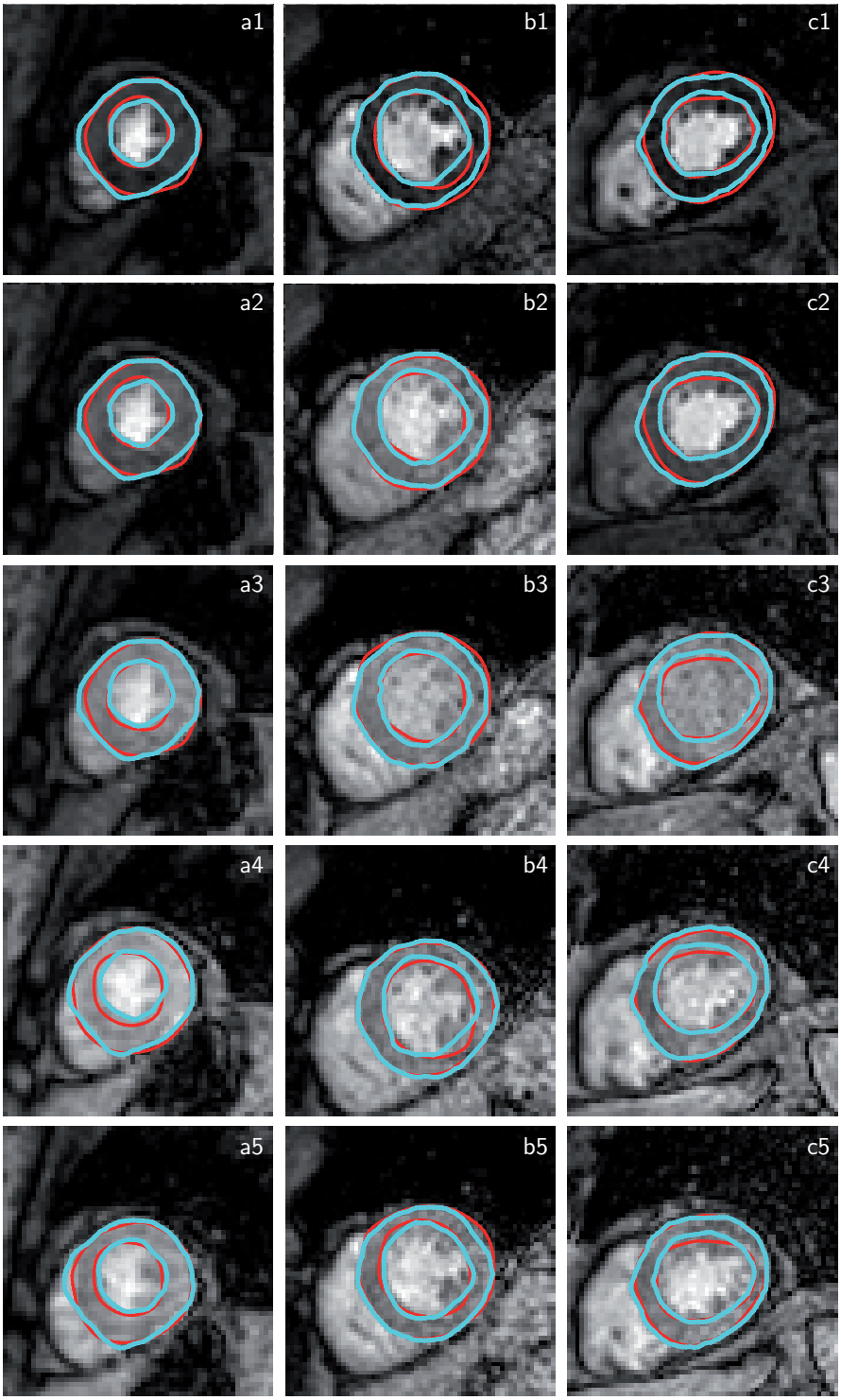

Figure 7.2: Frames showing the comparison between automatically generated contours (light blue) and manually traced ones (red). Each column (from a to c) contains frames from different patients, while different rows correspond to different moments in time during the sequence (from 1 to 5). Notably, the frames are not adjacent in time, but sampled through the sequence to testify the changes in pixel intensity due to contrast inflow.

7.4 Discussion

The synthetic dataset was used as a benchmark to test the performance of the registration scheme alone. The results show that the maximum measured error (estimated by HD) is around 1 px, demonstrating the robustness of the method. Notably, the errors were slightly higher at the epicardial boundary: this is probably due to the fact that in this dataset the difference in intensity between the myocardium and the background is statistically inferior to the one between the cavity and the myocardium, thus worsening the contours adaptation process in the former case. However, the difference is in the order of a 0.1 px and thus completely negligible.

Dataset A was used to compare the contours derived with the automated technique as a whole with those obtained with conventional manual tracing. The results of this comparison show that, on average, the distance between the two sets of contour (provided by MAD), is around 1 px. The reported values for the error metrics are comparable with those reported in the latest studies. For instance, Li *et al.* [23]) analyzed 20 sequences (comprised of 33 to 60 frames each) acquired in 13 patients. They reported a RMSD of 0.93 px for endocardial detection, 1.11 px for epicardial detection and 1.04 px overall. However, they did not perform the non-rigid registration process on automatically selected contours, but on manually traced ones, thus limiting considerably the possible sources of error. Furthermore, the comparison between results obtained in different patient cohorts, and using different imaging protocols, is an unsafe procedure, which allows to draw only approximative conclusions.

In summary, the measured errors committed by the proposed technique are comparable with the ones reported in other recently published studies. Importantly, the order of magnitude of the achieved accuracy is compatible with the clinical scenario.

Chapter 8

Clinical Validation

In Chapter 7 the presented technique was validated by quantifying the local and global discordance between automatically and manually extracted contours. Although this is a commonly adopted approach to judge the accuracy of techniques for object identification, it is not the best choice in the field of FP-CMR. The reason is that, due to the difficulty of correctly identifying anatomical structures through time in perfusion sequences, there is a high inter-operator variability related to conventional manual tracing. As a result, it is inappropriate to adopt manually identified contours as unique reference. This issue is explicitly treated by Wollny *et al.* [22] when approaching the validation of their registration method: "*These errors in the segmentation would show up as misregistrations when segmentation based statistics are used that analyze the myocardial boundary error or false-positive/false-negative pixels. [...] However, when assessing the performance of the intended task — perfusion analysis through intensity profiles — we confirmed that the influence of the segmentation differences was quite small, and hence, using intensity profiles obtained from manually segmented series as a gold standard for this comparison is still an effective approach for validation*". In other words, a more sound entity to be compared between automated and manual analyses is the pixel intensity variation over time of small regions located inside the myocardium. These contrast enhancement curves, which are less dependent on the traced contours, are in fact the real carriers of information regarding local perfusion, and therefore should be used to assess the accuracy of the technique.

Since the aim of the presented technique is to be adopted in the clinical environment, any validation process would be incomplete if no information about the diagnostic accuracy of the technique itself was given. Once contrast enhancement curves are extracted, both automatically and manually, perfusion indices can be computed for both approaches. These perfusion indices offer an indirect indication about the local myocardial blood flow, and can be adopted to discriminate between normally and abnormally perfused regions. In our

study, we compared the diagnostic accuracy of automatically and manually obtained perfusion indices to two different gold standards: qualitative visual interpretation of the acquired FP-CMR sequences and quantitative coronary angiography (QCA), which measures the extent of potential coronary stenosis. These comparison complete the large validation scheme adopted for the proposed technique.

In this Chapter, the validation of the proposed technique by means of clinically relevant quantities and methods will be pursued. Specifically, contrast enhancement curves will be extracted from both real datasets. Dataset A will be used to investigate whether the automated technique is able to produce high quality contrast enhancement curves and able to detect hyperemia (i.e. to recognize differences between stress and rest). Dataset B will be used to compare curves computed automatically with those extracted after manual tracing of myocardial contours. A set of perfusion indices will be derived from the curves and compared between automated and manual analyses. Finally, the diagnostic accuracy of automatically and manually obtained perfusion indices will be compared using two different gold standards: quantitative coronary angiography (QCA), which measures the lumen narrowing in presence of coronary stenosis, and qualitative visual interpretation of the acquired FP-CMR sequences. These comparisons complete the large validation scheme adopted for the proposed technique and show its reliability.

8.1 Quantification of Contrast Dynamics

Once the automated technique has been applied to an image sequence, the myocardial ROI, defined as the area between the endocardial and epicardial boundaries, is identified onto all frames. To allow the assessment of regional perfusion, the myocardial ROI is then uniformly divided into wedge-shaped segments following AHA guidelines [72]. According to these guidelines, the number of segments is 6 for both basal and mid levels, and 4 for the apical one, for a total of 16 segments (see Fig. 8.1, left). For anatomically correct orientation, the user is asked to select the anterior junction between the right ventricular free wall and the inter-ventricular septum in the reference frame. Finally, the changes of the mean pixel intensity in each segment are measured over time, resulting in time intensity curves. These are the so called contrast enhancement curves, which allow the quantification of the contrast dynamics and thus the estimation of local perfusion (see Fig. 8.1, right).

From each myocardial curve it is possible to compute indices in order to allow quantitative analysis. The quantities extracted from each curve are shown in Fig. 8.2.

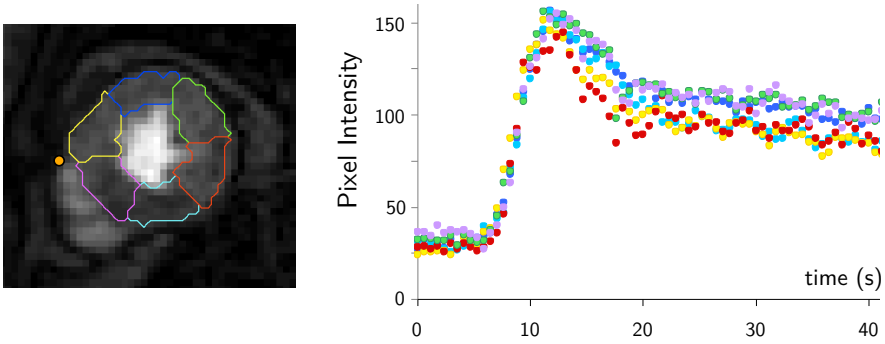

Figure 8.1: After the anterior junction of the right ventricular free wall with the inter-ventricular septum was manually identified (left, orange dot), myocardial segments were defined, and regional contrast enhancement was plotted over time for each segment (right). This example shows data obtained in a mid-ventricular slice during stress.

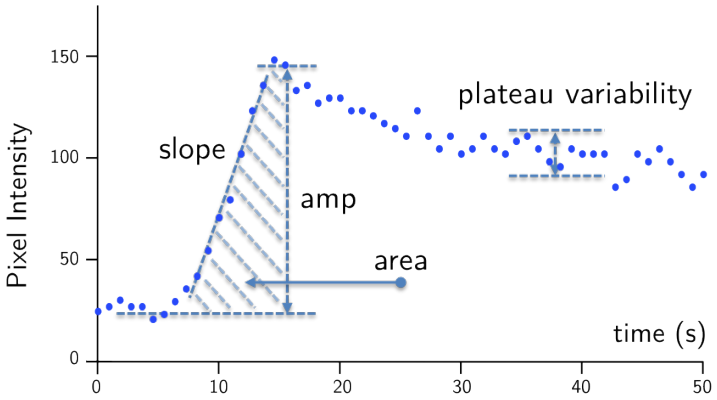

Figure 8.2: Definition of the indices extracted from each contrast enhancement curve.

Indices:

I. Peak-to-Peak Amplitude: distance between the baseline and the average of the three highest intensity values;

II. Slope: slope of the contrast enhancement phase. It is computed by means of a linear regression analysis;

III. Area: area between the curve and the baseline during the enhancement phase;

IV. Plateau Variability: standard deviation of at least 10 frames during the post-peak flat part of the curve.

The extraction is performed by manually selecting the beginning and the end of the contrast enhancement phase (i.e. the upslope part of the curve) and the plateau portion of the curve. This operation can be performed only once for all the curves extracted from the same sequence.

8.2 Quality Assessment and Detection of Hyperemia

The quality of the automatically extracted contrast-enhancement curves was assessed on Dataset A, since it consists in 15 subjects with normal perfusion (see § 6.2) imaged both at rest and during vasodilator stress. As a consequence, the analyzed perfusion sequences were 90. The assessment was performed either qualitatively, by visually judging the curves themselves, and quantitatively, by means of the defined indices. More specifically, a Signal-to-Noise Ratio (SNR) was defined as the ratio between the amplitude and the plateau variability extracted from each curve, both at rest and at stress. In addition, the computed indices were also used to test the ability of proposed technique to detect the expected hyperemic effects of the vasodilator agent. This goal was achieved by comparing amplitude and slope extracted from each segment between rest and stress using two-tailed paired student's t-tests.

Regional contrast enhancement curves clearly depicted the typical pattern of first-pass perfusion (see Fig. 8.1, right) in all image sequences obtained at both rest and stress. The results for SNR, slope and amplitude are reported in Tab. 8.1.

	SNR	Slope	Amplitude
Rest	17 ± 7	6.7 ± 2.3	65 ± 19
Stress	22 ± 8	15.6 ± 5.9	87 ± 25

Table 8.1: Results for SNR, slope (s^{-1}) and amplitude ($a.u.$) at rest and stress for Dataset A. The difference of both measured slope and amplitude values between rest and stress is statistically significant ($p < 0.000001$; paired t-test).

The measured SNR reflects excellent quality of the curves. As expected in subjects with normal perfusion, during stress, the upslope phase of the curves was steeper in all myocardial segments in all patients (see Fig. 8.3), indicating faster contrast inflow rate as part of the normal hyperemic response. In addition, the stress-induced increase in pixel intensity (i.e. the amplitude of the curve) was also significantly higher during stress, indicating increased concentration of contrast per unit myocardial volume.

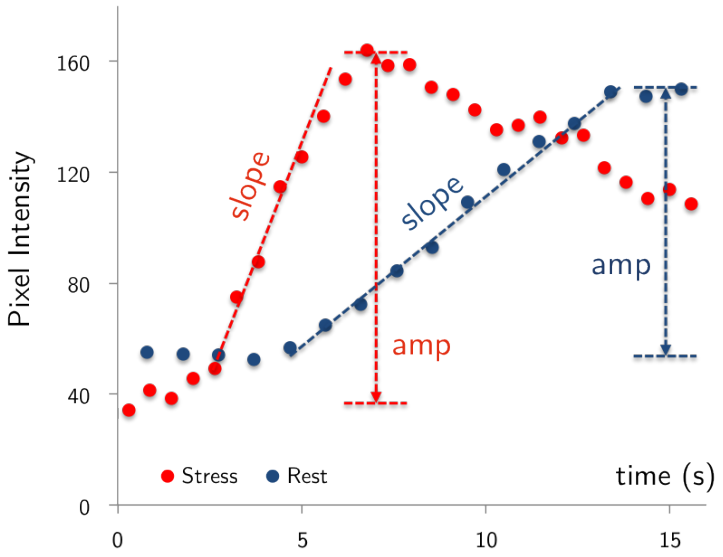

Figure 8.3: Example of contrast enhancement curves obtained in the mid-inferior segment during rest (blue) and stress (red). Note the increase in both the slope and the amplitude, reflecting the expected effects of stress.

8.3 Segmental Mean Intensity

Contrast enhancement curves were extracted applying the proposed technique to Dataset B (see § 6.2), which consists in 27 patients with suspected CAD acquired both at rest and stress, and thus comprises a total of 162 perfusion sequences. To further validate the technique, the sequences were also manually traced using commercial software (Argus®, Siemens Medical Solutions, Munich, Germany), and contrast enhancement curves were similarly computed. Mean pixel intensity in each automatically defined and manually traced segment was compared frame-by-frame for the resting images and separately for stress images. All inter-technique comparisons were performed using linear regression analysis with Pearson's correlation coefficient (R) and Bland-Altman analysis. Of note, the total number of compared intensity values is 21600 (27 patients $\times$ 16 segments $\times$ 50 frames) either for rest and stress.

Fig. 8.4 shows an example of FP-CMR images obtained at rest and during stress in a patient with significant CAD. Both the automatically and manually generated contrast enhancement curves showed very similar patterns, depicting a stress-induced perfusion abnormality in the inferior and lateral walls.

Fig. 8.5 shows the results of the comparisons between frame-by-frame segmental intensity values measured by means of the automated approach and through manual tracing. Excellent inter-technique agreement was noted both at rest and stress: R = 0.95, regression lines near unity and virtually zero

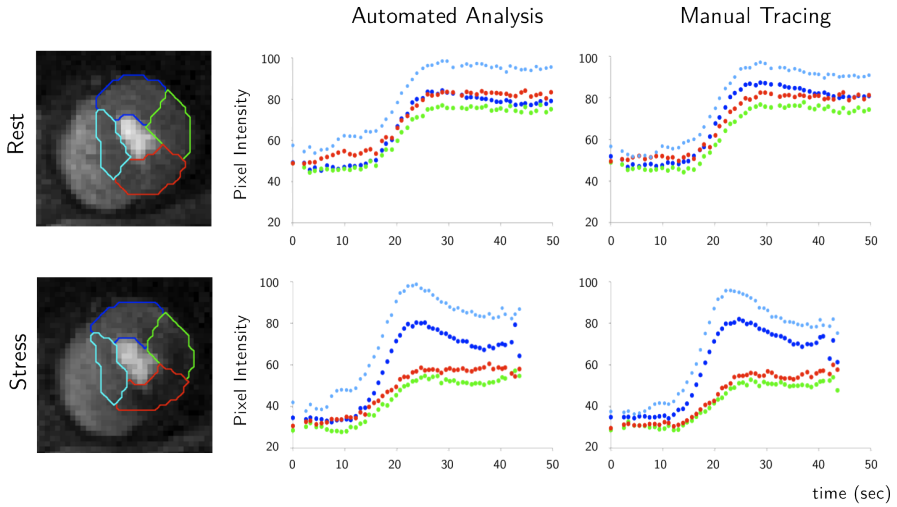

Figure 8.4: Example of FP-CMR images obtained at the apical LV level in a patient with stenosis greater than 50%. A stress-induced perfusion abnormality is visible in the inferior and lateral walls (bottom left). At rest, the automatically generated contrast enhancement curves (top middle) showed the same normal pattern in all segments. During vasodilation (bottom middle), both the amplitude and slope measured in the two non-affected myocardial segments (anterior and septal) increased considerably, in contrast to the two affected segments (inferior and lateral), where these indices were reduced. Manual tracing resulted in virtually identical curves (right).

biases with reasonably narrow limits of agreement (LOA). Separate analyses for basal, mid-ventricular and apical levels were also performed: the results, which are reported in Tabs. 8.2 and 8.3, show no significant differences from the overall results.

Bland-Altman Analysis

	Rest		Stress	
	Bias	LOA	Bias	LOA
Basal	1.4	11.2	-0.1	12.6
Mid	1.5	12.4	0.2	13.2
Apical	1.0	16.4	-0.3	15.7
Overall	1.3	13.1	0.0	13.7

Table 8.2: The results of Bland-Altman analysis both at rest and stress at different myocardial levels and overall.

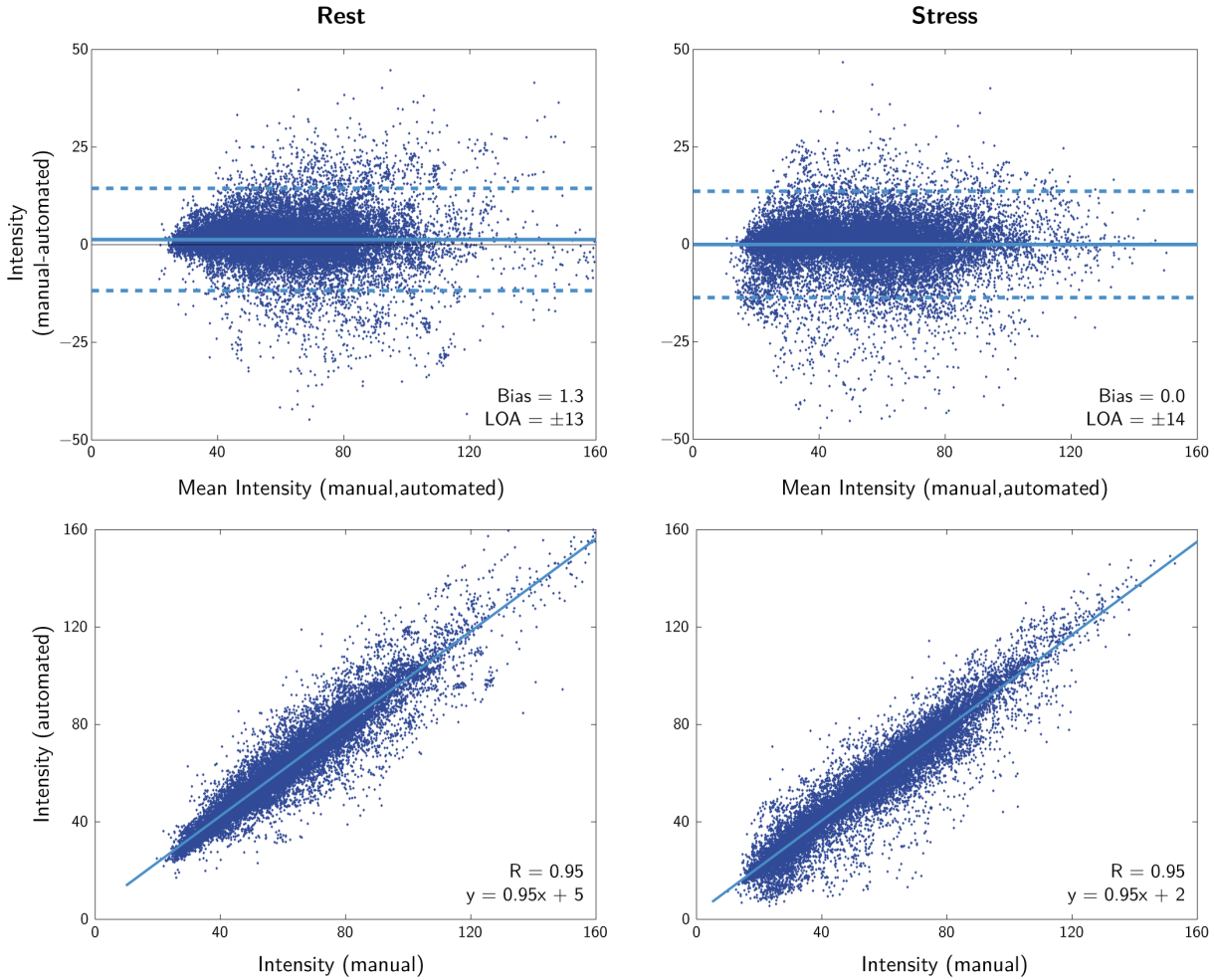

Figure 8.5: The results of Bland-Altman and linear regression analyses of segmental mean intensity derived from automatically and manually obtained contrast enhancement curves both at rest (left) and stress (right). LOA – 95% limits of agreement.

Correlation and Linear Regression Analyses

	Rest			Stress		
	R	m	q	R	m	q
Basal	0.94	0.94	5.0	0.94	0.95	2.6
Mid	0.94	0.97	3.5	0.95	0.94	3.1
Apical	0.94	0.94	5.6	0.95	0.97	1.8
Overall	0.95	0.95	4.6	0.95	0.95	2.4

Table 8.3: The results of correlation and linear regression analyses both at rest and stress at different myocardial levels and overall. Terms m and q are the coefficients of the regression line – $y = mx + q$.

8.4 Perfusion Indices

In § 8.1 the extraction of some indices from each contrast enhancement curve was defined. These quantities (a part from plateau variability) provide a quantitative evaluation of local myocardial perfusion, and have already been adopted in many study presented in literature [18][42][43]. In our study, we used the ones listed below:

Perfusion Indices:

I. Peak-to-Peak Amplitude;

II. Slope;

III. Product of Amplitude and Slope;

IV. Area.

These indices were extracted from each myocardial curve obtained both automatically and manually, both at rest and stress, in Dataset B. Thanks to the adopted dual-bolus acquisition technique (§ 6.2), in this dataset it was possible to extract an LV cavity intensity time curve (measured in a small circular ROI placed in the basal slice and multiplied by 10 to compensate for differences in contrast medium doses). This allowed to normalize each index by its respective LV cavity value. Finally, stress to rest ratio was calculated for each index (both non-normalized and cavity normalized) to reflect perfusion reserve of the indices.

To pursue the validation effort, we compared perfusion indices derived from automatically and manually generated contrast-enhancement curves. The results of this comparison are listed in Tab. 8.4.

Perfusion Indices

		R	m	q	Bias	LOA
Amp	**s**	0.90	0.89	4.8	0.25	12.8
	s/cav	0.92	1.05	-0.0013	0.0030	0.030
	s/r	0.87	0.88	0.22	0.016	1.08
	(s/cav)/(r/cav)	0.75	0.76	0.48	0.070	1.33
Slope	**s**	0.94	0.88	0.46	-0.18	1.72
	s/cav	0.94	1.05	-0.0017	0.00029	0.0156
	s/r	0.81	0.78	0.57	0.0069	2.16
	(s/cav)/(r/cav)	0.72	0.93	0.26	0.14	1.75
Amp*Slope	**s**	0.90	0.83	38	-17	205
	s/cav	0.90	0.88	0.00030	0.00000	0.0039
	s/r	0.83	0.90	0.32	-0.10	8.04
	(s/cav)/(r/cav)	0.72	0.88	0.55	0.21	4.12
Area	**s**	0.86	0.87	52	24	102
	s/cav	0.86	1.00	0.03	0.028	0.134
	s/r	0.45	0.43	0.69	0.030	1.76
	(s/cav)/(r/cav)	0.74	0.60	0.70	-0.20	4.70

Table 8.4: Results of the comparisons between perfusion indices derived from automatically and manually generated contrast enhancement curves: Pearson's correlation coefficient (R), linear regression analysis (y = mx + q) and Bland-Altman analysis (Bias ± LOA). Abbreviations: s – stress; r – rest; cav – cavity (either at stress or rest).

The analyses report high correlations, small biases and relatively narrow limits of agreement for most indices, and thus show that perfusion indices measured by the two techniques are in good agreement.

8.5 Diagnostic Accuracy against Coronary Angiography

In order to complete the validation process of the automated technique, the assessment of the diagnostic accuracy of the extracted indices had to be performed. The patients scanned for Dataset B were also analyzed by means of invasive Quantitative Coronary Angiography (QCA), which allows to estimate a potential reduction in the coronary artery luminal cross-sectional diameter. QCA can thus be adopted as a reference technique in comparing the diagnostic accuracy of automatically and manually extracted perfusion indices.

Comparisons were first done on a segment-by-segment basis. Each myocardial segment was classified as normal or abnormal based on the presence, location and severity of stenosis detected in the relevant coronary artery. Stenosis greater than 50% luminal narrowing was considered as evidence of significant CAD. The classification of myocardial segments was performed by an experienced interventional cardiologist, and was used as a reference for receiver operating characteristic (ROC) analysis. In particular, for each index, area under ROC curve (AUC) was computed separately per each one of the 16 myocardial segments and then averaged.

Sensitivity and specificity against QCA reference were calculated on a patient-by-patient basis. The condition required in order to consider a patient as abnormal was to display at least 2 adjacent abnormal segments.

Both segment-based and patient-based analyses were carried out separately for the manually and automatically generated curves, in order to allow comparisons of their diagnostic accuracy. Notably, of the 27 patients included in Dataset B, 21 were found to have significant stenosis on QCA: 9 had three-vessel, 5 two-vessel and 7 single-vessel disease. In these 27 patients, there were 215 segments supplied by arteries with stenosis greater than 50%, while the remaining 217 segments were supplied by arteries with no significant stenosis.

Tab. 8.5 shows the summary of the ROC analysis for perfusion indices obtained on a segment-by-segment basis for both the automated and manual techniques against QCA. For both techniques, the AUC varied among the calculated indices and ranged between upper 0.50s and lower 0.70s (having made the exclusion of the normalized area), but consistently showed highest values for the non-normalized values. Importantly, for all indices, normalized and non-normalized (by either LV cavity or resting value, or both), the AUC values were almost identical for the manual and the automated techniques, thus confirming the reliability of the proposed approach.

Tab. 8.6 shows the summary of the ROC analysis for perfusion indices obtained on a patient-by-patient basis. The calculated sensitivity and specificity of both techniques also varied among the calculated indices, with the automatically derived stress slope showing the best diagnostic accuracy (sensitivity 90% and specificity of 83%), which was better than the same index obtained

Segment-based Analysis against QCA			
		Automated	**Manual**
Amp	**s**	0.70	0.71
	s/cav	0.58	0.59
	s/r	0.58	0.58
	(s/cav)/(r/cav)	0.55	0.55
Slope	**s**	0.71	0.70
	s/cav	0.54	0.54
	s/r	0.56	0.58
	(s/cav)/(r/cav)	0.53	0.57
Amp*Slope	**s**	0.72	0.73
	s/cav	0.59	0.60
	s/r	0.59	0.58
	(s/cav)/(r/cav)	0.56	0.57
Area	**s**	0.53	0.53
	s/cav	0.58	0.56
	s/r	0.48	0.44
	(s/cav)/(r/cav)	0.50	0.48

Table 8.5: Results of the ROC analysis for perfusion indices obtained by both the automated and manual techniques using quantitative coronary angiography as a reference. Data are expressed as area under curve (AUC), calculated on a segment-by-segment basis. Abbreviations: s – stress; r – rest; cav – cavity (either at stress or rest).

by manual tracing (sensitivity 86% and specificity 50%).

Patient-based Analysis against QCA

		Automated		Manual	
		SE	**SP**	**SE**	**SP**
Amp	**s**	95	50	90	50
	s/cav	90	50	86	50
	s/r	76	50	81	50
	(s/cav)/(r/cav)	67	33	76	33
Slope	**s**	90	83	86	50
	s/cav	67	50	71	33
	s/r	90	67	81	67
	(s/cav)/(r/cav)	71	50	76	50
Amp*Slope	**s**	86	50	90	50
	s/cav	81	50	76	50
	s/r	95	67	90	67
	(s/cav)/(r/cav)	62	83	81	50
Area	**s**	76	67	86	17
	s/cav	81	50	81	50
	s/r	95	0	86	17
	(s/cav)/(r/cav)	90	17	71	33

Table 8.6: Results of the ROC analysis for perfusion indices obtained by both the automated and manual techniques using quantitative coronary angiography as a reference. Data are expressed as sensitivity (SE %) and specificity (SP %), calculated on a patient-by-patient basis.

8.6 Diagnostic Accuracy against Visual Interpretation

The diagnostic accuracy of both the automated and the manual techniques was also evaluated by comparing both techniques against visual interpretation of perfusion image sequences. Each myocardial segment was classified as normal or abnormal based on the presence of visually detectable hypo-enhancement during early phases of contrast wash-in. This classification was performed by a cardiologist experienced with CMR perfusion imaging, and was used as a reference for ROC analysis. For each index, area under ROC curve (AUC) was averaged for the 16 myocardial segments, similar to the comparisons with QCA described in § 8.5. These analyses were carried out separately for the manually and automatically generated curves to compare their accuracy against visual interpretation.

Finally, in order to demonstrate the superior diagnostic accuracy of the quantitative methods (either automated or manual) in comparison to qualitative analysis, K stats values were computed for each index against QCA. K stats are defined as the ratio between the number of concordant classifications and the total number of classifications.

Segment-based Analysis against Visual Interpretation

		Automated	Manual
Amp	**s**	0.60	0.63
	s/cav	0.71	0.75
	s/r	0.67	0.70
	(s/cav)/(r/cav)	0.65	0.68
Slope	**s**	0.61	0.60
	s/cav	0.73	0.73
	s/r	0.69	0.67
	(s/cav)/(r/cav)	0.71	0.72
Amp*Slope	**s**	0.61	0.64
	s/cav	0.73	0.78
	s/r	0.64	0.65
	(s/cav)/(r/cav)	0.69	0.74
Area	**s**	0.63	0.65
	s/cav	0.63	0.66
	s/r	0.56	0.61
	(s/cav)/(r/cav)	0.53	0.58

Table 8.7: Results of the ROC analysis for perfusion indices obtained by both the automated and manual techniques using visual interpretation as a reference. Data are expressed as area under curve (AUC), calculated on a segment-by-segment basis. Abbreviations: s – stress; r – rest; cav – cavity (either at stress or rest).

When using visual interpretation as a reference (see Tab. 8.7), AUC values varied among indices and ranged between lower 0.60s and upper 0.70s, and consistently showed highest values for cavity-normalized values. As for the comparisons against QCA, the AUC values were similar for the manual and the automated techniques.

Tab. 8.8 shows the K stats for perfusion indices extracted on a segment-by-segment basis using both automated and manual techniques together with visual interpretation against QCA. The computed values, again very similar for the two quantitative analysis, are higher than the one for the qualitative approach (equal to 0.58) for most indices.

Segment-based Analysis with K stats			
		Automated	**Manual**
Amp	**s**	0.73	0.71
	s/cav	0.64	0.64
	s/r	0.60	0.59
	(s/cav)/(r/cav)	0.62	0.60
Slope	**s**	0.74	0.73
	s/cav	0.62	0.59
	s/r	0.62	0.60
	(s/cav)/(r/cav)	0.60	0.62
Amp*Slope	**s**	0.74	0.74
	s/cav	0.62	0.62
	s/r	0.60	0.57
	(s/cav)/(r/cav)	0.62	0.59
Area	**s**	0.59	0.60
	s/cav	0.63	0.61
	s/r	0.51	0.48
	(s/cav)/(r/cav)	0.54	0.52
Visual Analysis		0.58	

Table 8.8: K stats calculated on a segment-by-segment basis for both the automated and manual techniques, together with visual assessment, using quantitative coronary angiography as a reference.

8.7 Discussion

In this Chapter, a detailed validation of the proposed technique was presented. Differently from what done in Chapter 7, perfusion image sequences acquired during pharmacological stress were analyzed. Stress testing is known to provide far less favorable conditions for CMR imaging, since it involves higher heart rates, allowing less time to image acquisition to be performed. Stress images are also challenging from the analysis point of view, because breath-holding under vasodilator agents is often difficult for the patient, resulting in increased cardiac translation and accentuated changes in the shape of the heart. The results presented in § 8.2 demonstrated that the proposed technique is suitable not only for analysis of resting perfusion image sequences, but also for images acquired during peak stress, as reflected by SNR values of the order of magnitude of 20. This number indicates that the increase in myocardial pixel intensity caused by the contrast bolus is 20 times the amplitude of the noise in the contrast-enhancement curves, depicting the excellent quality of these curves. In addition, we found that curves generated using our algorithm showed the expected distinctly different patterns between rest and stress in normally perfused hearts.

The remaining part of the validation process was performed on Dataset B, which was acquired at a different institution, using different equipment with different imaging settings in order to test the robustness of the technique. Of note, the algorithms worked changing only two internal parameters, as described in § 6.3. The reported results achieved through the comparison of segmental mean intensities between automated and manual analysis, in this context, are extremely positive. The studied perfusion indices, including their normalized versions either by corresponding LV cavity values and/or by rest values, showed high levels of agreement between automated and manual techniques, indicating that the former could be a useful alternative to the tedious and time-consuming standard methodology. Of note, the lowest levels of agreement were found for the stress to rest ratios of the cavity normalized indices, probably because of compounding errors originating from multiple divisions. Moreover, the Area index was the one showing the worst results in the whole analysis, probably due to its high dependency on the baseline value as well as on the selection of the contrast enhancement phase, which was performed manually.

The final step of validation of our technique was the side-by-side comparison of its diagnostic accuracy with that of the manual technique against reference methods for the detection of obstructive CAD. The analysis was performed initially using QCA as a reference, both on a segment-by-segment and on a patient-by-patient basis. As indicated, the segment-based analysis was accomplished performing a separate ROC analysis per each myocardial segment. The reason behind this choice lies in a consideration relative to the image acquisition process: it has been reported that the relative distance of myocardial segments to the receiving coil array causes inhomogeneities in acquisition sensitivity and, thus, differences in image brightness [73]. Although the acquisition protocol adopted for Dataset B should take care of this issue and generate normalized images [43], it is safer to perform a separate ROC analysis for each myocardial segment. While the diagnostic accuracy of several indices was very good (slope, for instance), it is possible to argue that the AUC values of some indices obtained by either of the two techniques were not very high. This is not surprising for two reasons. First, it is well established that one cannot expect a perfect agreement between severity of coronary lesions, as determined by angiography, and their manifestation in terms of perfusion [74]. Second, the ROC analysis was performed on a segment-by-segment basis, which involves a certain level of uncertainty regarding the correspondence between coronary territories and myocardial segments. Segment-by-segment or even territory-by-territory analysis of diagnostic accuracy does not usually yield high levels of accuracy, even for well-established techniques such as Nuclear myocardial perfusion Imaging [75]. Since the true clinical value of a diagnostic technique should be tested

on a patient-by-patient basis, this analysis was performed and its outcome was presented. However, differently from the segment-based one, the patient-based analysis was strongly limited by a referral bias, since all the patients were referred for cardiac catheterization based on abnormal nuclear cardiology findings, i.e. the group was biased in terms of high prevalence of disease (21 abnormal vs 6 normal patients). Nevertheless, in this cohort, the diagnostic accuracy of both techniques was similar. The last paragraph compared the diagnostic accuracy of the quantitative analyses to the one of qualitative one using QCA as a reference. Importantly, K stats analysis showed that the quantitative methods (automated and manual) are characterized by similar accuracy and yield, in most cases, better results compared to visual interpretation, thus demonstrating the clinical usefulness of the proposed methodology.

Chapter 9

Conclusion

The study was aimed at the design, the implementation and the validation of a novel approach for myocardial identification as a basis for perfusion quantification from CMR images. The proposed technique features statistical region-based and edge-based level-set techniques as well as a non-rigid registration scheme. The achieved results demonstrate that the technique is able to deal with the extreme dynamic nature of FP-CMR image sequences and rapid respiratory motion, allowing the extraction of high-quality contrast enhancement curves both at rest and during vasodilator stress. Importantly, we found high levels of agreement between automatically and manually obtained perfusion indices as well as similar diagnostic accuracy against QCA reference and visual interpretation.

In summary, our technique provides a fast, automated and user-friendly alternative to the prevailing manual methodology for measurement of myocardial contrast enhancement, which has been delaying the dissemination of quantitative evaluation of myocardial perfusion from CMR images.

Part II

Related Projects

Chapter 10

Left Ventricular Modelling: a Quantitative Functional Assessment Tool based on CMR Imaging

C.A. Conti, E. Votta, C. Corsi, D. De Marchi, **G. Tarroni**, M. Stevanella, M. Lombardi, O. Parodi, E.G. Caiani, and A. Redaelli

Interface Focus 2011; 1:384-395.

Abstract

Purpose. We present the development and testing of a semi-automated tool to support the diagnosis of left ventricle (LV) dysfunctions from cardiac magnetic resonance (CMR).

Methods. CMR short-axis images of 15 human LVs were processed to detect endocardial and epicardial contours and compute LV volume, wall mass, and regional wall motion. Results were compared to the ones from manual tracing by an expert cardiologist. Moreover, nearest neighbour tracking and finite element theory were merged to calculate local myocardial strains. The method was tested on a virtual phantom, whose strains were also computed by a commercial finite element solver, on a healthy LV and on two ischemic LVs with different severity of the pathology.

Results. Automated analysis of CMR data was feasible in 13/15 patients: computed LV volumes and wall mass well correlated with manually extracted data. The detection of regional wall motion abnormalities showed good sensitivity (77.8%), specificity (85.1%) and accuracy (82%). On the virtual phantom, computed local strains differed by less than 14% from the results of commercial finite element solver. Strains calculation on the healthy LV showed uniform and synchronized circumferential strains, with peak shortening of about 20% at end systole, and progressively higher systolic wall thickening going from base to apex. In the two pathological LVs, synchronicity and homogeneity were partially lost, anomalies being more evident for the more severely injured LV.

Conclusions. Preliminary testing confirmed the validity of our approach, which allowed for the fast analysis of LV function, even though future improvements are possible.

10.1 Introduction

Ischaemic cardiomyopathy is responsible for up to 65 per cent of the prevalence of heart failure (HF) [76]. Despite appropriate medical management, myocardial infarction initiates a remodelling process that potentially entails left ventricle (LV) dilation and mitral valve (MV) insufficiency, often proportional to the extent of damaged myocardium. To compensate for reduced ventricular function, the LV dilates to increase stroke volume through two distinct phases governed by mechanical, genetic and neurohormonal factors [77]: early remodelling, characterized by infarct expansion with wall thinning and LV dilation with subsequent increase in wall stress, and late remodelling, in which increased wall stress induces cardiomyocytes hypertrophy. Unfortunately, remodelling leads to alterations in the LV architecture towards a spherical form, further increasing wall stress, resulting in a vicious cycle leading to HF.

Imaging techniques play a pivotal role in LV function assessment in supporting clinical decision-making. Among them, cardiac magnetic resonance (CMR) imaging is a non-invasive technique currently considered the standard reference in the clinical evaluation of the LV.

Conventional two-dimensional cine images are normally used to asses LV volume, function, mass and regional dysfunction [78][79]. However, their analysis requires slice- by-slice, phase-by-phase endo- and epicardial boundaries detection. Even with commercial software, it requires extensive manual corrections, thus resulting in a poorly automated, time consuming and subjective analysis technique. Different techniques for CMR LV semi-automated and automated border detection have been described [80], but they suffer from different limitations: a large number of manually segmented images required to build a model database or to train the model [81], analysis limited to end-diastolic (ED) and end-systolic (ES) phases only, no continuous temporal segmentation and computational complexity [82].

Tagged-CMR is widely adopted to calculate two-dimensional wall strains by tracking the two- dimensional motion of myocardial points (defined by tags crossing) over time; it permits rapid imaging and visualization, as well as automation [83]. However, this technique does not capture real three-dimensional strains and does not allow for the analysis of the complete cardiac cycle, since the tags (i) can become less distinct, and thus more difficult to track, owing to out-of-plane motion of the tissue, and (ii) fade after a few time- frames, so that the analysis cannot be extended to the entire cardiac cycle. Moreover, only a few slices are acquired via tagged-CMR as additional sequences to the conventional examination. The assessment of three- dimensional myocardial motion using MR tagging techniques using multiple orthogonal image planes [84][85][86] or fully three-dimensional MR tagged imaging [87] is still part of the research arena and is primarily limited by the need for lengthy image ac-

quisition protocols and for tedious post-processing procedures.

The availability of a reliable technique for automated endocardial and epicardial contour detection and regional wall strain calculation throughout the cardiac cycle on conventional cine CMR images would overcome these limitations, providing an exhaustive quantitative analysis of the LV.

Within the framework of the virtual pathological heart of the virtual physiological human (VPH2) project, we aim at developing two decision support tools for cardiologists and cardiac surgeons, based on LV patient-specific modelling, the functional assessment tool (FAT) and the functional predictive tool (FPT). FAT quantitatively analyses LV, by semi-automated endocardial and epicardial detection, andMV function from CMR images, thus help- ing defining the severity and extent of disease in patients with LV dysfunction,with or without mitral regurgitation. FPT is used for an easy and fast simulation of post-operative scenarios subsequent to different surgical procedures.

The present paper is focused on the development, testing and validation of the LV-related capabilities of the FAT: (i) semi-automated detection of endocardial and epicardial contours for volumetric and wall motion (WM) analysis; (ii) quantification of LV volume, mass and regional WM; and (iii) computation of local strains in the myocardium. FAT contour detection was verified on a small population of subjects (n = 13), while its capability to correctly compute local LV wall strains was tested on a virtual phantom and on three real ventricles characterized by different clinical scenarios.

10.2 Methods

Cardiac magnetic resonance imaging

A group of 15 patients with previous myocardial infarction and regional WM abnormalities was considered. CMR studies were performed using a 1.5 T scanner (Signa Hdx®, GE Healthcare, Milwaukee, WI, USA). An eight-element cardiac phased-array receiver surface coil with breath-holding in expiration and ECG-gating were used for signal reception. Three standard cine long-axis slices and a stack (from 8 to 12) of contiguous cine short-axis slices from the atrioventricular ring to the apex were acquired using a steady-state free-precession pulse sequence (30 phases, slice thickness 8 mm with no overlap and no gap, field of view = 40 cm, reconstruction matrix 256×256, repetition time = 3.5 ms, echo time = 1.5 ms, flip angle 45°).

Algorithms for contours detection

The semi-automated detection of LV contours was based on region-based image noise distribution (for LV endocardial detection) and on edge-based image

gradient (for LV epicardial detection).

Endocardial border detection. The endocardial border detection is based on the formulation proposed by Chan & Vese [64] and on embedding in the segmentation model the *a priori* knowledge of the statistical distribution of grey levels in medical images [88]. In particular, concerning CMR, we note that image pixels are modelled as Gaussian distributed random variables. Then the proposed method drives the curve evolution to achieve a maximum-likelihood segmentation of the target, with respect to the statistical distribution law of image pixels.

Let us consider an image I as a real positive function defined in a domain $\Omega \subset \mathbb{R}^2$. The gray levels are assumed to be uncorrelated and independently distributed. They are thus characterized by their respective probability density. Now, we define a closed curve C partitioning the image domain in an 'inside' Ω_i and an 'outside' Ω_e and denote with $P_i = \prod_{\Omega_i(C)} p(I)$ the probability of the random field inside the curve and with $P_e = \prod_{\Omega_e(C)} p(I)$ the probability outside the curve. Without any *a priori* knowledge about the shape of the object to be detected, we look for the curve C that maximizes the likelihood function given by the product of the inner and the outer probability [89]: $P[I|C] = P_i P_e$.

Since the log function is strictly increasing, the maximum value of $P[I|C]$, if it exists, will occur at the same points as the maximum value of $l(I, C) = log\big(P[I|C]\big)$. This function is the 'log likelihood' and in many cases it is easier to work with it than with the likelihood function. Indeed, the product structure of the probability function is transformed in a summation or integral structure of the log likelihood. Passing to the continuous limit, we replace the sum with the integral and, to perform a maximum-likelihood segmentation of the target, we need to maximize the functional I with respect to variation of the curve C.

By considering the Gaussian noise distribution:

$$p(I) = \frac{1}{\sqrt{2\pi}\sigma} exp\left[-\frac{1}{2}\left(\frac{I-\mu}{\sigma}\right)^2 \right] \tag{10.1}$$

where μ and σ are the average and variance of I, respectively, the corresponding log-likelihood is derived as in Chesnaud *et al.* [90]. Then, following the model proposed by Chan & Vese [64] and embedding in the segmentation model the *a priori* knowledge of statistical distribution of grey levels in CMR images [65], the final associated flow results[1]:

$$\frac{\partial \phi}{\partial t} = |\nabla \phi| \left[\epsilon div\left(\frac{\nabla \phi}{|\nabla \phi|}\right) + log\left(\frac{e_i}{e_e}\right) + f_i - f_e \right] \tag{10.2}$$

where

$$A_i = \int_{\Omega_i(C)} dxdy \qquad A_e = \int_{\Omega_e(C)} dxdy \tag{10.3}$$

[1]The following equation has been rewritten to improve legibility.

$$B_i = \int_{\Omega_i(C)} I dxdy \qquad B_e = \int_{\Omega_e(C)} I dxdy \tag{10.4}$$

$$C_i = \int_{\Omega_i(C)} I^2 dxdy \qquad C_e = \int_{\Omega_e(C)} I^2 dxdy \tag{10.5}$$

$$f_{i,e} = \frac{A^2 I^2 - 2IAB + 2B^2 - AC}{AC - B^2} \tag{10.6}$$

$$e_{i,e} = \frac{AC - B^2}{A^2} \tag{10.7}$$

and $\phi(x, y, 0)$ is the initial function with the property that its zero-level set corresponds to the position of the initial front. Typically, it is defined by $\phi(x, y, 0) = \pm d$, where d is the signed distance function from each point to the initial front [57], and

$$\frac{\delta(\phi)}{|\nabla\phi|} \frac{\partial\phi}{\partial \mathbf{n}} = 0 \tag{10.8}$$

are the boundary conditions.

The evolution process will stop when the region probability terms of the inside regions do equal the terms of outside regions, up to regularization of boundaries (see Fig. 10.1, a).

To define the initial function, we require the manual placement of a single point inside the LV cavity. From a mathematical point of view, we defined a curve C, centred in the manual selected point, as the zero-level set of an implicit real function ϕ taking values on the image domain Ω:

$$C = \{(x, y) \in \Omega : \phi(x, y) = 0\} \tag{10.9}$$

This initial circumference C undergoes the evolution described in equation (10.2) in order to maximize the functional l.

Following this step, the boundary regularization was achieved using a curvature-based motion not allowing curvature above the mean Euclidean curvature value of the detected contour and designed to automatically include the papillary muscles in the LV cavity (see Fig. 10.1, b).

Epicardial border detection. To identify the epicardial boundary (see Fig. 10.1, c), we drove the evolution of an initial contour applying the well-known Malladi–Sethian model for active contour evolution, which requires adequate boundary conditions.

The model includes a dependence of the speed on the curvature, a propagation expansion speed and an advection speed based on the image gradient:

$$\frac{\partial\phi}{\partial t} = \nu\nabla g \cdot \nabla\phi - g(\lambda\kappa - 1)|\nabla\phi| \tag{10.10}$$

where κ is the mean curvature, g is the edge indicator, ν and λ are weighting coefficients.

The edge indicator g is a non-increasing function of the gradient of the initial image [61]:

$$g = \left[1 + \left(\frac{|\nabla I|}{\alpha}\right)^2\right]^{-1} \tag{10.11}$$

The parameter α depends on the characteristics of the noise in the image: α controls the sensitivity to edges and therefore it was empirically set to 20 to select the contrast of the objects we want to consider in the image during the motion of the embedding. The parameter ν is used to limit the regularization of the contour controlled by the parameter λ: these parameters were set equal to 10 and 6, respectively.

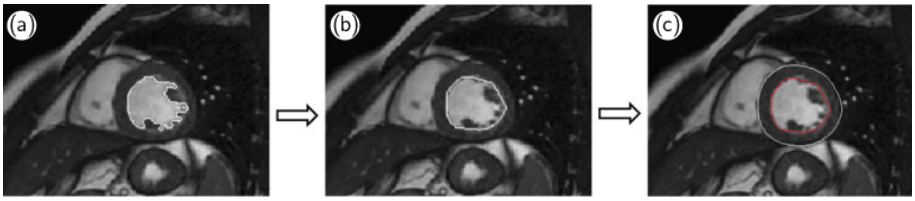

Figure 10.1: Schematization of the border detection procedure: (a) after initialization of one point inside the LV cavity, the algorithm based on the region-based image noise distribution iterates expanding the cavity position; (b) a second step algorithm, based on curvature-based motion, is then applied to regularize the contour and thus include papillary muscles and ventricular trabeculations inside the LV cavity, thus producing the final position of the endocardial contour; (c) the Malladi–Sethian model for active contour evolution is then applied starting from the detected endocardium (in red) in order to determine the epicardial position (in white).

The contour evolution will have a steady-state solution when the geometry dependent and expansion terms balance the advection term [57]. At the end of this step, the epicardial boundary was also regularized applying a modified curvature motion.

Algorithms initialization. For endocardial detection, the region-based approach was applied from basal to apical slices for each frame. In the basal slice, after initialization of the algorithm's parameters (radius of the initial circle, and per cent of radius decrement from one slice to the next one), the operator selected one point inside the LV cavity. Then, automatically, the applied algorithm expanded the initial circle according to the videointensity probability distribution followed by the regularizing expansion to include the papillary muscles, when present. Then, the algorithm processed the other slices, using the detected contour on the current slice (s) as initialization for the next ($s+1$) slice, after reducing it by the per cent set by the operator.

For epicardial detection, this approach required a robust initialization on the first frame f. Then, for the next frame $f+1$, the initialization was obtained by applying the 'erode' morphological operation applied to the resulting epicardial contour on the frame f.

For each slice and frames, the detected contours were then superimposed to the original image, to allow for possible corrections, if needed.

Left ventricle volume and mass quantification

The LV volume was automatically computed by sum- ming the LV area in each slice (measured as pixel counts inside the endocardial contour) multiplied by the pixel spatial resolution and by the slice thickness (from the DICOM header). In the same way, the LV mass was computed as the difference between the LV epicardial and LV endocardial volumes, and multiplied by 1.05 to be expressed in grams.

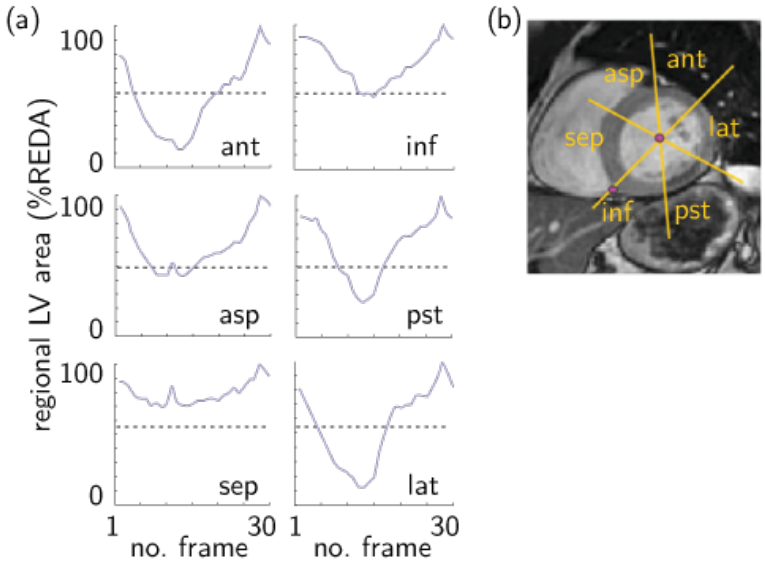

Figure 10.2: (a) Schematization of the definition of the six sectors for wall motion (WM) interpretation: ant, anterior; asp, antero-septal; sep, septal; inf, inferior; pst, posterior; lat, lateral (see text for more details). (b) Example of the regional WM curves obtained by the endocardial detection throughout the cardiac cycle in one slice at mid LV level. The grey dotted line in each graph represents the 50% threshold applied to regional area change values to automatically detect WM abnormalities. In this example, the septal sector (sep) was automatically interpreted as abnormal.

For the automated interpretation of regional WM, the ED frame was used to define the standard segmentation scheme for the LV short-axis view in each slice (see Fig. 10.2, b). In the slice at the mid-ventricular position, the ED

centroid of the LV cavity was calculated as centre of mass of the binary image representing the detected LV cavity, in which all pixels in the cavity appear 'on' (i.e. have value 1) and have been attributed with a unit mass, and used as the origin of segmentation.

An additional point was then manually placed at the junction between the right ventricular free wall and the interventricular septum. Starting from that point, the LV cavity was divided into six 60° wedge-shaped segments, corresponding to those used for visual assessment and grading of WM. For each segment, regional fractional area (RFA) in per cent of regional ED area was automatically calculated throughout the cardiac cycle using a fixed-coordinate reference system. From these six curves in each slice, RFA change (RFAC) was computed as the difference between the maximum and minimum value of RFA, expressed in per cent of the regional ED area. For each segment, these values were used to automatically interpret WM as normal (RFAC $\geq 50\%$) or abnormal (RFAC $< 50\%$) (see Fig. 10.2, a).

Validation of left ventricle volume and mass quantification

For validation purposes, data calculated through our semi-automated procedure were compared with the manual measurements performed by an expert cardiologist. The latter analyzed CMR data using commercial software (MASS®v. 6.1,Medis, Leiden, Netherlands) installed on the MRI workstation and proceeded into the conventional analysis of these images by manual tracing LV endo- and epicardial contours. Then, LV ED and ES volumes (EDV and ESV, respectively) and mass were measured using standard volumetric techniques. The same number of slices included for the reference value assessment by the expert were included in these computations, to avoid bias owing to the inclusion of a different number of slices.

Moreover, dynamic images were reviewed and regional WM was interpreted in three slices selected at apical, mid and basal levels. In each of these slices, the six regional segments (anterior, lateral, antero-lateral, septal, inferior and posterior) were qualitatively graded as normal or abnormal, thus providing the 'gold standard' for WM interpretation.

The results obtained from the automated analysis were then compared with the reference values by (i) linear regression and Bland–Altman analyses for LV volumes and mass; (ii) levels of agreement between the cardiologist WM grades and the automated classification of regional WM.

Sensitivity, specificity and accuracy for the automated interpretation of WM were also computed.

Calculation of left ventricle local strains and left ventricle torsion

Local strains in the LV myocardium were calculated through the following steps:

I. A slice-based reconstruction method [91] was used to obtain smooth, three-dimensional endocardial and epicardial surfaces, discretized into three-node triangular elements, from the sampled previously detected contours (see Fig. 10.3, a and b);

II. In the ED frame, endocardial and epicardial surfaces were divided into six longitudinal sections and three circumferential sections, for a total of 18 sectors (see Fig. 10.3, c). For each sector, its eight vertices were identified and the corresponding local principal curvatures calculated as in Vieira & Shimada [92];

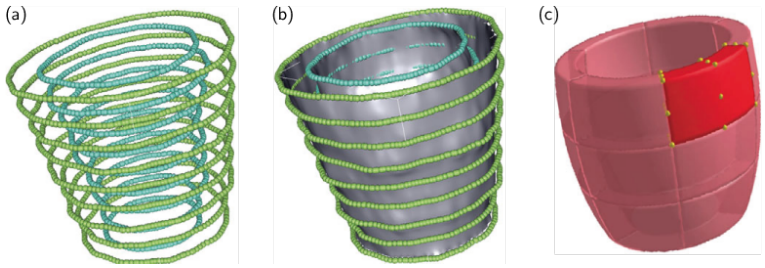

Figure 10.3: (a) Points obtained by sampling the endocardial (blue) and epicardial (green) contours. (b) Three-dimensional smooth endocardial and epicardial surfaces. (c) Sketch of LV segments.

III. The eight vertices of each sector were tracked throughout the subsequent time-points by means of a nearest neighbour search, assuming that the position of a given point P on the LV surface and the surface's local shape in P change continuously throughout the cardiac cycle, and thus undergo small changes in a sufficiently short time-frame. Briefly, at the time-point t, the position of P on the triangulated surface S_t is $\mathbf{x_t}$. At $t+1$, the triangulated surface S_{t+1} is deformed, and P has moved to its new position $\mathbf{x_{t+1}}$,estimated as the position of the node in S_{t+1} that minimizes the following function:

$$\begin{aligned}\phi(\mathbf{x_{t+1}}, \mathbf{x_t}, \mathbf{x_0}) = a_1\big(|\mathbf{x_{t+1,i}} - \mathbf{x_t}|^2\big) + a_2\Big[\big(K^1_{t+1,i} - K^1_t\big)^2 + \\ + \big(K^2_{t+1,i} - K^2_t\big)^2\Big] + a_3\big(|\mathbf{x_{t+1,i}} - \mathbf{x_0}|^2\big)\end{aligned} \tag{10.12}$$

where $\mathbf{x_{t+1,i}}$ is the position of the ith node on the surface S_{t+1}, $\mathbf{x_t}$ and $\mathbf{x_0}$ are the known positions of P at t and at ED, K^1 and K^2 are the

curvature tensor principal components and $a1$, $a2$, $a3$ are three positive scalar coefficients defined as:

$$a_1 + a_2 = 1 \tag{10.13}$$

and

$$a_3 = \begin{cases} 0, & t < 12 \\ (1/9)(t-12), & t \geq 12 \end{cases} \tag{10.14}$$

In the first term of ϕ, $|\mathbf{x_{t+1,i}} - \mathbf{x_t}|$ is the displacement needed to move P from its initial position $\mathbf{x_t}$ to its new one. The second term accounts for the change in local shape experienced by the surface, where $\left(K^1_{t+1,i} - K^1_t\right)$ and $\left(K^2_{t+1,i} - K^2_t\right)$ are the concomitant changes in local principal. In both terms, quadratic quantities are considered; thus, their convex linear combination is minimized if both terms are minimized. The coefficients a_1 and a_2 were set to 0.2 and 0.8, respectively, accordingly with a preliminary sensitivity analysis. The third term of the function is active only for $t \geq 12$, i.e. for the diastolic time-points, and enforces the return of the tracked point P to its initial position. The nearest neighbours search provided the time-dependent position of the eight vertices of each of the 18 sectors of the LV myocardium and, thus, the corresponding time-dependent displacements;

IV. A continuos displacement field was reconstructed within each sector by treating the latter as an eight-node isoparametric hexahedral finite element. A local system of coordinates $\mathbf{s} = (s_1, s_2, s_3)$ was defined, with $s_i \in [-0.5; 0.5]$ and with s_1, s_2, s_3 aligned, respectively, along the local circumferential, radial and axial directions of the LV in a cylindrical reference system with the z-axis on the LV long axis. Coordinates and displacements of each point within the sector were estimated by interpolating the coordinates and the displacements of the eight vertices via linear shape functions:

$$\mathbf{x}(\mathbf{s}) = \sum_{i=1}^{8} N_i(\mathbf{s}) \cdot \mathbf{x_i} \tag{10.15}$$

$$\mathbf{u}(\mathbf{s}) = \sum_{i=1}^{8} N_i(\mathbf{s}) \cdot \mathbf{U_i} \tag{10.16}$$

The strain tensor was computed as

$$\begin{aligned} \mathbf{E} &= \frac{1}{2}(\mathbf{C} - \mathbf{I}) \\ &= \frac{1}{2}\left(\mathbf{F}^T\mathbf{F} - \mathbf{I}\right) \\ &= \frac{1}{2}\left[(\mathbf{H} + \mathbf{I})^T(\mathbf{H} + \mathbf{I}) - \mathbf{I}\right] \\ &= \frac{1}{2}\left(\mathbf{H} + \mathbf{H}^T + \mathbf{H}^T\mathbf{H}\right) \end{aligned} \tag{10.17}$$

where $\mathbf{C}$ is the right Cauchy-Green strain tensor, $\mathbf{F}$ is the deformation gradient tensor, defined as $\mathbf{F} = \partial\mathbf{x}/\partial\mathbf{X}$, i.e. the derivative of the current position $\mathbf{x}$ as regard to the initial position $\mathbf{X}$, and $\mathbf{H}$ is the displacement gradient tensor, defined as $\mathbf{H} = \partial\mathbf{u}/\partial\mathbf{X}$, i.e. the derivative of the displacement $\mathbf{u}$ as regards to the initial position $\mathbf{X}$. $\mathbf{H}$ was computed as:

$$\mathbf{H} = \frac{\partial \mathbf{u}}{\partial \mathbf{X}} = \frac{\partial \mathbf{u}}{\partial \mathbf{s}} \cdot \frac{\partial \mathbf{s}}{\partial \mathbf{X}} = \sum_{i=1}^{8} \mathbf{U_i} \frac{\partial N_i}{\partial \mathbf{s}} \cdot \mathbf{J}^{-1} \tag{10.18}$$

where $\mathbf{J}$ is the Jacobian matrix that maps the global coordinates onto the local ones, i.e. $\mathbf{x} = \partial\mathbf{X}/\partial\mathbf{s}$.

In particular, the strain tensor $\mathbf{E}$ was assessed at the centre of each sector ($s_1 = s_2 = s_3 = 0$);

V. For the six vertexes at the basal end of the endocardial surface, and for the six vertexes at its apical end, the time-dependent average rotation angle θ_{rot} was computed. In an orthonormal reference system x, y, z centred in the LV centre of mass, with the z-axis aligned with the long-axis, θ_{rot} was defined as:

$$\theta_{rot}(t) = \frac{1}{6} \sum_{i=1}^{6} \left[\tan^{-1} \frac{y_i(t)}{x_i(t)} - \tan^{-1} \frac{y_i(0)}{x_i(0)} \right] \tag{10.19}$$

Positive values of $\theta_{rot}(t)$ corresponded to a counter-clockwise rotation as seen from the LV apex. The ventricle torsion was computed as:

$$torsion(t) = \theta_{rot}^{apical}(t) - \theta_{rot}^{basal}(t) \tag{10.20}$$

Validation of local strains calculation

The validation of the method for strains calculation consisted of two steps.

First, we tested its capability to compute strains on objects with simple geometry undergoing simple deformation processes. For this purpose, a virtual phantom, consisting in an ideal, axial-symmetric ventricle was defined and discretized into tetrahedral elements (see Fig. 10.4, a). By means of a commercial finite-element solver (ABAQUS®, Simulia Inc., Dessault Systèmes, Vélizy-Villacoublay, France), we simulated its inflation and deflation under the effect of a cyclic, time-dependent inner pressure. The phantom was divided into 18 sectors. The corresponding strains were computed by nearest neighbour tracking of the sectors' vertices, and compared with the values computed by the commercial solver for the tetrahedral elements located at the centre of each sector.

Second, we assessed the method's capability to compute strains in the presence of more complex motion patterns, characterized by non-uniform expansion and deflation, and by torsion.We analyzed a normal subject (SUBJECT1),

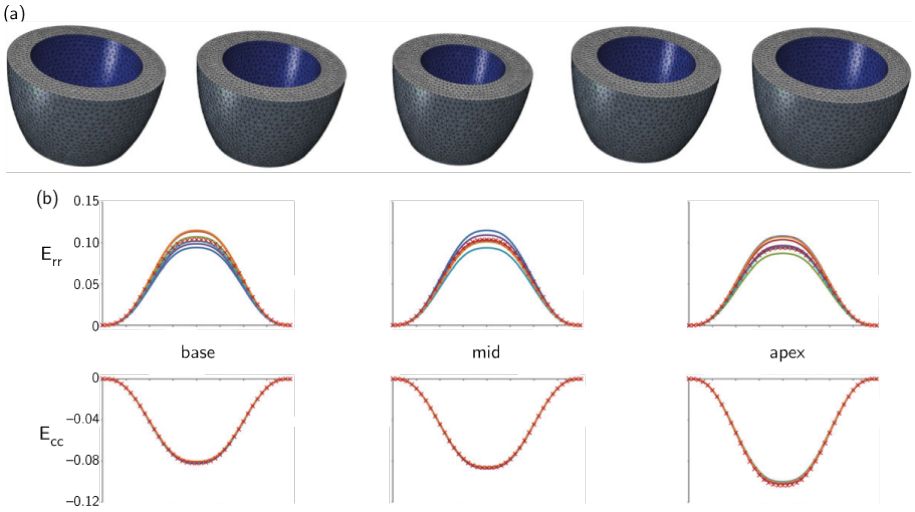

Figure 10.4: Virtual phantom model: (a) phantom ventricle geometry discretized into tetrahedral elements; (b) comparison between the local strains of the virtual phantom computed with our code and the output provided by the finite-element solver. Given the axial-symmetry of the phantom, the finite-element solution consists in a single plot for the basal, mid and apical level of the phantom, respectively. (b) Navy blue, sect1; red, sect2; green, sect3; purple, sect4; sky blue, sect5; orange, sect6; red crosses, FEM.

with EDV and ejection fraction (EF) equal to 130 ml and 72 per cent, and two patients affected by late ischaemic pathology: SUBJECT2 (EDV = 117 ml, EF = 44%, antero-lateral infarction), and SUBJECT3 (EDV = 378 ml, EF = 16%, anterior and inferior-lateral infarction). For each subject, we computed time-dependent basal and apical rotation angles, torsion and regional.

10.3 Results

FAT validation

Of the 15 patients, two were excluded for artifacts in the images that precluded correct performance of the algorithm without heavy manual correction. The semi-automated analysis was then feasible in 13/15 (87%) patients.

The time required to process a single frame (ED or ES) from base to apex, for both endo- and epicardial contours detection, was approximately 1 min using a standard PC. An example of the detected contours for ED and ES frames at three levels of the LV is shown in Fig. 10.5.

Good correlations were found with the reference values for LV EDV ($y = 0.99x+5.1$, $R^2 = 0.99$), and ESV ($y = x+4.34$, $R^2 = 0.99$), as well as with their derived parameters SV ($y = 0.98x - 0.24$, $R^2 = 0.97$) and EF ($y = x + 1.56$,

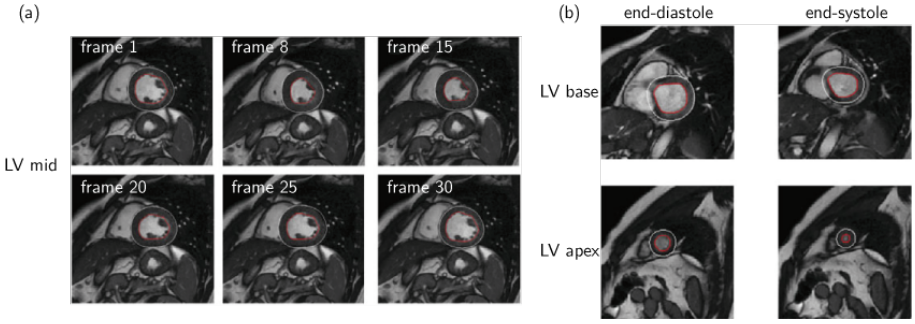

Figure 10.5: Examples of (a) the detected endocardial (in red) and epicardial contours in a slice at mid-ventricular level, in the same frames throughout the cardiac cycle and (b) in a slice at basal and apical levels at end-diastole and end-systole. At basal levels, manual correction was often needed, as shown in this example by the misplacing of the epicardial contour.

$R^2 = 0.98$). For LV mass, a good correlation was found (ED, $y = 1.07x + 5.41$, $R^2 = 0.81$; ES, $y = 0.97x + 12.86$, $R^2 = 0.74$). Bland-Altman analysis resulted in minimal bias and narrow limits of agreement in LV ED and ES volumes, and derived parameters. Conversely, a significant overestimation and wider limits of agreement were found for LV mass. In particular, the bias expressed as $error\%/mean$ of the gold standard values resulted less than 10 per cent in all parameters, except ED LV mass (see Tab. 10.1). Fig. 10.6 visualizes the results obtained in LV volumes and mass, considering ED and ES measurements together.

	Bias	Bias*	95% LOA
EDV	-2.5 ml	-1.4	-17.7÷12.7 ml
ESV	-4.2 ml	-4.1	-15.3÷6.8 ml
SV	1.7 ml	2.1	-7.6÷11.0 ml
EF %	1.5%	3.2	-3.2÷6.2% ml
ED LV Mass	-15.2 g	-11.2	-44.9÷14.6 g
ES LV Mass	-8.7 g	-5.8	-41.3÷23.8 g

Table 10.1: Regression analysis results. EDV, end-diastolic volume; ESV, end-systolic volume; SV, stroke volume; EF, ejection fraction. Bias* = Bias as error%/ mean of the gold standard values.

As regards the automated detection of LV WM, the time needed to process a single slice (30 frames), for endocardial contour detection, and for regional WM analysis, was approximately 1 min. The gold standard interpretation resulted in 135 segments evaluated as normal, and 99 as abnormal.

Fig. 10.2 shows an example of the regional WM curves, as well as the scheme

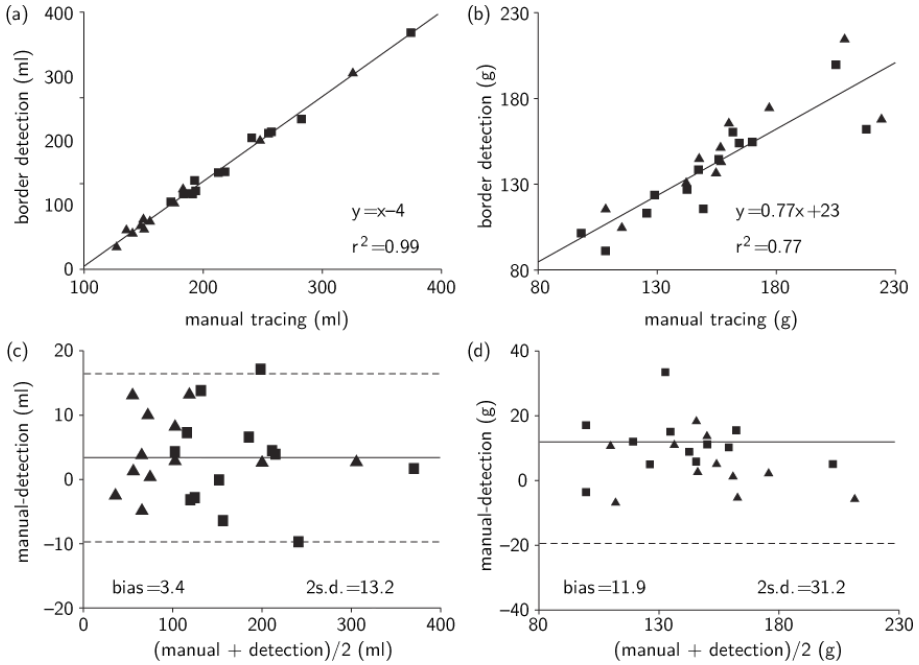

Figure 10.6: Linear correlation and Bland–Altman analysis of the results of (a, c) LV volumes and (b, d) mass (with end-diastolic, squares, and end-systolic, triangles, measurements considered together) obtained by manual tracing of CMR images (gold standard) and through application of the developed endocardial and epicardial border detection algorithm.

used for their quantification. Of the analyzed 234 segments (13 patients $\times$ 6 sectors $\times$ 3 slices), 77 were automatically classified as true positive, 115 as true negative, 20 as false positive and 22 as false negative, based on the selected 50 per cent threshold. These counts resulted in 77.8 per cent sensitivity, 85.1 per cent specificity and 82 per cent accuracy in the automated interpretation of WM.

Left ventricle local strains

Analysis of the virtual phantom. Fig. 10.4 shows the good agreement between the local strains of the virtual phantom computed with our method and the finite-element solution, the maximum difference being equal to 14 per cent.

Analysis of the real ventricles. For normal SUBJECT1, the measured regional strain curves (see Fig. 10.7) provided uniform strain patterns over all myocardial segments; in the systolic phase, all sectors contracted circumferentially and thickened radially. Circumferential shortening increased from the

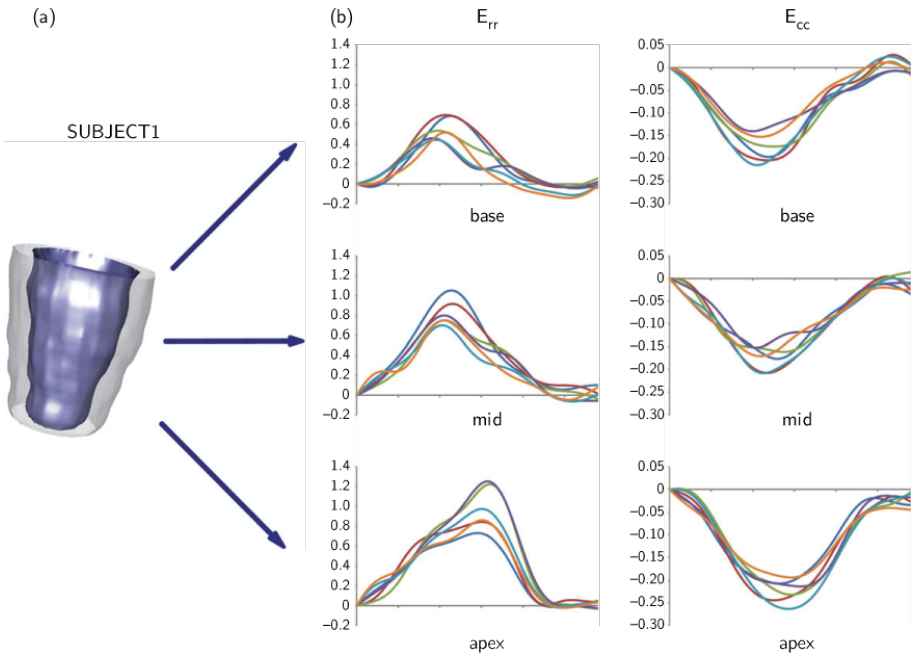

Figure 10.7: Three-dimensional reconstruction of LV endocardial and epicardial surfaces at ED for SUBJECT1. (b) Radial (E_{rr}) and circumferential strain (E_{cc}) curves for the six sectors of the basal, mid and apex regions. (b) Navy blue, sect1; red, sect2; green, sect3; purple, sect4; sky blue, sect5; orange, sect6.

basal region to the apex: peak absolute values ranged from 15 to 21 per cent for the sectors of the basal and mid region, and from 19 to 26 per cent for the apical sectors. Similarly, the observed thickening was progressively more relevant going from the ventricular base to the apex: plots showed maximum values of 51–70%, 69–100% and 72–125% for the sectors in the basal, mid and apical region, respectively. Apical and basal maximal systolic rotations and maximal torsion were 7.8°, 22.8° and 10.2°, respectively (see Fig. 10.9, top panel).

In the pathological subjects, the normal waveform of time-dependent strains, coherence between sectors at the same level, and trends characterizing the changes from the basal to the apical region, were lost.

For SUBJECT2 (see Fig. 10.8, top panel), in the basal region, circumferential shortenings showed a slower dynamics, with maximal values ranging from 12 to 20 per cent. In the mid and apical regions, progressively more irregular patterns and lower maximal values(from 5% to 12% and from 3% to 5%, respectively) were computed. As regards radial thickening, four of the basal sectors showed values from 40 to 80 per cent, whereas much lower values (13% and 22%) were observed in the remaining two sectors. In the mid and apical regions, maximum thickening ranged from 36 to 120 per cent and from 2

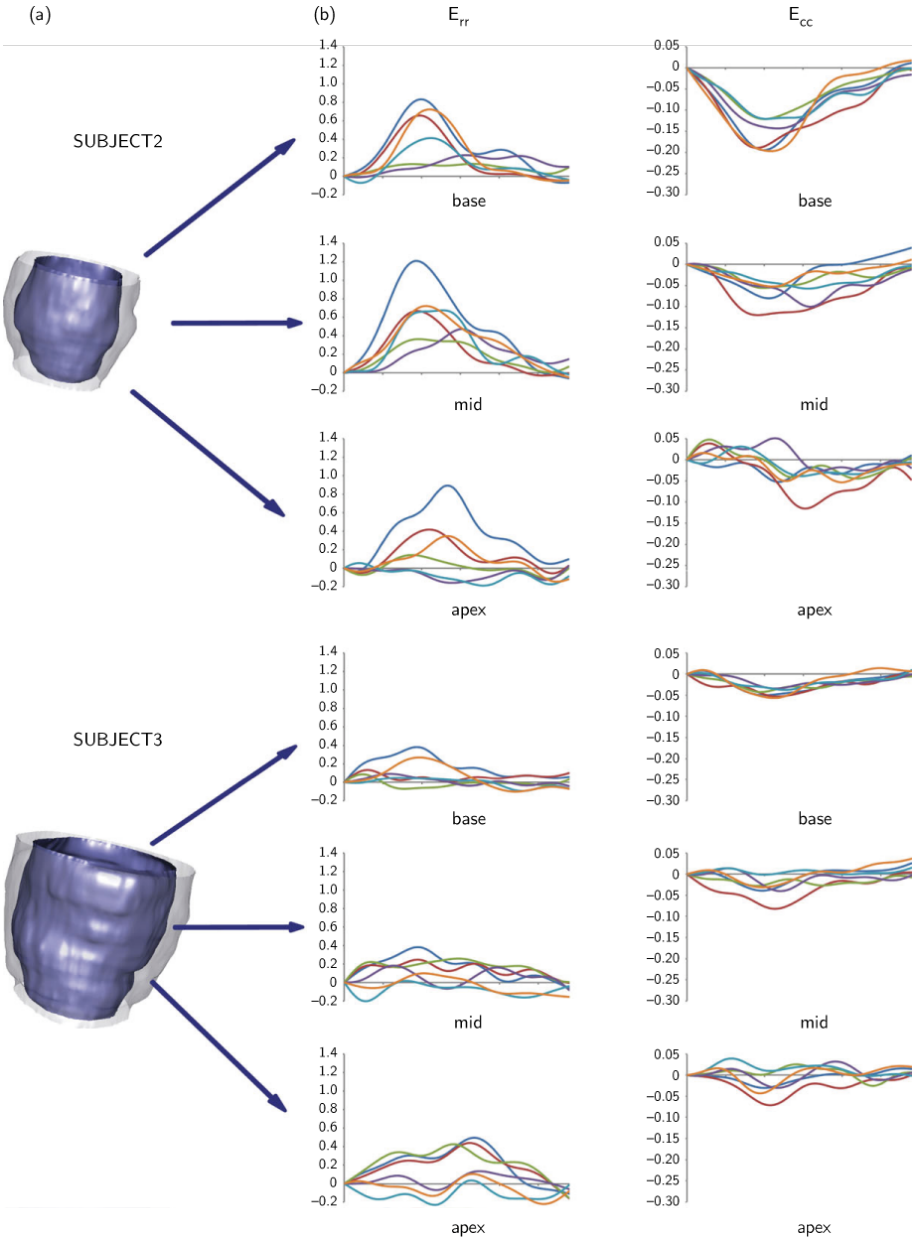

Figure 10.8: (a) Three-dimensional reconstruction of LV endocardial and epicardial surfaces at ED for SUBJECT2 and 3. (b) Radial (E_{rr}) and circumferential strain (E_{cc}) curves for the six sectors of the basal, mid and apex regions.(b) Navy blue, sect1; red, sect2; green, sect3; purple, sect4; sky blue, sect5; orange, sect6.

to 88 per cent, respectively. Apical and basal maximal systolic rotations and maximal torsion were 2.6°, 23.1° and 4.9°, respectively (see Fig. 10.9, mid panel).

SUBJECT3 showed even more abnormal circumferential shortenings and radial thickenings (see Fig. 10.8, bottom panel). None of the 18 sectors shortened by more than 8 per cent, thus indicating very poor contraction of the myocardium. Maximal thickening values ranged from 5 to 38 per cent, from 0 to 38 per cent and from 3 to 50 per cent in the basal, mid and apical sectors, respectively. Moreover, two sectors in the mid and apical regions experienced thinning. Apical and basal maximal systolic rotations and maximal torsion were 1.7°, 20.7° and 2.1°, respectively (see Fig. 10.9, mid panel).

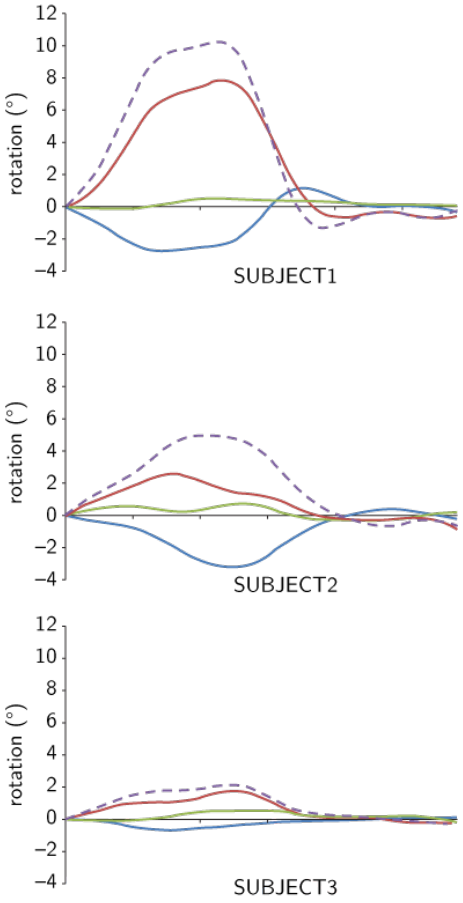

Figure 10.9: LV rotation profiles for SUBJECT 1, 2 and 3. Blue, green and red solid lines indicate basal, mid and apical rotation, respectively. Violet dashed line indicates LV torsion.

For each of the three subjects, the computation of strains, rotation angles and torsion required about 60 min on a standard desktop PC with single CPU

(Intel core2@1.86 Ghz).

10.4 Discussion

In this paper, we presented a new tool for LV analysis from CMR imaging, characterized by two novel aspects when compared with previous approaches [93].

The former consists in the automation of a relevant part of the procedure needed to recognize endocardial and epicardial contours.

The latter consists in the calculation of myocardial local strains through a Lagrangian approach, i.e. by actually tracking different portions of the myocardium in space throughout its deformation process.

In this study, on a small population of subjects, we tested the features of the software that allows for LV endo- and epicardial borders detection for volumetric and WM analysis. Moreover, we tested the capability to correctly compute local LV wall strains on a virtual phantom and applied it to three LVs characterized by different clinical scenarios.

Automated detection of contours for analysis of volumetric and wall motion analysis

CMR imaging provides accurate measurements of LV volumes, EF and mass, nevertheless, the quantification of volumes is based on time-consuming manual tracing of endocardial and epicardial boundaries in multiple slices. The subjective nature of this procedure limits the reproducibility of volume measurements and consequently of the set of derived parameters. The proposed combined automated endocardial and epicardial border detection procedure overcomes these limitations by allowing manual intervention just to optimize the auto- mated detected contours. Despite this advantage, the proposed approach was not completely reliable in several LV basal slices, owing to the presence of the aorta. In this case, manual tracing was performed in order to provide a reliable contour. The technique could be easily applied to all frames in the cardiac cycle, on a different number of slices of fixed thickness for each frame.

Analysis of left ventricle strains and torsion

For validation purposes, we first applied our method for strain estimation on a simplified virtual phantom. The computed strain curves well agreed with the ones yielded by a commercial finite-element solver throughout the whole cardiac cycle, confirming that our method fullfils the minimum requirement of being accurate in presence of simple motion patterns. The application of the

method on three real subjects showed its capability to capture more complex motion and strain patterns.

In the healthy subject, physiologically meaningful strain curves were found: consistently with previous findings [94][95] almost uniform circumferential shortening and increasing thickening were assessed from LV base to apex. Moreover, LV torsion was consistent with data from tagged MRI and Doppler tissue imaging [96], both in terms of time-course and maximal values.

In the ischaemic patients, we found a decrease in peak systolic circumferential and radial strains, in agreement with the expected loss of contraction proper- ties following infarction, as well as in peak systolic torsion, consistently with previous findings [97]. More- over, regional inhomogeneity and dyssynchrony of the strain pattern were detected. These abnormalities were more evident in SUBJECT3, consistently with his much lower EF.

Thus, in these preliminary tests, the calculation of rotations, LV torsion and local strains based on nearest neighbour search appeared able to provide realistic results.

However, the method suffers from some limitations. First, even though the metrics adopted in the nearest neighbour algorithm include a term aimed at enforcing the return of the tracked points to their initial position, computed time-dependent strains showed residual values around 5 per cent at the end of the cardiac cycle. This issue is reported also in other recent studies [98]; possible causes include the natural aperiodicity of LV deformation owing to heart-rate variability, and the inherent limitations of CMR acquisitions.

Second, in order to compute strains within each of the 18 LV wall sectors, we treated each of them as a first-order isoparametric hexahedral element. However, it does not allow for capturing the non-negligible curvature of the endocardial and epicardial surfaces of the sectors. To this aim, we plan to move to the use of higher order elements.

10.5 Conclusion

In the reported preliminary testing, the FAT tool resulted effective in computing LV volumes, myocardial strains and torsion from conventional cine short-axis CMR images. Obtained results were in agreement with manual ground truth values, and with reported literature. Although not fully automated, our method required minimal user interaction, thus improving repeatability. FAT capability in capturing regional functional features may be of use in the interpretation of the remodelling process following myocardial infarction; this information could be useful in the clinical decision-making process and potentially used as input for patient-specific LV modelling tools.

Chapter 11

Automatic Quantification of Cardiac Scar Extent from Late Gadolinium Enhancement Magnetic Resonance Imaging

C. Corsi, **G. Tarroni**, A. Tornani, S. Severi, and C. Lamberti

Computing in Cardiology 2011; 4-7.

Abstract

Purpose. Late gadolinium enhancement cardiac magnetic resonance imaging (LGE-CMRI) is the technique of choice to detect myocardial scars and assess myocardial viability. In clinical practice, this analysis is performed qualitatively or by manually tracing the enhanced area in each acquired slice. The purpose of this study was to test and validate a technique for automated localization and quantification of scar extent.

Methods. CMRI data in patients with previous myocardial infarction were analyzed using custom software from which the myocardium was automatically identified from steady-state free precession images and registered on LGE-CMRI data. Scar tissue was defined as myocardium with signal intensity $\geq$ 80% of its maximum and quantified on each slice. Scar location and extent were assessed and compared with expert analysis.

Conclusions. Preliminary results showed that automatic localization of scar from LGE-CMRI is feasible and scar quantification is accurate and reliable.

11.1 Introduction

As indicated in the ACCF/ACR/AHA/NASCI/SCMR 2010 expert consensus document on cardiovascular magnetic resonance [99], late gadolinium enhancement cardiac magnetic resonance imaging (LGE-CMRI) should be used for identifying the location and extent of myocardial necrosis in individuals suspected of having or diagnosed of chronic or acute ischemic heart disease. This imaging technique provides a noninvasive mechanism to predict recovery of function after revascularization being able to identify sub-endocardial or transmural infarctions. In particular, the presence and the transmurality of scar can be quantified and viable myocardium defined as dysfunctional and non-scarred tissue. Several studies showed the transmural extent of scars predicts the likelihood of recovery of regional function, and when greater than 20% of the myocardium is hibernating, improvement of ejection fraction is likely [100]. LGE-CMRI may also show non-transmural scars that fail to recover function after adequate revascularization. Overall, LGE CMRI has a negative predictive value of ∼90% of no functional recovery in segments with transmural infarction greater than 50% and a positive predictive value of ∼80% of recovery in segments without infarction [100].

In addition, recent studies showed LGE-CMRI may be a valuable tool for predicting major adverse cardiac events and cardiac mortality [101].

In clinical practice, scar assessment is performed qualitatively, or based on time-consuming manual tracing of the enhanced area in each acquired slice [102]. This qualitative analysis can be subjective, which limits direct comparison of results between sequential studies and might hinder its clinical application.

Therefore, the purpose of this study was to test and validate a technique for automated endocardial and epicardial border detection and quantification of scar location and extent.

11.2 Methods

CMR imaging and population

CMRI data were acquired (1.5T, Avanto®, Siemens Healthcare, Erlangen, Germany) at the Southampton University Hospital NHS Trust, UK, in 5 patients (3 males; age 59 ± 19 years) with previous myocardial infarction.

Scout images were acquired first, for identification of the cardiac axes. Dynamic image loops were then acquired perpendicular to the LV long-axis in contiguous slices from the mitral valve to the LV apex using a steady-state free precession (SSFP) imaging protocol (TR = 30 ms, TE = 1.1 ms, flip angle: 70°, slice thickness = 6 mm, spacing between slices = 10 mm, initial matrix

size: 192×156 pixel). Temporal resolution was 20 frames per cardiac cycle.

LGE-CMRI data was acquired after Gadolinium injection (TR = 700 ms, TE = 1.4 ms, IT = 220 ms, flip angle: 10°, slice thickness = 4 mm, no gap, initial matrix size: 256×200 pixel).

Image analysis

Custom software based on image noise distribution (for endocardial detection) and image gradient (for epicardial detection) was applied; the myocardium was automatically detected from SSFP images, and registered on LGE-CMRI data.

The first step of the analysis is the manual selection of one point inside the LV cavity followed by the application of a fast region-based global segmentation of the most apical slice of the end diastolic (ED) frame on the SSFP sequence (see Fig. 11.1, A). This global segmentation allows partitioning the acquired slice into maximally homogeneous regions taking into account the local noise patterns [66] (see Fig. 11.1, B). The final result (see Fig. 11.1, C) is limited to the region of interest around the initial point (see Fig. 11.1, D) and used as initial condition for a local segmentation obtained applying the same statistical model (see Fig. 11.1, E). Endocardial detection is refined by applying a boundary regularization achieved using curvature motion [103] that does not allow curvature above certain level and was designed to automatically include the papillary muscles in the LV cavity (see Fig. 11.1, E).

Figure 11.1: Endocardial segmentation: a point is selected inside the LV cavity in the most apical slice of the ED frame (A); global segmentation is performed (B) then the final zero level set (C) is limited to the region of interest around the initial point (D) and used as initial condition for the endocardium detection achieved in two steps: local statistical level set (E, white contour) and the edge-based level set (E, green contour).

To identify the epicardial boundary we then used the classical edge-based level-set model [57] to search the image from the endocardium outwards. The equation that drives the evolution is the well-known Malladi-Sethian model for active contour evolution including a dependence of the speed on the curvature, a propagation expansion speed and an advection speed based on the image gradient. At the end of this step, the epicardium boundary is also regularized with a modified curvature motion (see Fig. 11.2).

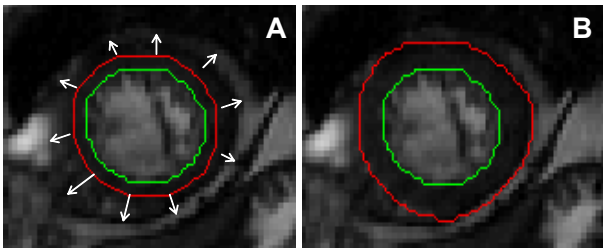

Figure 11.2: Final epicardial segmentation (B) obtained applying the classical edge-based level-set model to search the image from the endocardium outwards (A).

To obtain the segmentation of a frame, endo and epicardial segmentation was automatically repeated on each slice using as initial condition the centre of mass of the endocardial contour of the previous slice. For the segmentation of the next frames, the previously manually selected initial point was used and its position optimized considering the gray levels of the image.

The detected surface corresponding to the instant of time in which LGE CMRI data was acquired, is then registered on the LGE-CMRI data, considering the different acquisition parameters (see Fig. 11.3).

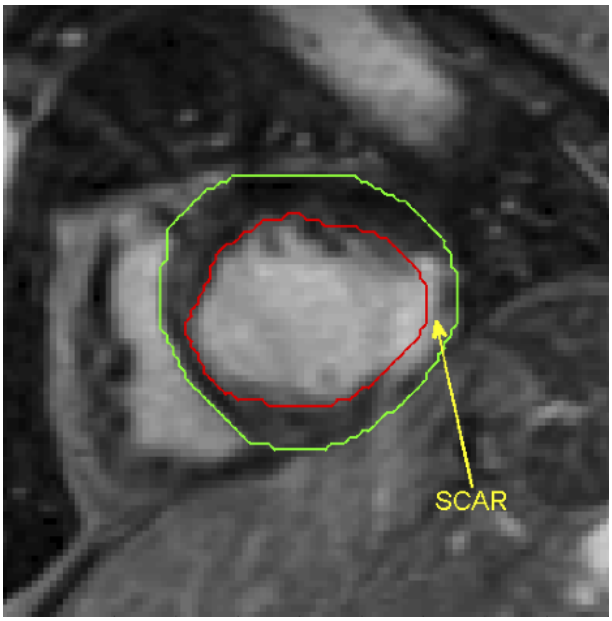

Figure 11.3: Example of scar detection in one slice of the LGE-CMRI data.

The tissue inside myocardium was studied and scar tissue defined as myocardium with signal intensity $\geq 80\%$ of its maximum and quantified on each slice.

An expert cardiologist provided the "gold standard" for scar location and extent on each acquired slice of the LGE-CMRI acquisition.

Scar location was assessed according to the standard segmentation model and compared with expert analysis; comparison of scar extent with "gold standard" was performed by linear regression and Bland-Altman analyses.

11.3 Results

Time required for automated analysis in one slice was only few seconds, for a total of 5-6 minutes for scar localization and quantification on a standard PC.

An example of the detected contours in one frame is shown in Fig. 11.4, together with the corresponding 3D reconstruction.

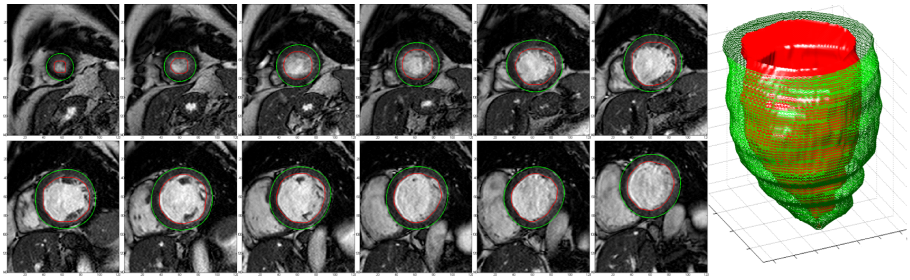

Figure 11.4: Endocardial and epicardial contours obtained in one frame from apex (top left) to base (bottom right) together with the corresponding 3D surface reconstruction.

Endo- and epicardial boundaries were judged accurate in all image sequences. Examples of the automatically detected contours (right panels) and the corresponding manually traced ones (left panels) are shown in Fig. 11.5.

Cardiologist detected 7 scars (4 mid antero-septal; 2 mid and apical lateral, 1 apical posterior) for a total of 73 slices. Automated analysis evidenced 7 scars and located them in the correct position.

An example of a detected scar in one patient in the lateral segment is shown in Fig. 11.6.

A very good correlation (R = 0.96, y = x + 0.06), non-significant bias (0.07 cm^2, 2.5% of the mean reference value) and narrow limits of agreement (0.61 cm^2) were found between scar area extent manually and automatically quantified. An example of the manually traced scar (left) and the automatically detected one (right) in one slice, in two patients, is reported in Fig. 11.7.

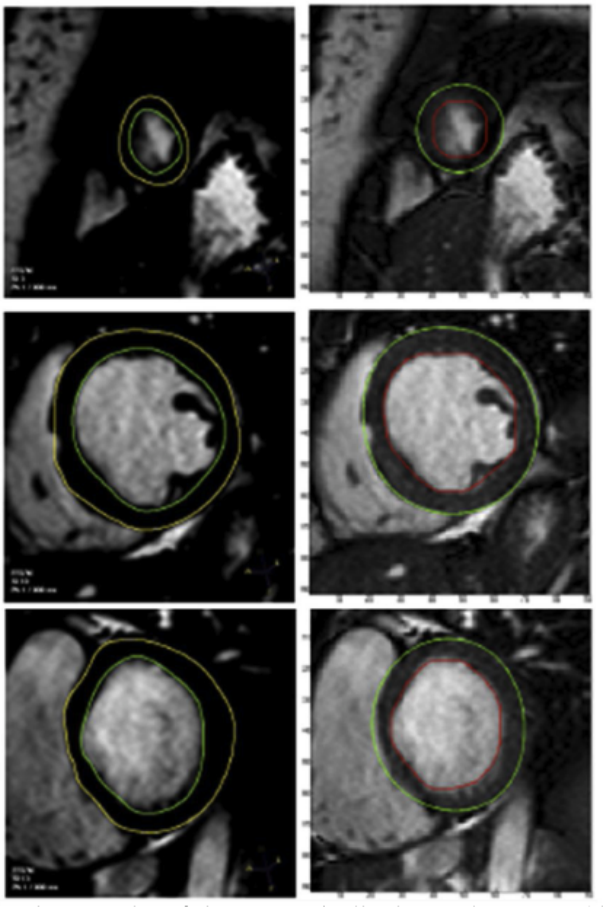

Figure 11.5: Examples of the automatically detected contours (right panels) and the corresponding manually traced ones (left panels).

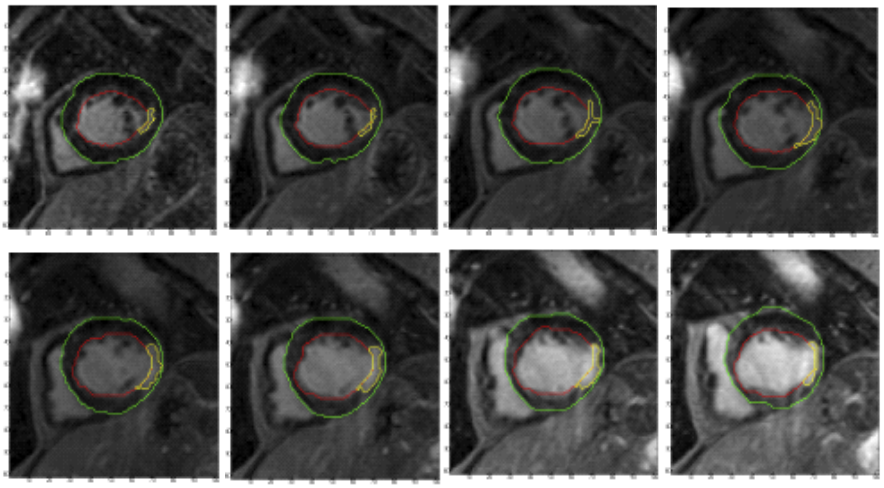

Figure 11.6: Example of scar detection from LGE-CMRI data in one patient: in red the endocardium, in green the epicardium and in yellow the detected scar.

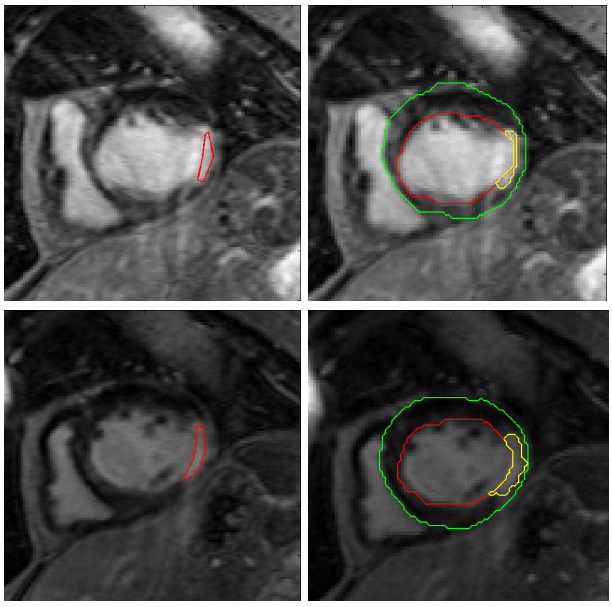

Figure 11.7: Comparison between scar contours manually traced (left) and automatically detected (right) in two slices belonging to two patients.

11.4 Discussion

In this study, we have presented a quantitative technique for segmenting myocardial scar in LGE-CMRI images, using myocardium information derived from SSFP data. We have applied this technique to images exhibiting visually distinct patterns of myocardial scar. A clear correspondence between the extent of myocardial hyper enhancement automatically quantified in LGE-CMRI images and the manually traced extent of myocardial scarring has been found.

Time required for the automated scar quantification could be further speeded up performing the analysis directly in the 3D space. Considering this improvement and following a comprehensive validation, this method could be suitable for clinical implementation. Importantly, the results of this analysis involve not only scar location and extent but also ventricular function being available dynamic endocardial and epicardial surfaces from which volumes, stroke volume, ejection fraction, mass, systolic and diastolic parameters could be easily derived and quantified.

Part III

Unrelated Projects

Chapter 12

Prosthetic Component Segmentation with Blur Compensation: a Fast Method for 3D Fluoroscopy

G. Tarroni, L. Tersi, C. Corsi, and R. Stagni

Medical & Biological Engineering & Computing in Press.

Abstract

Purpose. A new method for prosthetic component segmentation from fluoroscopic images is presented.

Methods. The hybrid approach we propose combines diffusion filtering, region growing and level set techniques without exploiting any a-priori knowledge of the analyzed geometry. The method was evaluated on a synthetic dataset including 270 images of knee and hip prosthesis merged to real fluoroscopic data simulating different conditions of blurring and illumination gradient. The performance of the method was assessed by comparing estimated contours to references using different metrics.

Results. Results showed that the segmentation procedure is fast, accurate, independent on the operator as well as on the specific geometrical characteristics of the prosthetic component, and able to compensate for amount of blurring and illumination gradient. Importantly, the method allows a strong reduction of required user interaction time when compared to traditional segmentation techniques.

Conclusions. Its effectiveness and robustness in different image conditions, together with simplicity and fast implementation, make this prosthetic component segmentation procedure promising and suitable for multiple clinical applications including assessment of *in vivo* joint kinematics in a variety of cases.

12.1 Introduction

3D video-fluoroscopy (3DF) was proven to be a reliable and accurate method to study *in vivo* joint kinematics [104][105][106][107]. This technique is aimed at reconstructing the 3D pose of objects of known 3D geometry from one or more 2D fluoroscopic projections. Different algorithms have been proposed for this estimation [104][108][109], but the appropriate segmentation of the target object in the 2D image is always a critical step [110][111]. The identification of the external contours of the object in the 2D projection drives the 3D alignment; additional internal and/or spurious contours can affect the final estimation of the 3D pose (e.g. introducing local minima, altering the sensitivity of the alignment algorithm).

For the segmentation of the 2D contour to be exploited for 3DF alignment, simple thresholding [104][112] or Canny edge detector [113] are typically applied to the whole image or to a smaller region of interest [104][114][115]. These methods rely on threshold values and the obtained results are usually not optimal. Consequently, a time consuming manual procedure is needed to delete the undesired contours belonging to other anatomical structures. This makes the segmentation procedure cumbersome and strongly operator dependent, thus hindering the application of 3DF for routine clinical functional assessment of human joints. Accordingly, an automated and reliable method for 2D fluoroscopic images segmentation could significantly improve the robustness of 3DF procedure and its applicability in the clinical practice.

The design of an automated segmentation technique has been hampered by several disturbing phenomena affecting fluoroscopic images: 1) quantum noise [116], 2) illumination gradient or vignetting, 3) presence of dark cemented regions close to prosthesis border, 4) cluttering of other prosthetic components or of the contralateral limb, and 5) image blurring, mainly affecting the contours orthogonal to the direction of motion of the acquired anatomical structure. Different segmentation methods are reported in literature. Domokos *et al.* [117] proposed a template matching method for radiographic hip prosthesis segmentation. However, the performance of the method was affected by the presence of illumination gradient. Varshney *et al.* [118] proposed a method based on a level-set implementation for multi-view segmentation to recover the 3D shape of bones and prostheses in postoperative joints. The performance of the method was promising, but strongly dependent on the number of input projections. Moreover, a good estimate of the general shape was obtained, but large errors could still occur locally, especially at sharp edges. Accordingly, the design of an automatic segmentation procedure should overcome the limitations of these methods, allowing the accurate extraction of prostheses boundaries.

In addition, albeit translational motion blur is a very common type of image distortion in 3DF and can negatively affect the segmentation result [119],

its detection and compensation to improve prostheses segmentation has not been deeply analyzed so far in this context. Therefore, a robust segmentation technique should also address this issue.

Traditional semi-automatic methods such as active contours [120], level-set [57] or region growing [121], when used alone, are unable to generate optimal results. On the other hand, a hybrid approach, combining the strong points of these methods without exploiting any a-priori knowledge of the analyzed geometry, can be used to develop a robust segmentation procedure to be applied in 3DF dynamic conditions, reducing user interaction.

The aim of the present work is to present a hybrid approach for the segmentation of fluoroscopic images of prosthetic components and to test its performance on both *in silico* and *in vivo* images. The proposed method is meant to make the segmentation procedure fast, robust (limiting operator dependency) and accurate (addressing the different sources of error), being independent on the specific geometrical characteristics of the prosthetic component and compensating for translational blurring.

12.2 Methods

Segmentation Method

The design criteria of the proposed hybrid approach were the following ones: velocity (reduced user interaction time), specificity (efficient discrimination between prosthesis edge and cemented parts or high density bony tissue), robustness (ability to deal with blurred images, low contrast and illumination gradient, independently from the operator), flexibility (applicability to different prosthetic models), accuracy (ability to detect contour points which are less likely to be part of the prosthesis boundary). The proposed technique consists of the following steps:

A. **Seeding:** a manual seeding is performed, choosing an internal point approximately at the center of the prosthesis component (see Fig. 12.1, Panel a). The image is then automatically cropped to a square, the side of which is a power of 2 pixels wide (S_{crop}). This was necessary for the following region growing operation;

B. **Diffusion filtering:** to reduce the effect of Poisson quantum noise [116] and illumination gradient typical of fluoroscopic images, an edge preserving anisotropic diffusion filter was designed and applied to the image [120] (see

Fig. 12.1, Panel b):

$$\begin{cases} I_t = g\kappa|\nabla I| + \nabla g \cdot \nabla I, & \text{in } \Omega \times (0,\infty) \\ \dfrac{\partial I}{\partial n} = 0, & \text{in } \partial\Omega \times (0,\infty) \\ I(0) = I_0, & \text{in } \Omega \end{cases} \tag{12.1}$$

where I is the image, Ω is the image domain, κ is the Euclidean curvature, g is the well-known edge indicator introduced by Perona and Malik [61]. The diffusion is weighted by the edge indicator g: it is fast in the low gradient areas, and it slows down and stops in correspondence of the edges. Equation 12.1 was approximated applying a finite-difference scheme and solved iteratively for at least a minimum number of steps (N_{filt}). The exit condition is reached when the relative variation of the mean of the difference between images during the filtering iterations is less than T_{filt};

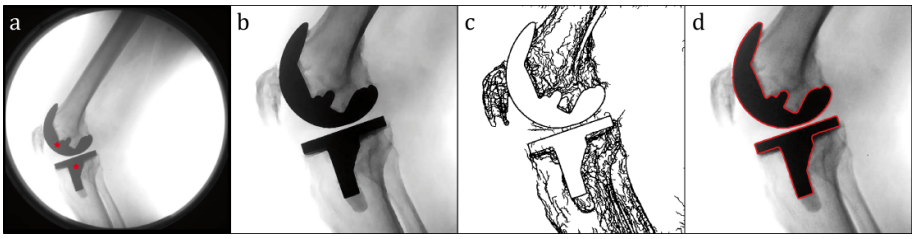

Figure 12.1: Segmentation technique (steps A to E). a) Initial image with seed points (stars) manually positioned; b) Image after cropping and anisotropic filtering; c) Image's edge indicator after thresholding; d) Contour obtained by region growing followed by Malladi-Sethian level-set algorithm.

C. **Binary masking:** a binary mask (g_{mask}) is computed thresholding the edge indicator g applied to the filtered image. This operation is carried out in order to obtain a uniform and closed white region inside the prosthesis area:

$$g_{i,j}^{mask} = \begin{cases} 0, & g_{i,j} < T \cdot g_{max} \\ 1, & g_{i,j} \geq T \cdot g_{max} \end{cases} \qquad \text{with } T \in \{0,1\} \tag{12.2}$$

$$g_{max} = \max_{i,j} g_{i,j} \qquad \text{with } i,j \in \Omega \tag{12.3}$$

with $T = 0.9$. To refine the spurious contours inside the prosthesis area a fill-holes procedure is finally applied to g_{mask}. The result of this step is a binary image, white in the uniform gray level area, and black in proximity of the edges (see Fig. 12.1, Panel c);

D. **Region growing:** the resulting image is elaborated with a region growing algorithm [121]. In the present implementation, the process starts from

the seed point specified at step A. To prevent eventual overflow outside the prosthesis region, an 8-connected neighborhood criteria was used for the classification. The result is a binary image, white inside the seeded prosthesis, and black outside. The contour is extrapolated as an iso-curve between black and white pixels. This contour is usually a closed and shrunk version of the actual prosthesis contour. In case that the final contour is not closed, the user can easily repeat step C and D manually modifying the threshold T;

E. **Contour refining:** a refining operation is carried out with a Malladi-Sethian level-set algorithm [57], based on equation 12.1, in which the implicit surface to be evolved is a distance function of the contour points (see Fig. 12.1, Panel d). The metric of the evolution is weighted by the edge indicator g applied to the original image I. The procedure is iterated, and automatically stopped when the area inside the contour does not change of more than a fixed number of pixels (N_{px}), experimentally determined, between two following iterations.

   In case of image blurring, the computed contour (MS-C) is more likely to underestimate the real one, remaining in the inside of the prosthesis;

F. **Blur detection & compensation:** the level-set contour obtained in the previous step undergoes an advection motion driven by a synthetic field $M = (M_x, M_y)$ defined as follows:

$$\begin{cases} M_x = s\cos\theta \\ M_y = s\sin\theta \end{cases} \tag{12.4}$$

$$s = sign\big[(G_x\cos\theta) + (G_y\sin\theta)\big] \tag{12.5}$$

   where G_x and G_y are the components of the gradient of the level-set function, and θ is an angle varying with a defined step in the range 0°-160°. For each value of θ, the advection motion performs a directional stretching of the previously computed contour (see Fig. 12.2, Panel a), leaving undeformed the portions orthogonal to the field and preserving the overall shape details (see Fig. 12.2, Panel b). This motion is carried on for a limited amount of iterations, in order to achieve a deformation roughly 2-pixel-wide per side, which is enough to detect even a very small blurring. The variance of pixel intensity gives a simple estimate of the presence of blur [122]. Accordingly, for each deformation direction, the variance of pixel intensity between the original contour and the deformed one is calculated. The deformation direction with the minimal variance is the one in which blurring is more likely to have occurred; the corresponding angle is labeled

θ_B. For blur compensation, the contour computed at step E undergoes an advection motion in the direction defined by θ_B. At each deformation step of two-pixel-width, the surface between the present contour and the one at the previous step is defined as Σ. The mean pixel intensity of the portion of g included in Σ is calculated at each step: the exit condition is reached when the mean pixel intensity at a certain step exceeds the one at the previous step by at least 10%. This is assumed as the outer blur contour (OB-C) (see Fig. 12.2, Panel c). The final contour of the prosthesis is defined as the curve equidistant from OB-C and MS-C (see Fig. 12.2, Panel d). In absence of blur, the exit condition is reached at the first deformation step, thus the final contour coincides with MS-C,

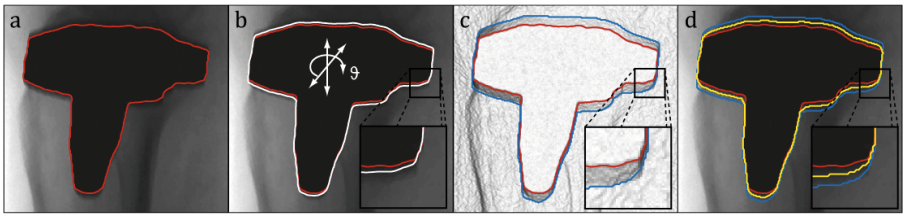

Figure 12.2: Blur detection and compensation (step F). a) Contour as obtained at step E; b) Blur direction extraction obtained deforming iteratively the initial contour (red) in different directions (white); c) Image's edge indicator used for the estimate of blurred area size (blue contour) performed deforming the initial contour (red) in the previously extracted direction; d) Prosthesis final contour (yellow) obtained as central line between the blue and red contours.

G. **Unreliable contour point suppression:** since the final usefulness of prosthesis segmentation is towards 3D alignment, and given the robustness of 3D/2D registration algorithms, few reliable contour points are preferred to many less reliable ones. Therefore, contour point suppression was implemented to improve contour accuracy. To this end, the gradient ($grad(I)$) of the image is computed and convolved with a smoothing Gaussian function, obtaining $grad^S(I)$. 5% of the points of the contour is suppressed, choosing those with the lowest value of the corresponding pixel in $grad^S(I)$. Then, any additional point of the contour is suppressed if the value of the corresponding pixel in $grad^S(I)$ is lower than a certain threshold (T_s).

Of note, the segmentation up to step F always generates closed contours, while step G always generates open contours.

The operator intervention is required at step A, in the seeding of a point internal to the prosthesis component, and potentially at step C, to modify the threshold T.

Synthetic Image Dataset

The dataset was composed of 1024×1024 images coded with 4096 gray levels in the range [0-1], corresponding to standard fluoroscopic images.

Projections of CAD models of knee (femoral and tibial components) and hip prosthesis femoral components (data from Simtk Grand challenge competition [123]) were generated, virtually aligning the geometric models over real fluoroscopic images of intact joints.

Based on Lambert-Beer law, DRRs [124] were generated and fused with the real images simulating different conditions of blurring and illumination gradient. The fusion was carried out using the following procedure: 1) the model was positioned in 10 physiological poses aligned to the underlying image; 2) flat shaded binary projections were generated. The iso-lines at the edge between black and white pixels were extracted and used as reference contours; 3) binary images were then blurred in a random direction, with blur amplitude of 0, 5 and 10 pixels; 4) Poisson quantum noise was added to the image according to Chan *et al.* [116]; 5) a radial illumination gradient was added to the image simulating the vignetting effect; the intensity of the gradient was varied considering three levels corresponding to 0, 5 and 10% of the real image gray level range; 6) the resulting image was finally merged to the real fluoroscopic image to simulate the texture caused by soft tissues. The resulting dataset included 270 perturbed images.

Performance Evaluation

The proposed hybrid segmentation procedure was applied to the synthetic image dataset. The influence of illumination gradient, blur correction and prosthesis component geometry on the final segmentation was analyzed.

All segmentations were performed setting the following values:
Step A) $S_{crop} = 512$ px; Step B) $N_{filt} = 50$, $T_{filt} = 1\%$; Step E) $N_{px} = 4$; Step F) θ in [0° - 160°] with step 20°; Step G) $T_s = 0.002$.

In order to evaluate the robustness of the procedure, one experienced and three un-experienced operators performed the segmentation, and one of the un-experienced operators repeated the segmentation procedure 3 times.

The performance of the segmentation procedure up to step F (closed contours) was evaluated computing the following parameters:

I. the Area Ratio coefficient A_r

$$A_r(R, E) = \frac{\Gamma_E}{\Gamma_R} \tag{12.6}$$

where Γ_R and Γ_E are the areas inside the reference contour R and estimated contour E, respectively. This parameter allows to quantify whether the area in E is smaller or larger than the area in R;

II. the Mean Absolute Deviation (MAD) [69]

$$MAD(R,E) = \frac{1}{2}\left[\frac{1}{N_r}\sum_{r\in R} d(r,E) + \frac{1}{N_e}\sum_{e\in E} d(e,R)\right] \tag{12.7}$$

where N_r and N_e are the number of points of the contours R and E respectively, and d is the Euclidean distance. This parameter allows to quantify the average error between contours;

III. the Hausdorff distance (H) [125]

$$H(R,E) = \max\{H_{re}, H_{er}\} \tag{12.8}$$

where H_{re} and H_{er} are the maximum of the minimum Euclidean distance between the single point $r \in R$ or $e \in E$ and the set of points of E or R, respectively (see Fig. 12.3, left). This parameter is a linear measurement of the maximum discrepancy among the contours and constitutes the error upper limit.

The performance of the segmentation procedure after step G (open contours) was evaluated computing the following parameters which take into account only the distances between the single point $e \in E$ and the set of points of R:

I. the Open Hausdorff distance (see Fig. 12.3, right)

$$oH(R,E) = H_{er} \tag{12.9}$$

II. the Open Mean Absolute Deviation (oMAD)

$$oMAD(R,E) = \frac{1}{N_e}\sum_{e\in E} d(e,R) \tag{12.10}$$

The Kolmogorov-Smirnov test was used to investigate whether the parameter distributions were normal.

Kruskal-Wallis tests were performed ($\alpha = 0.05$) to evaluate the influence on the estimated parameters of illumination gradient, blur amplitude, prosthesis model, as well as inter- and intra-operator intervention. Then, Mann-Whitney U test with Bonferroni correction was performed to ascertain possible between-group significant differences among the groups themselves. Finally, the Mann-Whitney U test ($\alpha = 0.05$) was performed to estimate the effect of blur compensation (step F) and unreliable contour point suppression (step G). All statistical analyses were performed with NCSS®(NCSS, Kaysville, Utah, US).

In order to verify the feasibility of applying the segmentation procedure (comprised of the blur compensation algorithm) to *in vivo* 3DF prosthesis

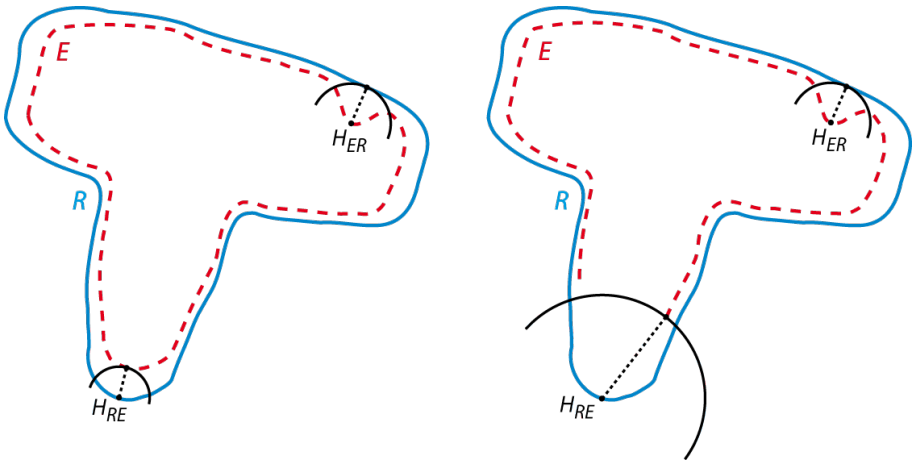

Figure 12.3: Outline of the Hausdorff distance for closed (left) and open (right) curves. H_{re} is not a suitable measure of the distance between open curves because it overestimates the actual distance.

datasets, images of a prosthetic knee of one subject performing a step up/down (30) task were analyzed using the same internal parameters of the *in silico* evaluations. Segmentation results and analysis time were qualitatively compared to the ones obtained using the standard approach based on Canny edge detector followed by manual contour suppression, which is needed to exclude detected spurious contours not belonging to the prosthesis.

12.3 Results

Custom software for segmentation was implemented in MATLAB®(MathWorks, Natick, Massachussetts, US).

The computational time was ∼25 s per image (Intel Core i7-2720QM 2.20 GHz, RAM 8.00 GB), of which ∼10 s for seeding (step A) and thresholding (step C-D), ∼10 s for diffusion filtering (step B), ∼2-3 s for contour refining (step E) and ∼1-2 s for blur detection and compensation (step F). Code parallelization was implemented and tested on 4 cores, allowing a reduction of the computational time for steps B, E, F, which required 4 s overall. The proposed method could efficiently segment prosthesis components, preserving sharp and round edges, and compensate for image blur. Some examples are shown in Fig. 12.4.

The Kolmogorov-Smirnov test showed that the parameters were not normally distributed ($p > 0.1$).

The illumination gradient did not result in any significant difference in values of parameters A_r, MAD and H. Thus, the performance of the segmentation method was independent from the illumination gradient.

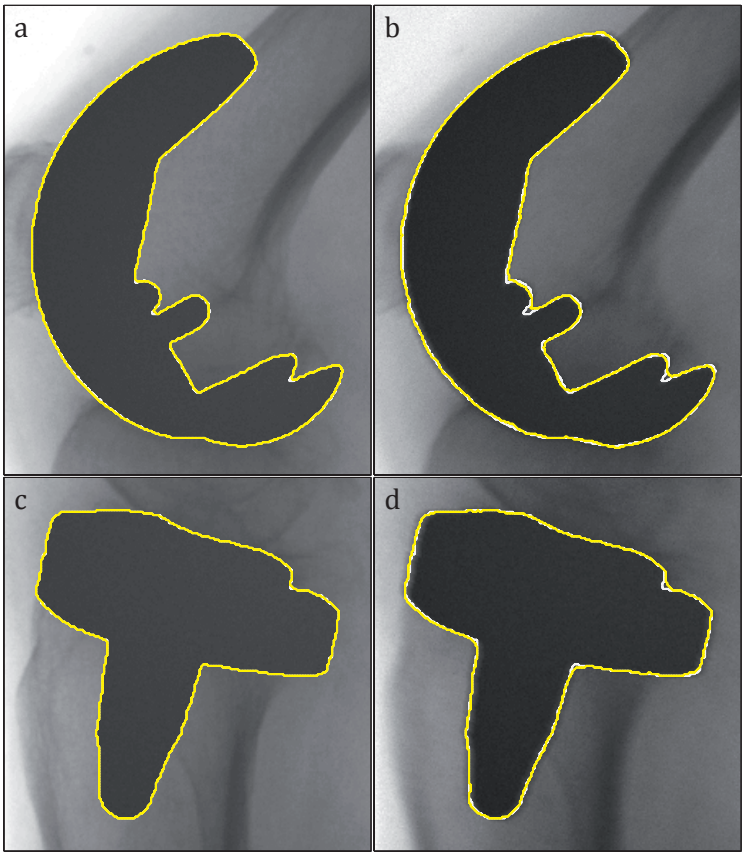

Figure 12.4: Examples showing the reference contour (white) and the automatically computed one (yellow). a) Femoral component without blur; b) Femoral component with blur = 10 px; c) Tibial component without blur; d) Tibial component with blur = 10 px. In all images the illumination gradient was 10%.

Before blur detection and compensation (steps A-E), the amplitude of blur superimposed to the image was inversely proportional to A_r and directly proportional to MAD and H. Blur correction (step F) always significantly improved A_r, MAD and H. In particular, it halved the value of MAD for any blur amplitude, and drove the value of A_r closer to 1. These trends were consistent for different prosthesis components. Quantitative representation of the statistical relationships among parameters, blur, blur compensation, and prosthesis component is reported in Fig. 12.5.

The Kruskal-Wallis test highlighted no significant difference among inter- and intra-operator intervention, supporting the robustness of the procedure.

The unreliable contour point suppression (step G) produced a systematic and significant (max $p < 0.001$) reduction of $oMAD$ and oH in any operative

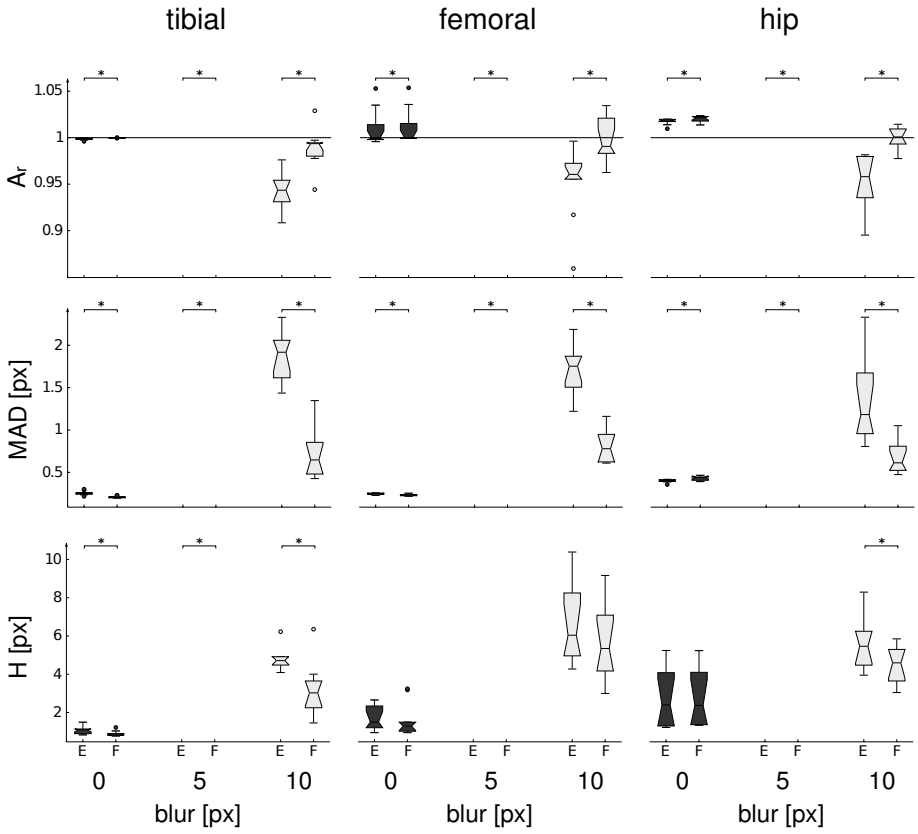

Figure 12.5: Box and whisker plot of the Area Ratio (A_r), Mean Absolute Deviation (MAD), and Hausdorff distance (H) without (step E) and with (step F) blur detection and compensation with respect to different levels of blur and different prosthesis models obtained by one un-experienced operator. The Kolmogorov-Smirnov test highlighted that blur decreased the accuracy of the segmentation (increasing H and MAD) with a smaller area with respect to the reference contour ($A_r < 1$). Blur correction and compensation significantly reduced this effect (* Mann-Whitney U-test, $p < 0.01$).

condition, according to Mann-Whitney U test.

Preliminary results on the *in vivo* dataset demonstrated that, even without tweaking the internal parameters, the proposed segmentation algorithm managed to analyze real fluoroscopic images. Both our method and the Canny edge detector showed a good sensitivity to the prostheses contour also with blurred images, although better results were obtained with the automated method especially in cemented parts. In terms of specificity, the proposed technique outclassed the Canny edge detector, always managing to avoid the detection of bony and soft tissues' boundaries. The analysis time for our method was ∼25 s per image as for *in silico* analysis, while for the Canny edge detector a trial and error approach was necessary to tune the needed parameters balancing sensitivity and specificity, and a long manual selection procedure was needed to exclude the remaining wrong contours, resulting in ∼1-2 min of user interaction per image. As an example, Fig. 12.6 shows the segmentation results of both our segmentation algorithm and the Canny edge detector before and after the wrong contours suppression.

12.4 Discussion

The appropriate segmentation of prosthetic components in the 2D fluoroscopic images is a critical step [110] in the implementation of 3DF for the accurate 3D kinematics of human joints. Mahfouz *et al.* [126] proposed a contour matching method not requiring manual contour suppression; however, information related to spurious contours interferes with a proper alignment. Therefore, other contour based approaches [104][114] imply a time-consuming and operator-dependent segmentation procedure, hindering the application of 3DF for routine clinical functional assessment of human joints.

In order to overcome this limitation, and to improve the robustness of 3DF procedure and its applicability in the clinical practice, a promising method for automatic prosthesis segmentation from 3DF data was designed and implemented.

In a work by Oprea *et al.* [127], the prosthesis segmentation performance of classical adaptive region segmentation approaches (Fuzzy C-means) resulted in 2-11% classification errors, unfitted to the 3DF context. On the other side, the level-set approach proposed by Varshney *et al.* [118] was proven to be efficient for 3D prostheses segmentation. However, this approach, purely based on level-set, might fail in accurately detecting the prostheses' sharp edges which are fundamental for a proper 3DF pose estimation.

To fully exploit the level-set potentialities and to provide a blur compensation method, in the present work the level-set approach was combined to anisotropic diffusion filtering and region growing. The diffusion filtering step

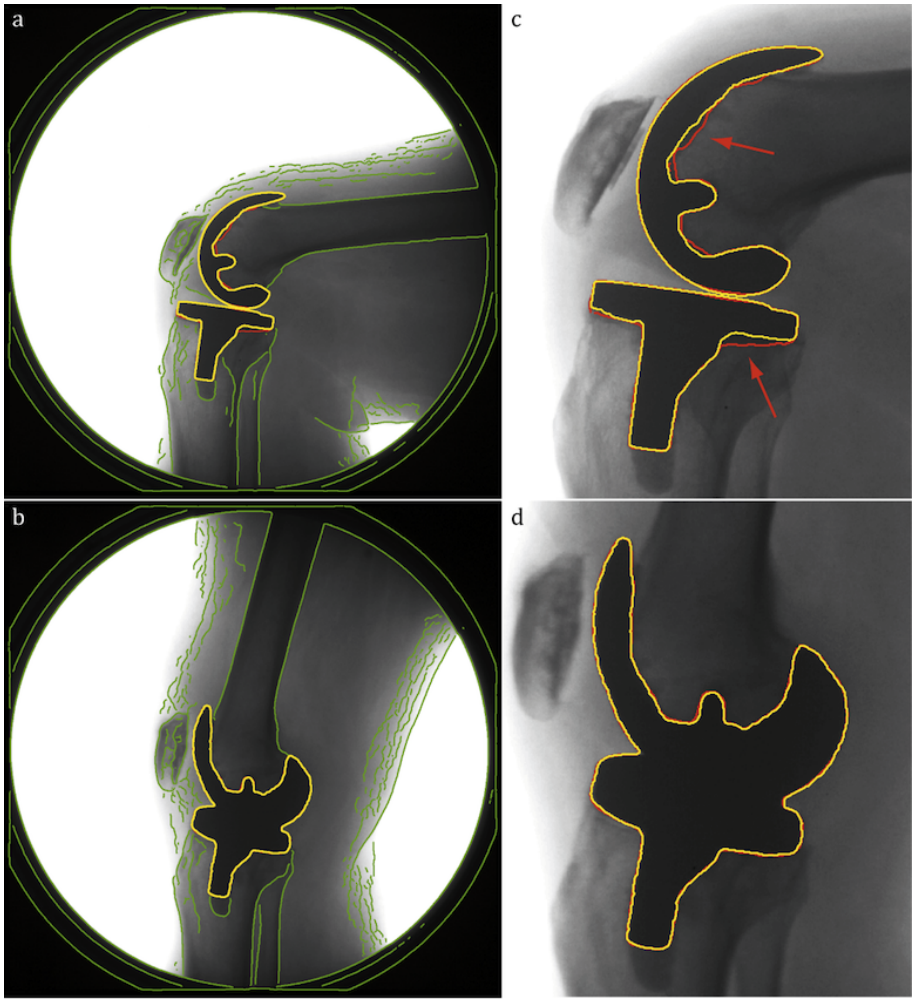

Figure 12.6: *in vivo* examples showing the application of both the proposed technique and Canny edge-detector presented both in the full frame (a and b) and cropped (c and d, respectively). The yellow contour represents the result of the automated technique, while the green and red ones show the results of the Canny filter before and after manual contour suppression, respectively. The red arrows point at cemented and blurred areas, in which the proposed technique outperforms the Canny edge-detector.

produces a homogenization of the gray levels of the image without altering the edges (which are therefore reinforced). This allows an initial compensation for illumination gradient and noise. To achieve a fast and conservative initial segmentation of the prosthesis, thresholding and region growing steps have been implemented. Then, a Malladi-Sethian level-set refinement step allows local expansion of the computed boundary so to compensate for remaining noise and artifacts. The reason to use a region growing step coupled with a level-set approach (rather than the latter alone) is twofold: firstly, due to the big size of typical fluoroscopic images, the level-set approach alone would require too much time to find the desired contour; secondly, since it is starting its evolution close to the final boundary, the Malladi-Sethian model can be tuned to force mild motion, which allows to detect edges even in case of low image contrast. The following fast and fully automated step regarding blur detection succeeds in compensating for motion blur when it is present, preserving the computed contour otherwise.

Blur has been deeply studied in image processing, and many different approaches have been previously proposed to measure the amount of blurring of an image [128][129][130]. However, to the best of our knowledge, none of these methods has ever been explicitly applied to prosthetic component segmentation. Among them, the method based on the variance of gray levels of the image has been reported to be a fast, simple yet accurate and robust indicator of presence and entity of blur [122]. Differently from the typical approaches for blur detection, which process the whole image, our technique has the advantage of having a rough a-priori knowledge of the position of the prosthetic component boundary. Thus we limited the variance measurement only in a narrow band area around the computed contour MS-C. As for the detection of the outer boundary OB-C, the deformation force field applied to the initial contour MS-C has been designed to preserve the shape details, especially sharp edges, obtained with the previous steps of the technique.

Unreliable contour point suppression is included as a final step of the proposed method considering the forthcoming 3D alignment procedure. Previous studies [104][112] on implant models detection from X-ray images showed that errors in segmentation lead to important errors in 3D/2D registration algorithms. Therefore, the possibility to automatically delete unreliable contour points could optimize pose estimation.

Our approach addresses typical issues limiting segmentation techniques in 3DF. Mahfouz *et al.* [111] used semi-automated segmentation methods based on snakes and on Canny edge detector. However the initial contour for the snake evolution had to be specified manually, and it was shown that the resulting contours vary significantly when noise was added. The segmentation method proposed by Domokos *et al.* [117] was affected by illumination varia-

tions typical of fluoroscopic images. Differently, our method was proven to be robust to noise and illumination gradients.

Our technique was applied to many implanted joints, including, but not limited to, hips and knee joints, since it does not require any a-priori information on model shapes and it could be of great interest for many clinical applications [131]. While the typical approach of manually selecting the prosthesis contours after applying edge detectors to the image (Canny filter) requires ∼1-2 min completely born by the user, the computational time of the new method is ∼25 s (of which only ∼10 s of user interaction) and it can be easily and greatly improved with code parallelization.

The limitations of the technique obviously include manual interaction. The seed point is used for image cropping and as starting point for the region growing algorithm. However, its position does not affect the outcome of the segmentation technique as shown by the results of the repeated analyses performed by different operators. As for the choice of the threshold in step C, the default value was found to be good enough in most cases. In addition, also un-experienced operators were able to easily set a threshold value leading to a good final segmentation in the remaining cases. An additional limitation is that this method is designed to compensate only for translational motion blur and not for other types of blur (such as out of focus blur and rotational motion blur). However, linear motion is the most common source of blur in 3DF; low entity focus or rotational blur can be roughly approximated to translational motion blur, and thus be still detected by our algorithm. Moreover, different deformation fields might be investigated in order to simulate other kinds of blurring.

This method was also applied to *in vivo* 3DF images. The preliminary tests, obtained using the same internal algorithm parameters specified for the *in silico* evaluations, were satisfactory and promising also on cemented parts. In addition, in the perspective of the analysis of an image sequence acquired during the execution of a specific exercise, given the very high temporal resolution achievable in 3DF, it could be feasible to reduce the manual interaction only to the first frame. This would allow an analysis of a whole 3DF sequence in few seconds. Moreover, the automation of the segmentation procedure would allow to better exploit high frequency fluoroscopic acquisition in favor of the 2D/3D alignment procedure.

In conclusion, a hybrid segmentation approach for 3D fluoroscopy has been presented and tested on both synthetic and real images. The obtained results show that the proposed technique succeeds in compensating for blurring and illumination gradient, in reducing user interaction and elaboration time, and in providing reliable prostheses contours, as required in the clinical environment.

Conclusion

This dissertation described the principal research projects pursued during my Ph.D. course in Bioengineering at the University of Bologna. Notably, the research activity has been performed at the Department of Electronics, Computer Sciences and Systems of the University of Bologna and, for a period of four months, at the Cardiac Imaging Research of the University of Chicago.

In Part I it has been reported the main research project, consisting in the the design, the implementation and the validation of an automated technique for myocardial identification as a basis for perfusion quantification in magnetic resonance images. Statistical level-set methods, known to be effective on other types of images, have been successfully implemented for myocardial segmentation in contrast-enhanced magnetic resonance images. Non-rigid inter-frame registration has been achieved by means of an innovative extension of the normalized cross-correlation algorithm in combination with level-set methods. The automated technique has been extensively tested on synthetic and real datasets. The wide range of comparisons between automated analysis and conventional manual tracing, which were performed also using quantitative coronary angiography and qualitative image interpretation as references, has demonstrated the robustness and reliability of the developed technique. As a consequence, this technique might substitute time-consuming manual tracing procedures, and thus address the strong clinical need for quantitative evaluation of myocardial perfusion. Of note, at the present time the proposed technique is being successfully used at the Cardiac Imaging Research of the University of Chicago for research purposes. Given the promising results, the developed methods could be applied to other segmentation/tracking problems in the field of biomedical image processing.

In Part II two side projects have been presented, relative to myocardial modelling using cine cardiac magnetic resonance images and necrotic scars detection using late Gadolinium enhancement images. In both cases, the segmentation methods implemented in the main project have been capable of providing a fast and reliable myocardial identification despite the different imaging protocol.

In Part III an unrelated research project has been described, consisting in the development and testing of a hybrid segmentation approach for prosthetic components in fluoroscopy. The proposed approach comprises different image processing methods such as anisotropic diffusion filtering, region growing and level-set techniques, and features a blur compensation mechanism. This approach has been tested on synthetic and real images, and the achieved results show that it might be adopted as a viable alternative to conventional Canny filtering and manual contour suppression procedures. Future work includes a larger validation scheme, in order to further assess the robustness and accuracy of the developed approach.

Publications and Awards

Peer-reviewed Papers

[P1] **G. Tarroni**, C. Corsi, P.F. Antkowiak, F. Veronesi, C.M. Kramer, F.H. Epstein, J. Walter, C. Lamberti, R.M. Lang, V. Mor-Avi, and A.R. Patel. Automated Quantification of Myocardial Perfusion at Rest and Stress from Contrast-Enhanced Magnetic Resonance Images. *Radiology*, in Review.

[P2] **G. Tarroni**, L. Tersi, C. Corsi, and R. Stagni. Prosthetic Component Segmentation with Blur Compensation: a Fast and Automated Method for 3D Fluoroscopy. *Medical and Biological Engineering and Computing*, in Press.

[P3] C.A. Conti, E. Votta, C. Corsi, D. De Marchi, **G. Tarroni**, M. Stevanella, M. Lombardi, O. Parodi, E.G. Caiani, and A. Redaelli. Left ventricular modelling: a quantitative functional assessment tool based on cardiac magnetic resonance imaging. *Interface Focus*, 1 (3):384-395, 2011.

Conference Proceedings

[P4] B.H. Freed, K.M. Turner, C. Yodwut, **G. Tarroni**, E. Estep, N.M. Bhave, A. Narang, S. Tanaka, C. Corsi, E. Gayat, P. Czobor, K. Cavanaugh, R.M. Lang, V. Mor-Avi, and A.R. Patel. Regadenoson cardiovascular magnetic resonance myocardial perfusion imaging predicts need for future revascularization. In *Journal of Cardiovascular Magnetic Resonance*, 14 (Suppl 1):P7, 2012.

[P5] A. Narang, C. Yodwut, **G. Tarroni**, E. Estep, K.M. Turner, B.H. Freed, N.M. Bhave, C. Corsi, M.H. Davidson, R.M. Lang, V. Mor-Avi, and A.R. Patel. Lipid sub-fractionation predicts worsening myocardial perfusion reserve in patients with low-density lipoprotein less than 100mg/dL: a regadenoson dardiac magnetic resonance study. In *Journal of Cardiovascular Magnetic Resonance*, 14 (Suppl 1):P70, 2012.

[P6] C. Corsi, **G. Tarroni**, A. Tornani, S. Severi, and C. Lamberti. Automatic Quantification of Cardiac Scar Extent from Late Gadolinium Enhancement MRI. In *Proceedings of Computing in Cardiology* 2011, in Press.

[P7] **G. Tarroni**, C. Corsi, P.F. Antkowiak, F. Veronesi, C.M. Kramer, F.H. Epstein, C. Lamberti, A.R. Patel, and V. Mor-Avi. Clinical Validation of an Automated Technique for MRI Based Quantification of Myocardial Perfusion. In *Proceedings of Computing in Cardiology* 2011, in Press.

[P8] **G. Tarroni**, A.R. Patel, P.F. Antkowiak, F.H. Epstein, C.M. Kramer, C. Lamberti, R.M. Lang, V. Mor-Avi, and C. Corsi. Automated frame-by-frame segmentation and non-rigid registration of MRI myocardial perfusion data at rest and stress. In *International Journal of CARS*, 6 (Suppl 1):S25, 2011.

[P9] **G. Tarroni**, C. Corsi, F. Veronesi, J. Walter, C. Lamberti, R.M. Lang, V. Mor-Avi, and A.R. Patel. Automated quantification of myocardial perfusion based on segmentation and non-rigid registration of contrast-enhanced cardiac magnetic resonance images. In *Journal of Cardiovascular Magnetic Resonance*, 13 (Suppl 1):P91, 2011.

[P10] E.G. Caiani, A. Redaelli, O. Parodi, E. Votta, F. Maffessanti, E. Tripoliti, G. Nucifora, **G. Tarroni**, M. Lombardi, and C. Corsi. Development and Validation of Automated Endocardial and Epicardial Contour Detection for MRI Volumetric and Wall Motion Analysis. In *Proceedings of Computing in Cardiology*, 37:1083-1086, 2010.

[P11] M. Lemmo, A. Azarine, **G. Tarroni**, and C. Corsi. Estimation of right ventricular volume, quantitative assessment of wall motion and trabeculae mass in arrhythmogenic right ventricular dysplasia. In *Proceedings of Computing in Cardiology*, 37:805-808, 2010.

[P12] **G. Tarroni**, A.R. Patel, F. Veronesi, J. Walter, C. Lamberti, R.M. Lang, V. Mor-Avi, and C. Corsi. MRI-based quantification of myocardial perfusion at rest and stress using automated frame-by-frame segmentation and non-rigid registration. In *Proceedings of Computing in Cardiology*, 37:1-4, 2010. (**Rosanna Degani Young Investigator Award**).

[P13] **G. Tarroni**, A.R. Patel, F. Veronesi, C. Lamberti, C. Corsi, and V. Mor-Avi. Automated Segmentation and Registration of Myocardium for Quantitative Assessment of First-Pass Perfusion MRI. In *Proceedings of Congresso GNB*, 2010.

[P14] **G. Tarroni**, A.R. Patel, F. Veronesi, C. Lamberti, V. Mor-Avi, and C. Corsi. Feasibility of automated frame-by-frame myocardial segmentation

as a basis for quantification of first-pass perfusion images. In *Journal of Cardiovascular Magnetic Resonance*, 12 (Suppl 1):O45, 2010.

Awards

[A1] Rosanna Degani Young Investigator Award for best oral and written presentation. *Computing in Cardiology*, Belfast, UK, 2010.

Bibliography

[1] WHO. Causes of Death 2008 Summary Tables. Technical report, 2011.

[2] WHO. World Health Statistics 2011. Technical report, 2011.

[3] WHO. The top 10 causes of death, 2011.

[4] Richard Niska, Farida Bhuiya, and Jianmin Xu. National Hospital Ambulatory Medical Care Survey: 2007 emergency department summary. *National health statistics reports*, (26):1–31, August 2010.

[5] Sanjiv Kaul. Myocardial contrast echocardiography: a 25-year retrospective. *Circulation*, 118(3):291–308, July 2008.

[6] M E Farkouh, P A Smars, G S Reeder, A R Zinsmeister, R W Evans, T D Meloy, S L Kopecky, M Allen, T G Allison, R J Gibbons, and S E Gabriel. A clinical trial of a chest-pain observation unit for patients with unstable angina. Chest Pain Evaluation in the Emergency Room (CHEER) Investigators. *The New England journal of medicine*, 339(26):1882–8, December 1998.

[7] J H Pope, T P Aufderheide, R Ruthazer, R H Woolard, J A Feldman, J R Beshansky, J L Griffith, and H P Selker. Missed diagnoses of acute cardiac ischemia in the emergency department. *The New England journal of medicine*, 342(16):1163–70, April 2000.

[8] Thomas Thom, Nancy Haase, Wayne Rosamond, Virginia J Howard, John Rumsfeld, Teri Manolio, Zhi-Jie Zheng, Katherine Flegal, Christopher O'Donnell, Steven Kittner, Donald Lloyd-Jones, David C Goff, Yuling Hong, Robert Adams, Gary Friday, Karen Furie, Philip Gorelick, Brett Kissela, John Marler, James Meigs, Veronique Roger, Stephen Sidney, Paul Sorlie, Julia Steinberger, Sylvia Wasserthiel-Smoller, Matthew Wilson, and Philip Wolf. Heart disease and stroke statistics-2006 update: a report from the American Heart Association Statistics Committee and Stroke Statistics Subcommittee. *Circulation*, 113(6):e85–151, February 2006.

[9] Robert C. Hendel, Daniel S. Berman, S. James Cullom, William Follansbee, Gary V. Heller, Hosen Kiat, Mark W. Groch, and John J. Mahmarian. Multicenter Clinical Trial to Evaluate the Efficacy of Correction for Photon Attenuation and Scatter in SPECT Myocardial Perfusion Imaging. *Circulation*, 99(21):2742–2749, 1999.

[10] Tust Techasith and Ricardo C Cury. Stress Myocardial CT Perfusion An Update and Future Perspective. *JACC. Cardiovascular imaging*, 4(8):905–16, August 2011.

[11] S.A. Hayat, G. Dwivedi, A. Jacobsen, T.K. Lim, C. Kinsey, and R. Senior. Effects of Left Bundle-Branch Block on Cardiac Structure, Function, Perfusion, and Perfusion Reserve: Implications for Myocardial Contrast Echocardiography Versus Radionuclide Perfusion Imaging for the Detection of Coronary Artery Disease. *Circulation*, 117(14):1832–1841, April 2008.

[12] A Storch-Becker, K P Kaiser, and L E Feinendegen. Cardiac nuclear medicine: positron emission tomography in clinical medicine. *European journal of nuclear medicine*, 13(12):648–52, January 1988.

[13] Piotr J Slomka, James A Patton, Daniel S Berman, and Guido Germano. Advances in technical aspects of myocardial perfusion SPECT imaging. *Journal of nuclear cardiology : official publication of the American Society of Nuclear Cardiology*, 16(2):255–76, January 2009.

[14] B Ohnesorge, T Flohr, C Becker, A F Kopp, U J Schoepf, U Baum, A Knez, K Klingenbeck-Regn, and M F Reiser. Cardiac imaging by means of electrocardiographically gated multisection spiral CT: initial experience. *Radiology*, 217(2):564–71, November 2000.

[15] Roxy Senior, Wolfgang Lepper, Agnes Pasquet, George Chung, Rainer Hoffman, Jean-Louis Vanoverschelde, Manuel Cerqueira, and Sanjiv Kaul. Myocardial perfusion assessment in patients with medium probability of coronary artery disease and no prior myocardial infarction: comparison of myocardial contrast echocardiography with 99mTc single-photon emission computed tomography. *American heart journal*, 147(6):1100–5, June 2004.

[16] Bobak Heydari, Michael Jerosch-Herold, and Raymond Y Kwong. Assessment of myocardial ischemia with cardiovascular magnetic resonance. *Progress in cardiovascular diseases*, 54(3):191–203, November 2011.

[17] Amit R Patel, Patrick F Antkowiak, Kiran R Nandalur, Amy M West, Michael Salerno, Vishal Arora, John Christopher, Frederick H Epstein,

and Christopher M Kramer. Assessment of advanced coronary artery disease: advantages of quantitative cardiac magnetic resonance perfusion analysis. *Journal of the American College of Cardiology*, 56(7):561–9, August 2010.

[18] Eike Nagel, Christoph Klein, Ingo Paetsch, Sabine Hettwer, Bernhard Schnackenburg, Karl Wegscheider, and Eckart Fleck. Magnetic resonance perfusion measurements for the noninvasive detection of coronary artery disease. *Circulation*, 108(4):432–7, July 2003.

[19] R.Y. Kwong, A.E. Schussheim, S. Rekhraj, A.H. Aletras, N. Geller, J. Davis, T.F. Christian, R.S. Balaban, and A.E. Arai. Detecting acute coronary syndrome in the emergency department with cardiac magnetic resonance imaging. *Circulation*, 107(4):531–537, January 2003.

[20] Kyle S McCommis, Thomas A Goldstein, Dana R Abendschein, Pilar Herrero, Robert J Gropler, and Jie Zheng. Quantification of Regional Myocardial Oxygenation by Magnetic Resonance Imaging: Validation With Positron Emission Tomography. *Circulation Cardiovascular Imaging*, 2010.

[21] Ganesh B. E. Adluru, Edward V. R. DiBella, and Matthias C. Schable. Model-Based Registration for Dynamic Cardiac Perfusion MRI. *Journal of Magnetic Resonance Imaging*, 1070(24):1062–1070, 2006.

[22] Gert Wollny, Maria J Ledesma-Carbayo, Peter Kellman, and Andres Santos. Exploiting Quasiperiodicity in Motion Correction of Free-Breathing Myocardial Perfusion MRI. *IEEE transactions on medical imaging*, 29(8):1516–1527, 2010.

[23] Chao Li, Ying Sun, and Ping Chai. Pseudo ground truth based non-rigid registration of myocardial perfusion MRI. *Medical image analysis*, 15(4):449–59, August 2011.

[24] Julien Milles, Rob J Van Der Geest, Michael Jerosch-Herold, Johan H C Reiber, and Boudewijn P F Lelieveldt. Fully Automated Motion Correction in First-Pass Myocardial Perfusion MR Image Sequences. *IEEE transactions on medical imaging*, 27(11):1611–1621, 2008.

[25] Vikas Gupta, Emile A Hendriks, Julien Milles, Rob J Van Der Geest, Michael Jerosch-Herold, Johan H C Reiber, and Boudewijn P F Lelieveldt. Fully Automatic Registration and Segmentation of First-Pass Myocardial Perfusion MR Image Sequences. *Academic Radiology*, 17(11):1375–1385, 2010.

[26] Christopher J Hardy, Harvey E Cline, Randy O Giaquinto, Thoralf Niendorf, Aaron K Grant, and Daniel K Sodickson. 32-element receiver-coil array for cardiac imaging. *Magnetic resonance in medicine : official journal of the Society of Magnetic Resonance in Medicine / Society of Magnetic Resonance in Medicine*, 55(5):1142–9, May 2006.

[27] R C Brasch. Introduction to the gadolinium class. *Journal of computer assisted tomography*, 17 Suppl 1:S14–8, January 1993.

[28] Massimo Lombardi and Carlo Bartolozzi. *MRI of the Heart and Vessels*. Springer, 2005.

[29] Nanaka Ishida, Hajime Sakuma, Munenobu Motoyasu, Tsutomu Okinaka, Naoki Isaka, Takeshi Nakano, and Kan Takeda. Noninfarcted myocardium: correlation between dynamic first-pass contrast-enhanced myocardial MR imaging and quantitative coronary angiography. *Radiology*, 229(1):209–16, October 2003.

[30] Mark Doyle, Anthon Fuisz, Eduardo Kortright, Robert W Biederman, Edward G Walsh, Edward T Martin, Lindsey Tauxe, William J Rogers, C Noel Merz, Carl Pepine, Barry Sharaf, and Gerald M Pohost. The impact of myocardial flow reserve on the detection of coronary artery disease by perfusion imaging methods: an NHLBI WISE study. *Journal of cardiovascular magnetic resonance : official journal of the Society for Cardiovascular Magnetic Resonance*, 5(3):475–85, July 2003.

[31] S D Wolff, J Schwitter, R Coulden, M G Friedrich, D A Bluemke, R W Biederman, E T Martin, A J Lansky, F Kashanian, T K F Foo, P E Licato, and C R Comeau. Myocardial first-pass perfusion magnetic resonance imaging: a multicenter dose-ranging study. *Circulation*, 110(6):732–7, August 2004.

[32] T H Giang, D Nanz, R Coulden, M Friedrich, M Graves, N Al-Saadi, T F Lüscher, G K von Schulthess, and J Schwitter. Detection of coronary artery disease by magnetic resonance myocardial perfusion imaging with various contrast medium doses: first European multi-centre experience. *European heart journal*, 25(18):1657–65, September 2004.

[33] Juerg Schwitter, Christian M Wacker, Albert C Van Rossum, Massimo Lombardi, Nidal Al-saadi, Hakan Ahlstrom, Thorsten Dill, Henrik B W Larsson, Scott D Flamm, Moritz Marquardt, and Lars Johansson. MR-IMPACT : comparison of perfusion-cardiac magnetic resonance with single-photon emission computed tomography for the detection of coronary artery disease in a multicentre, multivendor, randomized trial. *European Heart Journal*, pages 480–489, 2008.

[34] Kiran R Nandalur, Ben A Dwamena, Asim F Choudhri, Mohan R Nandalur, and Ruth C Carlos. Diagnostic performance of stress cardiac magnetic resonance imaging in the detection of coronary artery disease: a meta-analysis. *Journal of the American College of Cardiology*, 50(14):1343–53, October 2007.

[35] Michèle Hamon, Georges Fau, Guillaume Née, Javed Ehtisham, Rémy Morello, and Martial Hamon. Meta-analysis of the diagnostic performance of stress perfusion cardiovascular magnetic resonance for detection of coronary artery disease. *Journal of cardiovascular magnetic resonance : official journal of the Society for Cardiovascular Magnetic Resonance*, 12(1):29, January 2010.

[36] W Patricia Ingkanisorn, Raymond Y Kwong, Nicole S Bohme, Nancy L Geller, Kenneth L Rhoads, Christopher K Dyke, D Ian Paterson, Mushabbar A Syed, Anthony H Aletras, and Andrew E Arai. Prognosis of negative adenosine stress magnetic resonance in patients presenting to an emergency department with chest pain. *Journal of the American College of Cardiology*, 47(7):1427–32, April 2006.

[37] Chadwick D Miller, Wenke Hwang, James W Hoekstra, Doug Case, Cedric Lefebvre, Howard Blumstein, Brian Hiestand, Deborah B Diercks, Craig A Hamilton, Erin N Harper, and W Gregory Hundley. Stress cardiac magnetic resonance imaging with observation unit care reduces cost for patients with emergent chest pain: a randomized trial. *Annals of emergency medicine*, 56(3):209–219.e2, September 2010.

[38] J. Schwitter, D. Nanz, S. Kneifel, K. Bertschinger, M. Buchi, P. R. Knusel, B. Marincek, T. F. Luscher, and G. K. von Schulthess. Assessment of Myocardial Perfusion in Coronary Artery Disease by Magnetic Resonance : A Comparison With Positron Emission Tomography and Coronary Angiography. *Circulation*, 103(18):2230–2235, 2001.

[39] Bruce L Wilkoff, David Bello, Milos Taborsky, Josef Vymazal, Emanuel Kanal, Hubertus Heuer, Katrin Hecking, W Ben Johnson, William Young, Brian Ramza, Naveed Akhtar, Bernhard Kuepper, Peter Hunold, Roger Luechinger, Helmut Puererfellner, Firat Duru, M J W Gotte, Richard Sutton, and Torsten Sommer. Magnetic resonance imaging in patients with a pacemaker system designed for the magnetic resonance environment. *Heart rhythm : the official journal of the Heart Rhythm Society*, 8(1):65–73, January 2011.

[40] Thomas Grobner. Gadolinium-a specific trigger for the development of nephrogenic fibrosing dermopathy and nephrogenic systemic fibrosis?

Nephrology, dialysis, transplantation : official publication of the European Dialysis and Transplant Association - European Renal Association, 21(4):1104–8, April 2006.

[41] Martin R Prince, Honglei Zhang, Michael Morris, Jennifer L MacGregor, Marc E Grossman, Jeffrey Silberzweig, Robert L DeLapaz, Henry J Lee, Cynthia M Magro, and Anthony M Valeri. Incidence of nephrogenic systemic fibrosis at two large medical centers. *Radiology*, 248(3):807–16, September 2008.

[42] Daniel C Lee, Orlando P Simonetti, Kathleen R Harris, Thomas a Holly, Robert M Judd, Edwin Wu, and Francis J Klocke. Magnetic resonance versus radionuclide pharmacological stress perfusion imaging for flow-limiting stenoses of varying severity. *Circulation*, 110(1):58–65, July 2004.

[43] Michael Jerosch-Herold, Ravi Teja Seethamraju, Cory M Swingen, Norbert M Wilke, and Arthur E Stillman. Analysis of myocardial perfusion MRI. *Journal of magnetic resonance imaging : JMRI*, 19(6):758–70, June 2004.

[44] Philips. Elite Cardiac Clinical Solutions - Philips.

[45] Siemens. Argus Dynamic Signal.

[46] Andreas M. Weng, Christian O. Ritter, Joachim Lotz, Meinrad J. Beer, Dietbert Hahn, and Herbert Kostler. Automatic postprocessing for the assessment of quantitative human myocardial perfusion using MRI. *European Radiology*, (20):1356–1365, 2010.

[47] M F Santarelli, V Positano, C Michelassi, M Lombardi, and L Landini. Automated cardiac MR image segmentation: theory and measurement evaluation. *Medical engineering & physics*, 25(2):149–59, March 2003.

[48] Chao Li, Xiao Jia, and Ying Sun. Improved semi-automated segmentation of cardiac CT and MR images. In *2009 IEEE International Symposium on Biomedical Imaging: From Nano to Macro*, pages 25–28. IEEE, June 2009.

[49] L M Bidaut and J P Vallée. Automated registration of dynamic MR images for the quantification of myocardial perfusion. *Journal of magnetic resonance imaging : JMRI*, 13(4):648–55, April 2001.

[50] Christophe Dornier, Marko K Ivancevic, Philippe Thevenaz, and Jean-Paul Vallée. Improvement in the Quantification of Myocardial Perfusion Using an Automatic Spline-Based Registration Algorithm. *Journal of Magnetic Resonance Imaging*, 168:160 –168, 2003.

[51] Sandeep N Gupta, Meiyappan Solaiyappan, Garth M Beache, Andrew E Arai, and Thomas K F Foo. Fast Method for Correcting Image Misregistration Due to Organ Motion in Time-Series MRI Data. *Magnetic Resonance in Medicine*, 514:506 –514, 2003.

[52] H. Olafsdottir, M. B. Stegmann, B. K. Ersboll, and H. B. W. Larsson. A comparison of FFD-based nonrigid registration and AAMs applied to myocardial perfusion MRI. In Jaakko T Astola, Ioan Tabus, and Junior Barrera, editors, *Proceedings of SPIE*, volume 6144 of *Society of Photo-Optical Instrumentation Engineers (SPIE) Conference Series*, pages 614416–I. SPIE, 2006.

[53] M. B. Stegmann, H. Olafsdottir, and H. B. W. Larsson. Unsupervised motion-compensation of multi-slice cardiac perfusion MRI. *Medical Image Analysis*, 9:394–410, 2005.

[54] Dwarikanath Mahapatra and Ying Sun. Integrating segmentation information for improved MRF-based elastic image registration. *IEEE transactions on image processing : a publication of the IEEE Signal Processing Society*, 21(1):170–83, January 2012.

[55] Stanley Osher and James A Sethian. Fronts propagating with curvature-dependent speed: Algorithms based on Hamilton-Jacobi formulations. *Journal of Computational Physics*, 79(1):12–49, November 1988.

[56] R. Malladi, J.A. Sethian, and B.C. Vemuri. Shape modeling with front propagation: a level set approach. *IEEE Transactions on Pattern Analysis and Machine Intelligence*, 17(2):158–175, 1995.

[57] J. A. Sethian. *Level Set Methods and Fast Marching Methods: Evolving Interfaces in Computational Geometry, Fluid Mechanics, Computer Vision, and Materials Science ... on Applied and Computational Mathematics)*. Cambridge University Press, 1999.

[58] Xavier Bresson. *Image Segmentation with Variational Active Contours*. PhD thesis, EPFL, 2005.

[59] Matthew A. Grayson. The heat equation shrinks embedded plane curves to round points. *Journal of Differential Geometry*, 26(2):285–314, 1987.

[60] Vicent Caselles, Ron Kimmel, and Guillermo Sapiro. Geodesic active contours. *International journal of computer vision*, 22(1):61–79, 1997.

[61] Pietro Perona and Jitendra Malik. Scale-Space and Edge Detection Using Anisotropic Diffusion. *IEEE Transactions on Pattern Analysis and Machine Intelligence*, 12(7), 1990.

[62] Laurent D Cohen. On active contour models and balloons. *Computer Vision Graphics and Image Processing Image Understanding*, 53(2):211–218, 1991.

[63] S.C. Zhu, T.S. Lee, and A.L. Yuille. Region competition: unifying snakes, region growing, energy/Bayes/MDL for multi-band image segmentation. In *Proceedings of IEEE International Conference on Computer Vision*, pages 416–423. IEEE Comput. Soc. Press.

[64] T F Chan and L A Vese. Active contours without edges. *IEEE transactions on image processing : a publication of the IEEE Signal Processing Society*, 10(2):266–77, January 2001.

[65] Alessandro Sarti, Cristiana Corsi, Elena Mazzini, and Claudio Lamberti. Maximum likelihood segmentation of ultrasound images with Rayleigh distribution. *IEEE transactions on ultrasonics, ferroelectrics, and frequency control*, 52(6):947–60, June 2005.

[66] Cristiana Corsi, Federico Veronesi, Claudio Lamberti, Dianna M E Bardo, Ernest B Jamison, Roberto M Lang, and Victor Mor-Avi. Automated frame-by-frame endocardial border detection from cardiac magnetic resonance images for quantitative assessment of left ventricular function: validation and clinical feasibility. *Journal of magnetic resonance imaging : JMRI*, 29(3):560–8, March 2009.

[67] P Kellman, F H Epstein, and E R McVeigh. Adaptive sensitivity encoding incorporating temporal filtering (TSENSE). *Magnetic resonance in medicine : official journal of the Society of Magnetic Resonance in Medicine / Society of Magnetic Resonance in Medicine*, 45(5):846–52, May 2001.

[68] D.P. Huttenlocher, G.A. Klanderman, and W.J. Rucklidge. Comparing images using the Hausdorff distance. *IEEE Transactions on Pattern Analysis and Machine Intelligence*, 15(9):850–863, 1993.

[69] Pratim Ghosh, Mehmet Emre Sargin, and B S Manjunath. Robust dynamical model for simultaneous registration and segmentation in a variational framework: A Bayesian approach. In *2009 IEEE 12th International Conference on Computer Vision*, pages 709–716. IEEE, September 2009.

[70] Marie-Pierre Jolly, Hui Xue, Leo Grady, and Jens Guehring. Combining registration and minimum surfaces for the segmentation of the left ventricle in cardiac cine MR images. *Medical image computing and computer-assisted intervention : MICCAI ... International Conference on Medical Image Computing and Computer-Assisted Intervention*, 12(Pt 2):910–8, January 2009.

[71] Lee R. Dice. Measures of the Amount of Ecologic Association Between Species. *Ecology*, 26(3):297, July 1945.

[72] Manuel D Cerqueira, Neil J Weissman, Vasken Dilsizian, Alice K Jacobs, Sanjiv Kaul, Warren K Laskey, Dudley J Pennell, John A Rumberger, Thomas Ryan, and Mario S Verani. Standardized myocardial segmentation and nomenclature for tomographic imaging of the heart: a statement for healthcare professionals from the Cardiac Imaging Committee of the Council on Clinical Cardiology of the American Heart Association. *Circulation*, 105(4):539–42, January 2002.

[73] Frans P P J Kremers, Mark B M Hofman, Jan G J Groothuis, Michael Jerosch-Herold, Aernout M Beek, Sven Zuehlsdorff, Sonia Nielles-Vallespin, Albert C van Rossum, and Robert M Heethaar. Improved correction of spatial inhomogeneities of surface coils in quantitative analysis of first-pass myocardial perfusion imaging. *Journal of magnetic resonance imaging : JMRI*, 31(1):227–33, January 2010.

[74] N G Uren, J A Melin, B De Bruyne, W Wijns, T Baudhuin, and P G Camici. Relation between myocardial blood flow and the severity of coronary-artery stenosis. *The New England journal of medicine*, 330(25):1782–8, June 1994.

[75] TM Bateman, GV Heller, and AI McGhie. Diagnostic accuracy of rest/stress ECG-gated Rb-82 myocardial perfusion PET: comparison with ECG-gated Tc-99m sestamibi SPECT. *Journal of nuclear cardiology : official publication of the American Society of Nuclear Cardiology*, 13(1):24–33, 2006.

[76] Marshall I Hertz, Paul Aurora, Jason D Christie, Fabienne Dobbels, Leah B Edwards, Richard Kirk, Anna Y Kucheryavaya, Axel O Rahmel, Amanda W Rowe, and David O Taylor. Registry of the International Society for Heart and Lung Transplantation: a quarter century of thoracic transplantation. *The Journal of heart and lung transplantation : the official publication of the International Society for Heart Transplantation*, 27(9):937–42, September 2008.

[77] M G Sutton and N Sharpe. Left ventricular remodeling after myocardial infarction: pathophysiology and therapy. *Circulation*, 101(25):2981–8, June 2000.

[78] W G Hundley, B M Meshack, D L Willett, D E Sayad, R A Lange, J E Willard, C Landau, L D Hillis, and R M Peshock. Comparison of quantitation of left ventricular volume, ejection fraction, and cardiac output in patients with atrial fibrillation by cine magnetic resonance imag-

ing versus invasive measurements. *The American journal of cardiology*, 78(10):1119–23, November 1996.

[79] E Nagel, U Schneider, S Schalla, T Ibrahim, B Schnackenburg, A Bornstedt, C Klein, H B Lehmkuhl, and E Fleck. Magnetic resonance real-time imaging for the evaluation of left ventricular function. *Journal of cardiovascular magnetic resonance : official journal of the Society for Cardiovascular Magnetic Resonance*, 2(1):7–14, January 2000.

[80] A F Frangi, W J Niessen, and M A Viergever. Three-dimensional modeling for functional analysis of cardiac images: a review. *IEEE transactions on medical imaging*, 20(1):2–25, January 2001.

[81] Mehmet Uzümcü, Rob J van der Geest, Cory Swingen, Johan H C Reiber, and Boudewijn P F Lelieveldt. Time continuous tracking and segmentation of cardiovascular magnetic resonance images using multidimensional dynamic programming. *Investigative radiology*, 41(1):52–62, January 2006.

[82] E Angelie, P J H de Koning, M G Danilouchkine, H C van Assen, G Koning, R J van der Geest, and J H C Reiber. Optimizing the automatic segmentation of the left ventricle in magnetic resonance images. *Medical physics*, 32(2):369–75, February 2005.

[83] N F Osman, W S Kerwin, E R McVeigh, and J L Prince. Cardiac motion tracking using CINE harmonic phase (HARP) magnetic resonance imaging. *Magnetic resonance in medicine : official journal of the Society of Magnetic Resonance in Medicine / Society of Magnetic Resonance in Medicine*, 42(6):1048–60, December 1999.

[84] W G O'Dell, C C Moore, W C Hunter, E A Zerhouni, and E R McVeigh. Three-dimensional myocardial deformations: calculation with displacement field fitting to tagged MR images. *Radiology*, 195(3):829–35, June 1995.

[85] Li Pan, Jerry L Prince, João A C Lima, and Nael F Osman. Fast tracking of cardiac motion using 3D-HARP. *IEEE transactions on bio-medical engineering*, 52(8):1425–35, August 2005.

[86] A A Young. Model tags: direct three-dimensional tracking of heart wall motion from tagged magnetic resonance images. *Medical image analysis*, 3(4):361–72, December 1999.

[87] Salome Ryf, Marcus A Spiegel, Michael Gerber, and Peter Boesiger. Myocardial tagging with 3D-CSPAMM. *Journal of magnetic resonance imaging : JMRI*, 16(3):320–5, September 2002.

[88] A.C. Bovik. On detecting edges in speckle imagery. *IEEE Transactions on Acoustics, Speech, and Signal Processing*, 36(10):1618–1627, 1988.

[89] Adelchi Azzalini. *Statistical Inference Based on the likelihood*. Chapman and Hall/CRC, 1996.

[90] C. Chesnaud, P. Refregier, and V. Boulet. Statistical region snake-based segmentation adapted to different physical noise models. *IEEE Transactions on Pattern Analysis and Machine Intelligence*, 21(11):1145–1157, 1999.

[91] X. Lin, N. J. B. McFarlane, Y. Zhao, G. J. Clapworthy, F. Dong, and A. Redaelli. Visualisation of Left Ventricular Dysfunction in the Virtual Pathological Heart. In *2010 14th International Conference Information Visualisation*, pages 635–640. IEEE, July 2010.

[92] Miguel Vieira and Kenji Shimada. Surface mesh segmentation and smooth surface extraction through region growing. *Computer Aided Geometric Design*, 22(8):771–792, November 2005.

[93] Niall G Keenan and Dudley J Pennell. CMR of ventricular function. *Echocardiography (Mount Kisco, N.Y.)*, 24(2):185–93, February 2007.

[94] Liang Zhong, Yi Su, Si-Yong Yeo, Ru-San Tan, Dhanjoo N Ghista, and Ghassan Kassab. Left ventricular regional wall curvedness and wall stress in patients with ischemic dilated cardiomyopathy. *American Journal of Physiology Heart and Circulatory Physiology*, 296(3):H573–H584, 2009.

[95] Thor Edvardsen, Bernhard L Gerber, Jérôme Garot, David A Bluemke, João A C Lima, and Otto A Smiseth. Quantitative assessment of intrinsic regional myocardial deformation by Doppler strain rate echocardiography in humans: validation against three-dimensional tagged magnetic resonance imaging. *Circulation*, 106(1):50–6, July 2002.

[96] Yuichi Notomi, Randolph M Setser, Takahiro Shiota, Maureen G Martin-Miklovic, Joan A Weaver, Zoran B Popović, Hirotsugu Yamada, Neil L Greenberg, Richard D White, and James D Thomas. Assessment of left ventricular torsional deformation by Doppler tissue imaging: validation study with tagged magnetic resonance imaging. *Circulation*, 111(9):1141–7, March 2005.

[97] Iris K Rüssel, Marco J W Götte, Jean G Bronzwaer, Paul Knaapen, Walter J Paulus, and Albert C van Rossum. Left ventricular torsion: an expanding role in the analysis of myocardial dysfunction. *JACC. Cardiovascular imaging*, 2(5):648–55, May 2009.

[98] Mathieu De Craene, Gemma Piella, Oscar Camara, Nicolas Duchateau, Etelvino Silva, Adelina Doltra, Jan D'hooge, Josep Brugada, Marta Sitges, and Alejandro F Frangi. Temporal diffeomorphic free-form deformation: application to motion and strain estimation from 3D echocardiography. *Medical image analysis*, 16(2):427–50, February 2012.

[99] W Gregory Hundley, David A Bluemke, J Paul Finn, Scott D Flamm, Mark A Fogel, Matthias G Friedrich, Vincent B Ho, Michael Jerosch-Herold, Christopher M Kramer, Warren J Manning, Manesh Patel, Gerald M Pohost, Arthur E Stillman, Richard D White, and Pamela K Woodard. ACCF/ACR/AHA/NASCI/SCMR 2010 expert consensus document on cardiovascular magnetic resonance: a report of the American College of Cardiology Foundation Task Force on Expert Consensus Documents. *Journal of the American College of Cardiology*, 55(23):2614–62, June 2010.

[100] R J Kim, E Wu, A Rafael, E L Chen, M A Parker, O Simonetti, F J Klocke, R O Bonow, and R M Judd. The use of contrast-enhanced magnetic resonance imaging to identify reversible myocardial dysfunction. *The New England journal of medicine*, 343(20):1445–53, November 2000.

[101] Raymond Y Kwong, Anna K Chan, Kenneth A Brown, Carmen W Chan, H Glenn Reynolds, Sui Tsang, and Roger B Davis. Impact of unrecognized myocardial scar detected by cardiac magnetic resonance imaging on event-free survival in patients presenting with signs or symptoms of coronary artery disease. *Circulation*, 113(23):2733–43, 2006.

[102] Randolph M Setser, Daniel G Bexell, Thomas P O'Donnell, Arthur E Stillman, Michael L Lieber, Paul Schoenhagen, and Richard D White. Quantitative assessment of myocardial scar in delayed enhancement magnetic resonance imaging. *Journal of magnetic resonance imaging : JMRI*, 18(4):434–41, October 2003.

[103] R Malladi and J a Sethian. Image processing via level set curvature flow. *Proceedings of the National Academy of Sciences of the United States of America*, 92(15):7046–50, July 1995.

[104] S A Banks and W A Hodge. Accurate measurement of three-dimensional knee replacement kinematics using single-plane fluoroscopy. *IEEE transactions on bio-medical engineering*, 43(6):638–49, June 1996.

[105] P Bifulco, M Cesarelli, R Allen, M Sansone, and M Bracale. Automatic recognition of vertebral landmarks in fluoroscopic sequences for analysis of intervertebral kinematics. *Medical & biological engineering & computing*, 39(1):65–75, January 2001.

[106] Shunji Hirokawa, M Abrar Hossain, Yuichi Kihara, and Shogo Ariyoshi. A 3D kinematic estimation of knee prosthesis using X-ray projection images: clinical assessment of the improved algorithm for fluoroscopy images. *Medical & biological engineering & computing*, 46(12):1253–62, December 2008.

[107] Bart L Kaptein, Edward R Valstar, Berend C Stoel, Hans C Reiber, and Rob G Nelissen. Clinical validation of model-based RSA for a total knee prosthesis. *Clinical orthopaedics and related research*, 464:205–9, November 2007.

[108] D A Dennis, R D Komistek, W A Hoff, and S M Gabriel. In vivo knee kinematics derived using an inverse perspective technique. *Clinical orthopaedics and related research*, (331):107–17, October 1996.

[109] S Zuffi, a Leardini, F Catani, S Fantozzi, and a Cappello. A model-based method for the reconstruction of total knee replacement kinematics. *IEEE transactions on medical imaging*, 18(10):981–91, October 1999.

[110] Christof Hurschler, Frank Seehaus, Judith Emmerich, Bart L Kaptein, and Henning Windhagen. Accuracy of model-based RSA contour reduction in a typical clinical application. *Clinical orthopaedics and related research*, 466(8):1978–86, August 2008.

[111] Mohamed R Mahfouz, William a Hoff, Richard D Komistek, and Douglas a Dennis. Effect of segmentation errors on 3D-to-2D registration of implant models in X-ray images. *Journal of biomechanics*, 38(2):229–39, March 2005.

[112] William A. Hoff, Richard D. Komistek, Douglas A. Dennis, Stefan M. Gabriel, and Scott A. Walker. Three-dimensional determination of femoral-tibial contact positions under in vivo conditions using fluoroscopy. *Clinical biomechanics (Bristol, Avon)*, 13(7):455–472, October 1998.

[113] John Canny. A Computational Approach to Edge Detection. *IEEE Transactions on Pattern Analysis and Machine Intelligence*, PAMI-8(6):679–698, November 1986.

[114] B L Kaptein, E R Valstar, B C Stoel, P M Rozing, and J H C Reiber. A new model-based RSA method validated using CAD models and models from reversed engineering. *Journal of biomechanics*, 36(6):873–82, June 2003.

[115] Takaharu Yamazaki, Tetsu Watanabe, Yoshikazu Nakajima, Kazuomi Sugamoto, Tetsuya Tomita, Hideki Yoshikawa, and Shinichi Tamura.

Improvement of depth position in 2-D/3-D registration of knee implants using single-plane fluoroscopy. *IEEE transactions on medical imaging*, 23(5):602–12, May 2004.

[116] C L Chan, A K Katsaggelos, and A V Sahakian. Image sequence filtering in quantum-limited noise with applications to low-dose fluoroscopy. *IEEE transactions on medical imaging*, 12(3):610–21, January 1993.

[117] Csaba Domokos and Zoltan Kato. Parametric estimation of affine deformations of planar shapes. *Pattern Recognition*, 43(3):569–578, 2010.

[118] Kush R Varshney, Nikos Paragios, Jean-François Deux, Alain Kulski, Rémy Raymond, Phillipe Hernigou, and Alain Rahmouni. Postarthroplasty examination using X-ray images. *IEEE transactions on medical imaging*, 28(3):469–74, March 2009.

[119] Scott Tashman and William Anderst. In-vivo measurement of dynamic joint motion using high speed biplane radiography and CT: application to canine ACL deficiency. *Journal of biomechanical engineering*, 125(2):238–45, April 2003.

[120] G. Sapiro. Geometric partial differential equations in image analysis: past, present, and future. In *Proceedings., International Conference on Image Processing*, volume 3, pages 1–4. IEEE Comput. Soc. Press.

[121] William K. Pratt. *Digital Image Processing.* John Wiley & Sons, Inc., 2007.

[122] C. F. Batten, D. M. Holburn, B. C. Breton, and N. H. M. Caldwell. Sharpness Search Algorithms for Automatic Focusing in the Scanning Electron Microscope. *Journal of scanning microscopy*, 2001.

[123] Dong Zhao, Scott A Banks, Darryl D D'Lima, Clifford W Colwell, and Benjamin J Fregly. In vivo medial and lateral tibial loads during dynamic and high flexion activities. *Journal of orthopaedic research : official publication of the Orthopaedic Research Society*, 25(5):593–602, May 2007.

[124] B M You, P Siy, W Anderst, and S Tashman. In vivo measurement of 3-D skeletal kinematics from sequences of biplane radiographs: application to knee kinematics. *IEEE transactions on medical imaging*, 20(6):514–25, June 2001.

[125] Tyrrell R. Rockafellar and Roger J.-B. Wets. *Variational Analysis.* Springer, 2004.

[126] Mohamed R Mahfouz, William a Hoff, Richard D Komistek, and Douglas a Dennis. A robust method for registration of three-dimensional knee

implant models to two-dimensional fluoroscopy images. *IEEE transactions on medical imaging*, 22(12):1561–74, December 2003.

[127] Alina Oprea and Constantin Vertan. A Quantitative Evaluation of the Hip Prosthesis Segmentation Quality in X-Ray Images. In *2007 International Symposium on Signals, Circuits and Systems*, pages 1–4. IEEE, July 2007.

[128] J.H. Elder and S.W. Zucker. Local scale control for edge detection and blur estimation. *IEEE Transactions on Pattern Analysis and Machine Intelligence*, 20(7):699–716, July 1998.

[129] N Narvekar and L Karam. A No-Reference Image Blur Metric Based on the Cumulative Probability of Blur Detection (CPBD). *IEEE transactions on image processing : a publication of the IEEE Signal Processing Society*, (480):1–7, March 2011.

[130] E. Tsomko, H.J. Kim, and E. Izquierdo. Linear Gaussian blur evolution for detection of blurry images. *IET Image Processing*, 4(4):302, 2010.

[131] Matías De La Fuente, Jörg A K Ohnsorge, Erik Schkommodau, Stefanie Jetzki, Dieter C Wirtz, and Klaus Radermacher. Fluoroscopy-based 3-D reconstruction of femoral bone cement: a new approach for revision total hip replacement. *IEEE transactions on bio-medical engineering*, 52(4):664–75, April 2005.

Giacomo Tarroni was born in Castel San Pietro Terme (BO), Italy, in 1983. He obtained a B.Sc. degree in Electronic Engineering in 2005 and a M.Sc. degree in Electronic Engineering for Biomedical Applications in 2008, both at the University of Bologna. In 2009 he was admitted to the Ph.D course in Bioengineering at the Department of Electronics, Computer Sciences and Systems at the University of Bologna. His main research interests are related to the field of biomedical image processing and include variational techniques for image segmentation, multi-scale registration, image deblurring, object tracking as well as novel acquisition protocols for magnetic resonance imaging.